



Intelligent Wireless Networks and Robots for Low-Cost Battery-Less Sensing and Localization

BY
EVANGELOS GIANNELOS

A DISSERTATION
SUBMITTED IN PARTIAL FULFILLMENT OF THE
REQUIREMENTS FOR THE DEGREE OF

DOCTOR OF PHILOSOPHY
IN
TECHNICAL UNIVERSITY OF CRETE
SCHOOL OF ELECTRICAL AND COMPUTER ENGINEERING

COMMITTEE IN CHARGE:
PROFESSOR AGGELOS BLETSAS (SUPERVISOR)
PROFESSOR GEORGE N. KARYSTINOS
PROFESSOR MICHAEL G. LAGOUDAKIS

OCTOBER 2023

© Copyright by Evangelos Giannelos, 2023.
All rights reserved.

Έξυπνα Ασύρματα Δίκτυα και Ρομπότ για
Χαμηλού Κόστους Αισθητήρες και Προσδιορισμό
Θέσης

Abstract

This dissertation presents a comprehensive exploration of radio frequency identification (RFID) technology merged with robotics, shedding light on their transformative potential and inherent challenges. At the heart of our research lies the meticulous study of monostatic localization using novel techniques that do not necessarily imitate a synthetic aperture radar (SAR), in sharp contrast to prior art; instead, the adopted approach exploits sparse and low-bandwidth phase measurements with appropriate particle filtering weights, so that robustness to indoor multipath is achieved. As a result, state-of-the-art performance in 3D localization utilizing commercial Gen2 RFID tags is achieved with a mean absolute error of 24 cm.

Building upon this foundational work, the research delves into the intricacies of multipath effects, particularly the distortions introduced by environmental reflections. Notably, the investigation in this realm resulted in a technique that jointly estimates the location of the tag as well as its reflector with a reflector localization accuracy of 5 cm; such (perhaps) pioneering endeavor adheres to low bandwidth limitations of existing, commercial RFID systems.

Furthermore, study of bistatic/multistatic localization is performed, offering elliptical direction-of-arrival (DoA) estimation and 2D/3D localization techniques, with unique geometrical considerations and their implications on RFID systems. These techniques offer estimations with as low as 5° and 9 cm mean absolute error for DoA and 2D localization respectively.

Transitioning next into the realm of wireless sensor networks (WSNs), the dissertation elucidates the symbiotic relationship between RFIDs and WSNs, emphasizing key considerations surrounding interrogation architectures and their real-world ramifications. Experiments include both unmanned aerial vehicles (UAV), as well as ground-based pedestrian interrogation systems, using bistatic and monostatic architectures.

A paramount feature of this research is the seamless integration of theoretical studies with tangible applications, resulting in real-world systems primed for diverse applications. This is exemplified in our development of a mobile interrogation and localization system, integrated with the Robot Operating System (ROS), capable of pinpointing RFID tags in complex environments, like warehouses, libraries, and offices. Further, the synergy of UAV-based interrogation with backscatter technology emerges as a beacon of innovation, signaling new horizons in precision agriculture.

Περίληψη

Η παρούσα διατριβή παρουσιάζει μια ολοκληρωμένη διερεύνηση της τεχνολογίας αναγνώρισης μέσω ραδιοσυχνοτήτων (RFID) σε συνδυασμό με τη ρομποτική, προβάλλοντας τις μετασχηματιστικές της δυνατότητες και τις εγγενείς της προκλήσεις. Στο επίκεντρο της έρευνάς μας βρίσκεται η αναλυτική μελέτη του μονοστατικού εντοπισμού με τη χρήση νέων τεχνικών που δεν αποτελούν αναγκαστικά μίμηση ενός ραντάρ συνθετικού διαφράγματος (SAR), σε έντονη αντίθεση με τις προϋπάρχουσες τεχνικές- αντ' αυτού, η προσέγγιση που υιοθετήθηκε αξιοποιεί αραιές και χαμηλού εύρους ζώνης μετρήσεις φάσης με φίλτρα σωματιδίων κατάλληλα ζυγισμένα, έτσι ώστε να επιτυγχάνεται ανθεκτικότητα στην ανακλαστικότητα εσωτερικών χώρων. Ως αποτέλεσμα, επιτυγχάνεται κορυφαία επίδοση στον τριδιάστατο εντοπισμό θέσης χρησιμοποιώντας εμπορικές ετικέτες RFID Gen2 με μέσο απόλυτο σφάλμα 24 εκ.

Βασιζόμενη σε αυτή τη θεμελιώδη εργασία, η έρευνα εμβαθύνει στις ιδιαιτερότητες του φαινομένου πολλαπλών διαδρομών διάδοσης λόγω ανακλάσεων, και συγκεκριμένα στις παραμορφώσεις που προκαλούνται από αυτές τις ανακλάσεις. Αξίζει να σημειωθεί ότι η διερεύνηση σε αυτό το πεδίο οδήγησε σε μια τεχνική που εκτιμά από κοινού τη θέση της ετικέτας, καθώς και του ανακλαστήρα της, με 5 εκ. ακρίβεια στον εντοπισμού του ανακλαστήρα- αυτή η (ίσως) πρωτοποριακή προσπάθεια ακολουθεί τους περιορισμούς χαμηλού εύρους ζώνης των υφιστάμενων, εμπορικών συστημάτων RFID.

Επιπλέον, πραγματοποιήθηκε μελέτη του διστατικού/πολυστατικού εντοπισμού θέσης, προσφέροντας μια «ελλειπτική» εκτίμηση της κατεύθυνσης άφιξης (DoA), τεχνικές 2D/3D εντοπισμού βασιζόμενες σε ιδιαίτερες γεωμετρικές ιδιότητες και τις ιδιαιτερότητες της εφαρμογής τους σε συστήματα RFID. Οι τεχνικές αυτές προσφέρουν εκτιμήσεις με μέσο απόλυτο σφάλμα μόλις 5° και 9 εκ. για DoA και 2D εντοπισμό, αντίστοιχα.

Μεταβαίνοντας στη συνέχεια στον τομέα των ασύρματων δικτύων αισθητήρων (WSN), η διατριβή μελετά τη συμβιωτική σχέση μεταξύ των RFID και των WSN, δίνοντας έμφαση σε βασικά ζητήματα σχετικά με τις αρχιτεκτονικές ανάγνωσης και τις επιπτώσεις τους σε πραγματικές εφαρμογές. Τα πειράματα περιλαμβάνουν τόσο μη επανδρωμένα εναέρια οχήματα (UAV), όσο και επίγεια συστήματα ανάγνωσης με πεζούς, χρησιμοποιώντας διστατικές και μονοστατικές αρχιτεκτονικές.

Πρωταρχικό χαρακτηριστικό αυτής της έρευνας είναι η άρτια ενσωμάτωση των θεωρητικών μελετών σε απτές εφαρμογές, καταλήγοντας σε πραγματικά συστήματα έτοιμα για διάφορες εφαρμογές. Αυτό αποδεικνύεται από την ανάπτυξη ενός κινητού συστήματος ανάγνωσης και εντοπισμού ετικετών, ενοποιημένο με το ρομποτικό λειτουργικό σύστημα (ROS), το οποίο είναι ικανό να εντοπίζει ετικέτες RFID σε πολύπλοκα περιβάλλοντα όπως αποθήκες, βιβλιοθήκες και γραφεία. Περαιτέρω, η συνέργεια της ανάγνωσης μέσω UAV σε

συνδυασμό με την τεχνολογία οπισθοσκέδασης αναδεικνύεται ως παράδειγμα καινοτομίας, σηματοδοτώντας νέους ορίζοντες στη γεωργία ακριβείας.

Acknowledgements

To the invaluable individuals who have contributed to my journey, both academically and personally, I offer my sincere gratitude.

First and foremost, I owe an immense debt of gratitude to my supervisor. Throughout my undergraduate degree and all the way to the completion of this PhD, your unwavering faith in my abilities, your critical insights, and your ceaseless dedication have been the compass guiding me through this journey. Your mentorship has transcended the boundaries of academia, giving me the boost I needed even when going through tough times personally.

To Professor G. Karystinos, not only for your participation to my committee but for the honor you've given me by naming a theorem after me and incorporating it to your lectures. I am deeply humbled by this gesture and will forever carry it with pride.

I cannot forget the pivotal role played by my close lab coworkers and friends. Our late nights, the brainstorming sessions, the expeditions, the successes, and even the setbacks – each of these moments were made bearable and memorable because of your camaraderie. These moments will always remind me of all the fun and good times we had together.

To the broader community of our lab's members over the years, your feedback, shared expertise, and the spirit of collective endeavor have enriched my doctoral experience immeasurably.

Outside of the academic sphere, my gratitude extends to my dearest friends. You've been a consistent beacon of support and a reminder of the world outside the lab. From the countless nights in the university's dorms to our adventurous trips, through highs and lows, you've been the source of some of my most treasured moments away from home. Most notably, your faith in me, even in times when I had little in myself, has been unwavering.

To my family, thank you for laying the foundation upon which this achievement rests. Your sacrifices, teachings, and endless love have been my strongest pillars. Even though I was away from you, I always felt you were there for me in both times of joy and need. Your support and belief in me has been the wind beneath my wings.

Lastly, but most intimately, to my partner in life, Aneza. You have been my rock throughout this journey, my confidante in times of doubt, and the person to share my happiness in times of triumph. Your patience, understanding, excitement, and love have made this journey not just bearable, but truly fulfilling. You were always there for me and shared the weight of my challenges until the end. This achievement, while mine in name, would be incomplete without you.

In sum, this journey through academia and life, riddled with challenges and triumphs, has been a collective endeavor. To all who have been a part of it, my heartfelt thanks.



RELIEF

Intelligent Repeaters & Robots
for RFID Inventorying & Localization

This research has been cofinanced by the European Union and Greek national funds through the Operational Program Competitiveness, Entrepreneurship and Innovation, under the call RESEARCH - CREATE - INNOVATE (project code: T1EDK-03032).



European Union
European Regional
Development Fund



ΕΡΑνηΕΚ 2014-2020
OPERATIONAL PROGRAMME
COMPETITIVENESS
ENTREPRENEURSHIP
INNOVATION



Co-financed by Greece and the European Union

«The implementation of the doctoral thesis was co-financed by Greece and the European Union (European Social Fund-ESF) through the Operational Programme «Human Resources Development, Education and Lifelong Learning» in the context of the Act “Enhancing Human Resources Research Potential by undertaking a Doctoral Research” Sub-action 2: IKY Scholarship Programme for PhD candidates in the Greek Universities».



European Union
European Social Fund

Operational Programme
Human Resources Development,
Education and Lifelong Learning

Co-financed by Greece and the European Union



Contents

Abstract	iv
Acknowledgements	vii
1 Introduction	1
1.1 Applications of RFIDs	3
1.2 Motivation	4
1.3 Technical Preliminaries - ROS, Robotic Platform and Drone	5
1.3.1 ROS	5
1.3.2 Robot Setup Description - The Turtlebot2 Platform	7
1.3.3 Robot Setup Description - Added Components	9
1.3.4 Drone Setup Description - The Drone Platform	18
1.3.5 Drone Setup Description - Added Components	19
1.4 Roadmap	22
1.5 Thesis Contributions	22
2 Monostatic Localization with a Robotic Platform	24
2.1 RFID Systems: Monostatic Architecture, and Phase-Based Distance Estimation	25
2.1.1 Phase model	26
2.2 Particle Filtering for Phase-Based RFID Localization	30
2.2.1 Introduction to Particle Filtering	30
2.2.2 Phase Based Particle Filtering	31
2.2.3 Robust Distance-based Particle Filtering (RDPF)	32
2.2.4 Experimental Results and Analysis	41
2.3 Conclusion	49
3 Reflection and Tag Joint Localization	51
3.1 Introduction	51
3.2 Reflection and Measurement Modeling	52

3.2.1	Modeling 1st and 2nd Order Reflections	53
3.2.2	Adopted Signal Model	57
3.3	Joint Wall and Tag Localization	61
3.4	Experimental Evaluation	62
3.5	Conclusion	64
4	Bistatic - Multistatic Localization	66
4.1	Introduction	66
4.2	Problem Formulation and Phase Model	67
4.3	Ellipses based Method and Ambiguity Resolution	69
4.4	Elliptical DoA Estimation and Localization	76
4.4.1	Multistatic Elliptical DoA Estimation (ElIDoA)	76
4.4.2	Multistatic 2D Localization	77
4.4.3	Multistatic 3D Localization	78
4.5	Experimental Evaluation	80
4.5.1	Experimental Evaluation of ElIDoA vs MUSIC	82
4.5.2	Experimental Evaluation of 2D Localization Algorithms	83
4.5.3	Simulated 3D Localization Results	85
4.5.4	Conclusion	86
5	Wireless Sensor Network Interrogation and Path Planning	87
5.1	Backscatter Wireless Sensor Networks	88
5.1.1	WSN Deployments	88
5.1.2	Components	89
5.1.3	Interrogation Techniques	89
5.2	Path Planning Algorithms	90
5.2.1	Travelling Salesman Problem (TSP) Solution	90
5.2.2	Min-Waypoint Approach	92
5.3	Implementation and Results	95
6	Conclusion	99
6.1	Recapitulation	99
6.2	Major Findings and Achievements	99
6.3	Future Directions	100
6.4	Closing Remarks	101
	Bibliography	102

Chapter 1

Introduction

In recent decades, Radio Frequency Identification (RFID) technology, leveraging the principles of reflection radio, is becoming an increasingly pivotal domain in the wireless research community, especially in the context of localization. The ubiquity of Radio Frequency Identification technology has been on a dramatic rise, not merely due to its inherent utility, but also fueled by various technological advancements that have expanded its scope and improved its efficiency. This research delves deep into the nuances of RFID technology, with particular emphasis on RFID localization methods, and the broad spectrum of its applications, from agriculture to indoor tracking and beyond.

At the heart of RFID technology is the concept of backscatter radio [1–3]. At its basic form a reader communicates wirelessly with a single RFID tag. While the reader is an actively transmitting device, the RFID tag can be a passive, RF-powered unit, consisting of an antenna and a simple chip that controls the termination load of the antenna. The illuminating signal provided by the reader does not only provide an RF harvesting source for the tag’s power needs, but also serves as a medium for the tag to “piggyback” its payload. By switching between the different antenna termination loads, the tag can effectively alter the characteristics of the signal reflected back to the environment by its antenna similarly to how a flashlight and a mirror can be used to convey messages. This reflected signal can be then captured by the reader and through analyzing its characteristics the tag’s information can be obtained. The most prevalent standard defining the reader-tag communication is currently the EPC Gen2 (short for EPCglobal UHF Class 1 Generation 2) protocol [4].

The system architecture described above, where the device acts as both the illuminator and the receiver of the backscattered signal, is termed monostatic. In contrast to this monolithic approach, the bistatic and multistatic architecture are now introduced. Here, the roles of illumination and signal reception are being distributed among two or multiple

devices. Such decentralized system structures can provide certain advantages in signal clarity and range, but are also paired with their unique challenges. These architectures have attracted significant interest comparing and analyzing their potential [5, 6].

RFID’s ingenious approach of utilizing backscatter radio, significantly minimizes power consumption, rendering RFID particularly well-suited for environments that demand ultra-low-power operations, such as Wireless Sensor Networks (WSNs) [7, 8]. Over time, this principle has been employed in a plethora of scenarios, be it digital, FSK-based backscatter communication [9–11] or even analog backscatter radio-based WSNs [12–14]. Innovatively, pre-existing signals have even been used for RF illumination in backscatter radio-based WSN nodes, as documented in studies like [15, 16].

In the realm of RFID localization, one witnesses a surging interest, especially given the substantial improvements in tag sensitivity and range, as well as the affordability and availability of commodity readers. Multiple techniques that have emerged over the years are based on the Received Signal Strength Indicator (RSSI) [17–19], but phase-based [20–22] or hybrid phase-RSSI methods [23] stand out due to their precision. These techniques, predominantly aligned with monostatic architectures -where the transmitting and receiving antennas of the reader coincide- are associated with inherent distance ambiguities, which can be addressed using strategies involving varied wavelengths, increased bandwidth [24], or even reader mobility [20, 25]. However, challenges, such as estimating the reader’s location or the complexities induced by wireless multipath environments, remain [26].

While a plethora of projects has focused on static or stationary interrogation setups, quite recent developments have incorporated dynamic entities, like drones or UAVs. For instance, investigations into the use of unmanned vehicles for interrogating backscatter radio-based sensors/tags have surfaced, mostly leaning towards system-level optimization [27, 28]. Diverse applications, such as using UAVs to track other UAVs indoors via RSSI variations [29] or leveraging a differential Global Navigation Satellite System for outdoor RFID tag localization [30, 31], have been explored. The optimization of UAV operational parameters has also been a topic of keen interest [32, 33].

This dissertation embarks on an experimental exploration of UAV-based interrogation within a backscatter environmental WSN, specifically emphasizing its application in agriculture. By measuring various attributes across different points in a field using backscatter technology, we present a method that facilitates smarter agricultural decisions, optimizing resource distribution and thus promoting more sustainable farming practices.

However, the focus doesn’t rest merely on exploring and enhancing existing methods. This work presents novel techniques that challenge traditional notions, such as the com-

combination of phase and RSSI in a narrowband reader setup to counter multipath effects. Innovative applications, from robotic platforms employing SLAM for RFID reader measurements to particle filtering techniques for robust tag localization, have been explored in depth. The broader vision remains - to advance RFID technology, making it more versatile, accurate, and applicable in diverse scenarios.

In summary, this research journey traverses the rich tapestry of RFID technology, from its foundational principles to state-of-the-art applications, fostering a comprehensive understanding of its potential and paving the way for future innovations. The references and studies cited herein provide a testament to the vast body of knowledge that has been built over the years, yet the field remains ripe with opportunities for groundbreaking discoveries and transformative applications.

1.1 Applications of RFIDs

In this era of rapidly advancing digital connectivity, Radio Frequency Identification (RFID) has established itself as an innovative technology. At its core, RFID's ability to wirelessly identify, sense, localize, and track objects has transformed a myriad of sectors.

For instance, consider a sprawling retail warehouse [34–36]. In the past, inventory checks were labor-intensive, time-consuming, and prone to human error. With RFID, each item can be tagged, found and tracked in real-time, ensuring instantaneous inventory updates and facilitating swift restocking processes.

In healthcare settings [37–39], the implications are even more profound. Imagine a busy hospital where hundreds of critical equipment pieces, from heart rate monitors to syringe pumps, need to be tracked. RFID ensures that a nurse or doctor can instantly locate vital equipment, enhancing patient care and potentially saving lives. Moreover, RFID tags on medication bottles can ensure the right patient receives the correct dose at the necessary time.

Agriculture, too, has reaped the benefits of RFID [14, 40, 41]. On a vast farm, RFID tags on livestock can track an animal's health, location, and feeding patterns, ensuring optimal care. Additionally, RFID sensors in the soil can monitor moisture levels, helping farmers irrigate with precision and conserve water.

However, the journey of RFID adoption is not without its hurdles. The intricate environments in which RFID operates can introduce challenges. For example, in a packed supermarket, reflections from metal shelves or liquid products can distort RFID signals. Yet, understanding these effects can lead to refining RFID systems, making them even more resilient and accurate.

The fusion of RFID with other technologies unlocks additional potential for innovation. When combined with Wireless Sensor Networks (WSNs), the possibilities expand exponentially. For instance, in a vineyard, an RFID-backed WSN can monitor soil nutrients, ensuring each grapevine gets tailored care, leading to better wine quality.

The technical challenges posed by such integrations are manifold. Deploying an RFID system in a bustling library, where thousands of books need tracking, or in a multi-tiered warehouse demands a blend of software and hardware expertise. This dissertation's exploration of the synergy between RFIDs, robotics and WSNs aims to navigate these complexities, offering robust real-world solutions for diverse problems and applications.

As we journey further into this dissertation, we will traverse the intricate and promising landscape of RFID, unveiling its transformative potential in detail.

1.2 Motivation

The allure of RFID's such promising capabilities, while significant, is juxtaposed with a labyrinth of technical intricacies. The drive behind this work is to study, understand and solve such problems in order to achieve accurate and reliable systems equipped to overcome challenges arising from these real-world applications. As it was already mentioned, reflections from environmental objects, known as multipath effects, emerge as formidable adversaries, warping the electromagnetic fields upon which RFID hinges. Yet, the horizon of challenges extends further. As we intertwine RFID with other avant-garde technologies, such as robotics and Wireless Sensor Networks (WSNs), we not only amplify its capabilities, but also inherit unique challenges from each domain. This fusion of potential and pitfalls has been the catalyst driving our deep dive into the RFID universe.

Specifically, we wanted to engineer a system capable of pinpointing objects with precision within expansive environments, like warehouses or libraries. Recognizing the value of high-resolution 3D localization for tasks, like inventory management or locating misplaced items, we envisioned a system that marries accuracy with economic efficiency. Since covering such a large area with multiple readers would be economically inefficient and unfeasible, we wanted to explore the concept of a singular, mobile monostatic reader that is able to move along the corridors of the area of interest. To satisfy the mobility requirement we decided to employ a robotic platform on which the reader would be integrated. The mobility factor was not merely a solution, but an opportunity in disguise. The localization techniques devised for the moving reader leverage the motion of the reader/antenna over a target region to provide finer estimates than conventional stationary systems. The distance the device travels creates a larger synthetic antenna

aperture. Typically, the larger the aperture, the higher the accuracy will be. An added benefit of the RFID versus the traditional optical systems is that the targeted objects can be hidden behind other obstacles and can be localized even when the direct line of sight path is obscured.

During the development of this system, we analyzed and identified the main cause of error to be the multipath propagation effect, where the usually dominant and of interest line of sight signal component is perturbed by signals originating from environmental reflectors. While we managed to limit its influence on our system, we wanted to study the nature of these reflections, as well as model their effects and even estimate their origins, so we can improve the localization ability of our system.

Another area of interest for our research was the bistatic/multistatic architecture and its inherent advantages and challenges. Instead of scattering multiple stationary monostatic readers, we explored the potential of the multistatic architecture, capitalizing on its extended coverage range and intrinsic geometric advantages. The goal was to devise a stationary system for localizing RFID tags, alleviating the complexities of having a physically moving platform.

We also wanted to explore the synergy of backscatter radios with WSNs, particularly spotlighting their potential in precision agriculture. To harness the cost-effectiveness and energy efficiency of these sensors, we integrated a UAV drone with a single-board computer and a light-weight software-defined radio. This approach was our answer to the limited communication range of these sensors in relation to the large-scale deployments studied. We sought to understand how such a UAV-backed system would stack up against a traditional, pedestrian reader-equipped counterpart, both designed for tasks, like monitoring soil moisture, in expansive agricultural setups.

1.3 Technical Preliminaries - ROS, Robotic Platform and Drone

Before we delve deeper in the algorithms and techniques developed during this work, let us first examine the equipment used, the technical challenges involved with it, as well as the engineering solutions that were devised to solve them.

1.3.1 ROS

In the realm of robotics, systems are inherently intricate, comprising a multitude of interconnected subsystems that need to operate in harmony to achieve specified tasks. These

subsystems must not only communicate efficiently for real-time data exchange and action planning, but also facilitate the seamless integration of new modules. The challenge of orchestrating this complex interplay is elegantly met by the Robot Operating System (ROS) [42], a middleware framework that has become the de facto standard in the robotics community.

ROS employs a modular architecture, where the code is organized into discrete entities, known as Nodes. Each Node functions as an independent process and is designed to perform a specific task. For example, one such Node is explicitly programmed to interact with Hokuyo's Light Detection and Ranging (LiDAR) system, whose responsibility is to collect laser scan data and publish it to a pre-defined Topic within the ROS ecosystem. Nodes communicate among themselves through two primary mechanisms: Topics and Services.

Topics serve as communication channels for message passing, allowing Nodes to publish or subscribe to them. Importantly, the architecture supports a many-to-many relationship; a single Node can publish or subscribe to multiple topics, and conversely, multiple Nodes can publish or subscribe to the same topic. Messages encapsulate structured data that is being exchanged, conforming to predefined message types that ensure consistency and interoperability.

Services, on the other hand, enable a Node to invoke functions or routines in another Node. This provides a synchronous form of communication and allows for more complex interactions beyond simple data passing. Services enable Nodes to request specific actions from other Nodes, essentially acting as function calls across the network.

One of the compelling advantages of ROS is its broad-based industry support. Manufacturers of a wide range of devices designed for robotic applications routinely provide ROS-compatible packages, thus eliminating the need for developers to create bespoke drivers for each new piece of hardware. This consolidation under a single Application Programming Interface (API) dramatically simplifies the development process, accelerating both deployment and subsequent iterations.

Moreover, ROS offers a suite of powerful utilities and tools aimed at enhancing various aspects of the robotic software development lifecycle. This includes capabilities for data visualization, logging, and playback, as well as robust simulators for testing and debugging in a virtual environment. Originating from Stanford University and first released in 2007, ROS has continued to evolve, offering a versatile and rich set of features that have contributed to its widespread adoption as the middleware framework of choice for robotics software development.

1.3.2 Robot Setup Description - The Turtlebot2 Platform



Figure 1.1: The default configuration of the Turtlebot2 platform.

The Turtlebot platform is an accessible, cost-effective solution tailored for educational and research initiatives in cutting-edge robotics. Conceived by Melonee Wise and Tully Foote at Willow Garage in November 2010, Turtlebot offers a comprehensive kit that includes a mobile base, a 3D sensor, a computing unit, and a modular stackable structure to which additional components can be attached. Its software is open-source, and the platform is deeply integrated with the Robotic Operating System (ROS), with numerous pre-configured ROS packages readily available to expedite development and research activities.

The inaugural version of Turtlebot utilized the iRobot Create as its mobile base, which itself was an enhanced derivative of the iconic Roomba robotic vacuum cleaner. The second generation of Turtlebot (Turtlebot2) which is used in this work (Fig. 1.1, transitioned to a Kobuki Base manufactured by Yujin Robot. The updated base represented a qualitative leap, featuring additional capabilities, such as analog input options, an increased number of power connectors, touch-sensitive buttons, indicator LEDs, and an improved battery life, thereby expanding the range and flexibility of experiments and applications that could be undertaken.

At the core of our robotic system lies the Kobuki Mobile Base, which serves dual functionalities: it governs the locomotion of the robot, while also functioning as a power hub for the supplementary modules integrated into the system. The Kobuki base is energized by a 4S2P Lithium-Ion battery pack, with a nominal voltage of 14.8 V and a capacity of 4400 mAh. According to the manufacturer's specifications, this battery is capable of sustaining the robot's operations for an impressive duration of up to 7 hours.

Our empirical experience with the system corroborates this claim, confirming its efficacy and reliability.

To facilitate the seamless integration and operation of auxiliary modules, the Kobuki base is equipped with an array of specialized power connectors designed for various sub-systems:

- 19 V / 2 A: Intended for laptop power supply. This connector is active only when the base is plugged in for charging and is hence unavailable during autonomous operation.
- 12 V / 5 A: Allocated for powering high-consumption peripherals, like a robotic arm. In our system, we employ this port to energize all of our 12 V modules via a custom-designed power distribution board.
- 12 V / 1.5 A: Initially intended for the Microsoft Kinect power supply. In our configuration, as we do not use Kinect as our 3D sensor, this port is repurposed to accommodate DC-to-DC converters, enabling us to derive diverse voltage levels to meet our specific requirements.
- 5 V / 1 A: Serves as a general-purpose power supply port.

From a mechanical standpoint, the Kobuki base employs a differential drive system, consisting of one wheel on each lateral side. Each wheel is propelled by a geared motor and incorporates a built-in encoder. This setup allows for a maximum translational velocity of 70 cm/s and a rotational velocity ceiling of 180 deg/s. Additionally, the base can comfortably support payloads weighing up to 5 kg.

Moreover, the Kobuki base is furnished with a suite of sensing elements to enhance its autonomous navigation and interaction capabilities. These include a factory-calibrated single-axis gyroscope for orientation tracking, three bump sensors strategically positioned for collision avoidance, a trio of cliff sensors for drop-off detection, and a wheel drop sensor in each wheel to monitor the integrity of wheel movements.

Furthermore, the base provides a range of programmable Input/Output (I/O) interfaces to extend its capabilities. These include four analog inputs, four digital inputs, and four digital outputs. For enhanced user interaction and debugging, the base also includes two bi-color LEDs and three touch-sensitive buttons. Data communication with external computing platforms is facilitated through a USB port.

The orchestration of these myriad functionalities is controlled by an STM 32-bit microcontroller, which serves as the computational brain of the Kobuki base. Overall, the

Kobuki Mobile Base offers an intricate yet highly integrated platform, adept at providing both mobility and power distribution functionalities, thereby serving as an ideal cornerstone for versatile robotic systems.

1.3.3 Robot Setup Description - Added Components

2D LiDAR Sensor



Figure 1.2: Hokuyo UST-20LX mounted on Turtlebot.

For distance measurement and environmental mapping, our robotic system employs a Hokuyo UST-20LX, a sensor that operates based on Light Detection and Ranging (LiDAR) technology. It is a 2D laser scanner, capable of performing these measurements across multiple angles within a 270° field of view. The angular resolution of the device is 0.25° , and it offers a detection range spanning from as close as 0.06 m up to 20 m, with an accuracy of ± 40 mm. Its specifications allow the device to be powered directly by the Kobuki Base without requiring any adaptors. For data communication with the computing system, the Hokuyo UST-20LX comes equipped with an Ethernet interface and a ROS node responsible for its management.

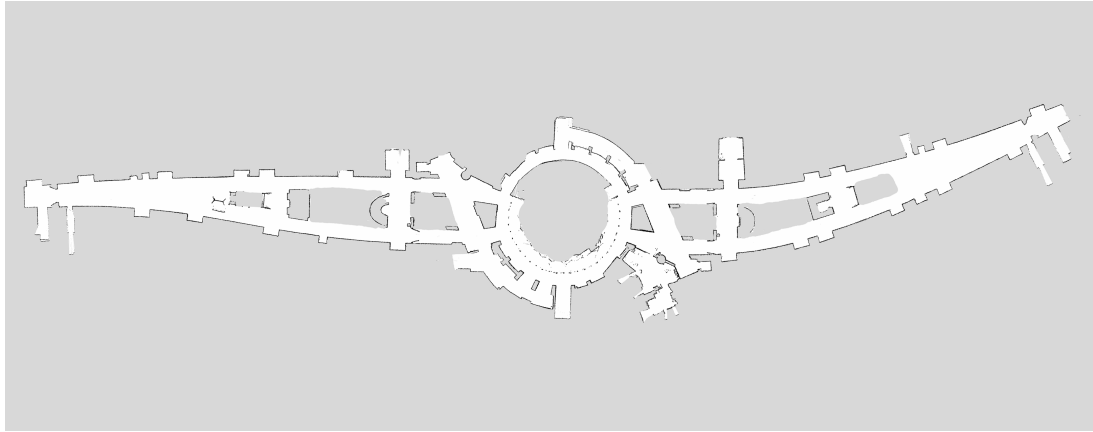
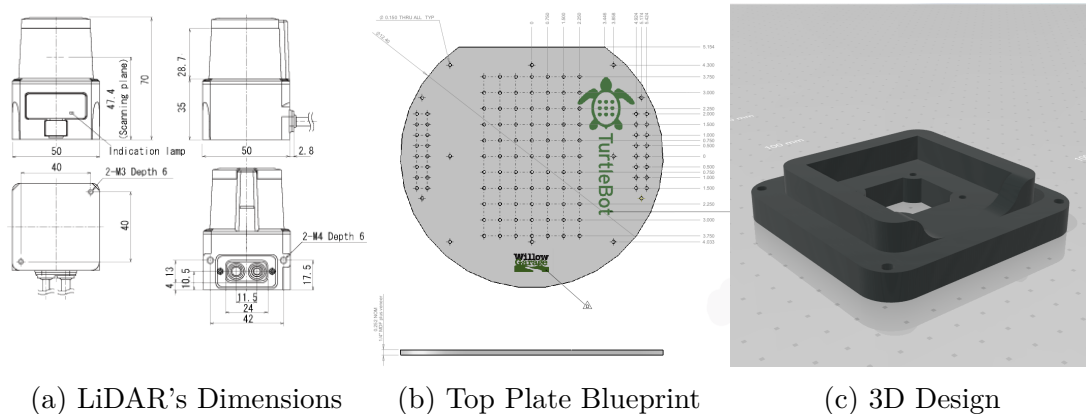


Figure 1.3: Ground floor mapping of TUC's School of ECE building using SLAM.

This sensor is intended to be positioned on the top mounting surface of the Turtlebot platform, but the pre-existing hole grid pattern on this surface (Fig. 1.4b) was not congruent with the mounting holes on the Hokuyo UST-20LX LiDAR (Fig. 1.4a). To reconcile this discrepancy without modifying either the Turtlebot platform or the LiDAR, a custom base was designed (Fig. 1.4c) to accommodate both the specific dimensions of the LiDAR device and the grid pattern of the Turtlebot's mounting surface, ensuring a stable and secure installation. The base was materialized using a 3D printer, so it was designed with these limitation in mind.



(a) LiDAR's Dimensions (b) Top Plate Blueprint (c) 3D Design

Figure 1.4: LiDAR's base design and schematics.

3D Depth Camera



Figure 1.5: The Orbbec Astra camera module.

In our efforts to extend the robot's depth perception capabilities to the 3D space, we integrated an Orbbec Astra Camera. Beyond its depth-sensing prowess, the Orbbec Astra Camera is equipped with an RGB image sensor, thereby offering the dual capability of capturing colorized images alongside depth maps. Both the depth and RGB images furnished by the Astra Camera boast a resolution of 640×480 pixels. Additionally, the camera offers a comprehensive Field of View measuring $60^\circ\text{H} \times 49.5^\circ\text{V} \times 73^\circ\text{D}$, ensuring expansive coverage of the environment. When it comes to the range of object detection, the camera can detect objects situated between 0.6 m and 8 m. Lastly, in terms of its power requirements and communication, the Astra Camera operates using a USB 2.0 connection, ensuring easy integration.

In essence, the incorporation of the Orbbec Astra Camera within our robot not only enhances its perceptual capabilities, but also enables a more nuanced understanding of its environment, aiding in tasks ranging from navigation to object recognition and interaction. Namely, its depth sensing capabilities were used in order to avoid collisions with unexpected objects in the 3D space (not present in the LiDAR's 2D plane of sensing), human avoidance, while also providing information of the status (open, closed) of doors that the robot is required to navigate through.

RFID Tag Reader



Figure 1.6: The Impinj Speedway R420 RFID reader.

The RFID reader that was mainly used in this work is an Impinj Speedway R420 monostatic 4-port reader. Its maximum transmission power is limited by the EU1 regulations at 31.5 dBm, while it is operating in the UHF 868 MHz band. It requires though a 24 V DC power supply, which was achieved using the 12 V rail of the Kobuki base along with a DC/DC converter.

In terms of establishing a communication link with the device, our decision tilted towards the Ethernet connection. This choice was driven by the Ethernet's inherent benefits of simplicity combined with rapid data transfer capabilities. On the software communication front, however, challenges arose. At the time of our implementation, the accessible firmware, the predominant resource available, was an LKT C++ library. Unfortunately, this posed compatibility issues with our ROS environment.

To address this issue, we developed a parameterised C++ code using a gcc version compatible with the library and compiled an executable. In order to incorporate this executable to our ROS environment, we introduced a python-based ROS node that served as a communication wrapper. Its function was to efficiently manage the aforementioned executable. By doing so, it ensured that data from the R420 reader was constantly available and easily accessible to other ROS nodes integral to our work, notably the localization node.

In the process of enhancing the data integrity and accuracy of our system, a pivotal step involved fine-tuning the synchronization between the measurement's timestamp and the corresponding position at which it was taken. Given the intricacies involved in ensuring precise time synchronization between multiple devices in a networked environment, the Network Time Protocol (NTP) emerged as an indispensable tool.

The NTP configuration was set up on the RFID reader. This protocol was used to ensure that the reader's internal clock was aligned accurately with a reference time source. In order for the reader to access the NTP server, the on-board computer's internet connection was shared with the reader. By doing so, we were not only able to provide the reader with access to reliable time servers, but also ensured a consistent internet environment for both the on-board computer and the reader.

With both units accessing the same time reference, the resultant effect was a marked improvement in the synchronization, effectively minimizing any potential discrepancies that could arise from misaligned time data. While this optimization greatly improves the performance and reliability of our system, it is important to note that alternative methods for synchronization can be implemented without the need of an internet connection.

Ethernet Switch



Figure 1.7: The Cisco SG110D-08 Ethernet switch.

Typically, devices like our computing unit come equipped with a singular Ethernet port. While this is adequate for most standalone applications, our setup necessitated the integration of multiple Ethernet-enabled devices. The easiest solution to this problem was the inclusion of an Ethernet switch, which would expand the number of available Ethernet connections, thus accommodating multiple devices.

In our case, we used the Cisco SG110D-08 Ethernet switch, an 8-port switch which provided the capacity to connect up to seven additional devices (besides our computing unit). This flexibility not only catered to our present needs, but also left room for potential future expansions or integrations.

The Cisco SG110D-08 switch has a power specification of 12 V DC, which matches our Kobuki base's 12 V rail, making it a perfect power source for the switch. By connecting the switch directly to the Kobuki's 12 V rail, we ensured a seamless and efficient power supply, minimizing the need for additional external power sources or adapters.

Incorporating the Ethernet switch into our platform, thus, effectively streamlined the communication pathways between our computing unit and other networked devices. This also allows easy access to the computing unit for programming and debugging purposes

by connecting an external computer to the system using one of the available Ethernet ports. The end result was a robust, interconnected system with enhanced communication capabilities, prepared to handle the challenges of our intricate networking needs.

Antennas and Mounts

In our series of experiments involving the robotic platform, the antenna of choice was consistently the FlexiRay SF-2110 model. This antenna has a gain of 5 dBi, while being really compact and lightweight, making it especially suitable for mobile robotic applications.

Given the experimental nature of this work and the need for flexibility, the mounting mechanism of the antennas on the robot was crucial. We employed wooden poles of either one or two meters in length, which were attached to the robot. These poles were anchored securely using specially designed 3D printed sockets (Fig. 1.8). These sockets were designed for easy installation and removal, enabling quick modifications and adjustments to the setup as needed.



Figure 1.8: The 3D printed pole mounting adapter (red).

To fix the FlexiRay SF-2110 antenna onto the wooden poles, a bespoke 3D printed holder was conceived. This holder, combined with crafted adapters and mounts, ensured that the antenna remained firmly in place, even when the robot was in motion. While the design of the mounts was pretty sturdy, due to the new increased height to width ratio of the robot, the chassis of the robot started flexing. This flexing resulted in an oscillation of the wooden pole (especially the 2 meter one) that inevitably introduced some extra error to the antennas' location estimate.

But beyond just stability, we prioritized adaptability in our design approach. Our mounting mechanism was designed to be modular. This feature proved invaluable as it

permitted the orientation of the antennas to be easily changed. With the incorporation of a 90-degree adapter (leftmost bottom component of Fig. 1.9a), the antennas could be quickly repositioned to suit specific experimental conditions or objectives. Furthermore, this modular design is well-prepared to accommodate such potential future additions, ensuring that our robotic platform remains flexible and adaptable.



(a) Antenna holder, adapter and mounting bracket. (b) The whole assembly mounted on the robot.

Figure 1.9: The pole/antenna mounting system.

Computing Unit

In order to communicate with the array of peripheral devices and the Kobuki base's control unit, while also processing sensor data, executing SLAM, and running localization algorithms, a central computing unit is required. This unit, functioning as the brain of the system, should be capable of running Linux OS, which is required to setup the ROS environment and could be a single-board computer, a mini PC, or a laptop.

At the beginning, a small laptop was employed as this central computing unit. However, recognizing the potential for enhanced efficiency and compactness, we transitioned to the Intel NUC7i5BNH mini PC. This computer is equipped with a 2.2 GHz Intel i5 processor, 8 GB of RAM, and a 120 GB Solid State Drive, ensuring rapid data access and storage.



Figure 1.10: The Intel NUC7i5BNH mini PC.

Considering power requirements, the NUC demands a voltage in the range of 12-19 V DC. It peaks at a power consumption of 50 W, but a 20-30 W consumption is required under normal operational conditions. While the Kobuki's 12 V 5 A power rail could theoretically sustain such a load, real-world application proved otherwise. The concurrent connection of multiple devices to the same rail, combined with sudden power surges from the robot's motors, dipped the voltage low enough to crash the PC and rendered this power source inadequate.

Our remedy to this problem involved the repurposing of a compromised 6s2p LiPo battery, which was reconfigured into a 4s2p after the removal of the defective cells. This rejigged battery setup can consistently deliver voltages between 16.8 V (maximum) and 14.8 V (15% threshold below which the battery might sustain irreversible damage). Such voltage parameters comfortably fall within the NUC's operational requirements. Extrapolating from a power scenario where the PC operates at its maximum performance, the current draw is approximately:

$$I = \frac{P}{V} = \frac{50 \text{ W}}{15.8 \text{ V}} \approx 3.1646 \text{ A.} \quad (1.1)$$

Drawing upon the battery's nominal 17,000 mAh capacity (considering a 15% reduction for longevity), the prospective battery runtime can be estimated:

$$\text{Battery Runtime (hours)} = \frac{17 \cdot 0.85 \text{ A}}{3.1646 \text{ A}} \approx 4.57 \text{ hours.} \quad (1.2)$$

These calculations reflect our empirical observations. In real-world scenarios, where the PC seldom harnessed its full potential, the battery consistently exceeded an 8-hour runtime. To further achieve battery longevity and efficiency, a Battery Management

System (BMS) was integrated. This ensures load distribution across the cells and offers over-discharge rate protection. Additionally, to preempt any inadvertent power depletions, a typical Remote-Control (RC) low battery beeper system was installed, sounding an alarm upon detecting a specified low voltage level.

The addition of this battery system, besides providing an extended and reliable power source for the computing unit, also increased the overall runtime of the platform as a whole, since less systems have to rely on the base's batteries.

To facilitate interactions with the computing unit, a dual-method communication approach was employed. Primarily, Secure Socket Shell (SSH) was utilized, serving as a robust and secure means of command-line-based interaction. This mode was particularly efficient for direct, pre-programmed tasks and allowed quick access without the need for a comprehensive graphical interface.

However, in scenarios demanding a visual interface – be it for intricate software adjustments, real-time data visualization, or troubleshooting – a remote desktop application was preferred. An intriguing quirk associated with this application necessitated the use of an HDMI dummy plug. This plug, when inserted into the computer's HDMI slot, mimics the presence of a physical monitor. Without this, the remote desktop application faced challenges in rendering the desired visual environment.

To complement these remote access methodologies and enhance onsite responsiveness, a wireless mini keyboard was integrated into the setup. This device gave operators the ability to manually control the robot's movements with precision when necessary. More crucially, it acted as a safeguard, ensuring that in unforeseen circumstances or system hiccups, there was always a direct means to regain control or halting the robot's movements.

Augmenting the platform's range of feedback capabilities, an audio system was introduced in the form of a speaker. Through this speaker, the platform could provide users with real-time audio feedback, while also enabling it to solicit assistance for tasks beyond its capability, like requesting someone to open a door. This addition enhanced the robot's ability to operate in human-centric environments, while avoiding expensive and complex requirements like a robotic arm.

1.3.4 Drone Setup Description - The Drone Platform

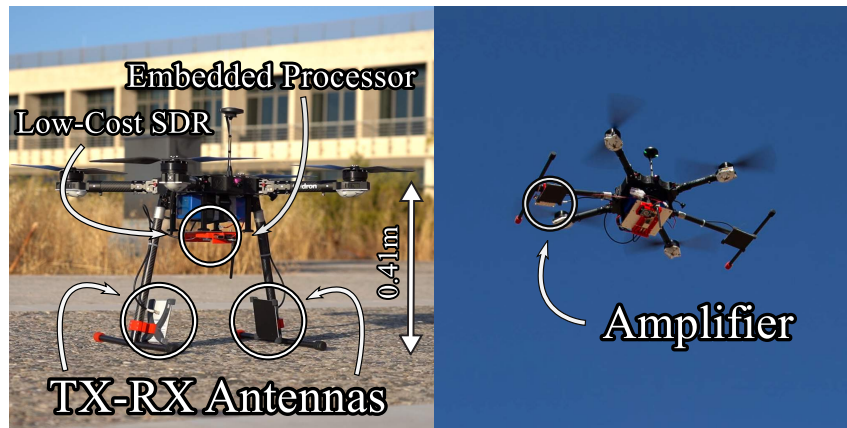


Figure 1.11: The drone platform along with the added components on the ground (left) and during flight (right).

The primary drone utilized throughout our research is the Italdron EVO4HSE (Fig. 1.11). This drone stands out for its advanced features and adaptability to a diverse range of experimental settings. The Italdron EVO4HSE operates using the Pixhawk 4 flight controller, which is powered by the versatile Ardupilot software.

It was powered by a high-capacity 377 Watt-hours LiPo battery that ensures prolonged flight times and reliable performance, while also providing a power source for additional components essential for our research activities.

Designed with adaptability and user-convenience in mind, the Italdron EVO4HSE boasts a highly transportable system. Its arms fold quickly, making it efficient for transportation and deployment. Furthermore, this drone is crafted to withstand environmental challenges; its design is resistant to both dust and humidity, enhancing its durability in varied field conditions.

Another impressive attribute of the Italdron EVO4HSE is its payload capacity. It can comfortably carry and transport up to 2.5 kilograms, making it versatile for a plethora of applications. Whether it is research tools or sensors, the drone can be easily adapted to cater to different experimental needs.

In environments known for high electromagnetic densities, the robustness of a drone's datalink is crucial. The Italdron EVO4HSE excels in this regard with a resilient datalink that ensures safe and uninterrupted operations, even in challenging electromagnetic scenarios.

The drone's motor-propulsive units are notable for their efficiency and reactivity. Ensuring optimal performance and longevity, these units undergo rigorous quality checks.

The drone is also replete with features designed to maximize safety and mitigate risks. Some of these integral safety measures include the return-to-land function, geofencing, proximity sensors, and many more. These features provide operators with peace of mind, knowing that the drone is equipped to handle unforeseen circumstances.

One of the best features of the Italdron EVO4HSE is its modular design. This design philosophy facilitates easy integration with both pre-market and after-market technologies and accessories. This adaptability was particularly beneficial for our research, as it permitted the seamless installation of various additional modules on the drone's body, tailored to our specific experimental requirements.

1.3.5 Drone Setup Description - Added Components

Single-Board Computer



Figure 1.12: The Odroid-XU4 single-board computer.

The Odroid-XU4 single-board computer was selected to serve as the processing unit for our system (Fig. 1.12). While the Pixhawk 4 controller exclusively managed the drone's navigation, the Odroid-XU4 undertook a broader array of responsibilities.

The Odroid-XU4 is a new generation of computing device with powerful, energy-efficient hardware and a minimalistic form factor. Offering open source support, the board can run various flavors of Linux, including the latest Ubuntu 20.04 and Android 7.1 Nougat. By implementing the eMMC 5.0, USB 3.0 and Gigabit Ethernet interfaces, the ODROID-XU4 boasts amazing data transfer speeds, a feature that is required for the needs of our application.

To physically integrate the Odroid-XU4 with our drone, a custom 3D printed mount was designed and crafted to position the computer on the drone's underside. This mounting solution allowed easy access to the Odroid's ports for programming and debugging.

Furthermore, it was designed with the ability to accommodate a full-sized LimeSDR. For instances requiring the LimeSDR mini, a bespoke adaptor was crafted to ensure compatibility. A significant attribute of this case was its design consideration for the LimeSDR's relatively delicate ports. By integrating a dedicated bracket, it firmly anchored the connected cables, ensuring they remained securely affixed and reducing undue strain on the ports.

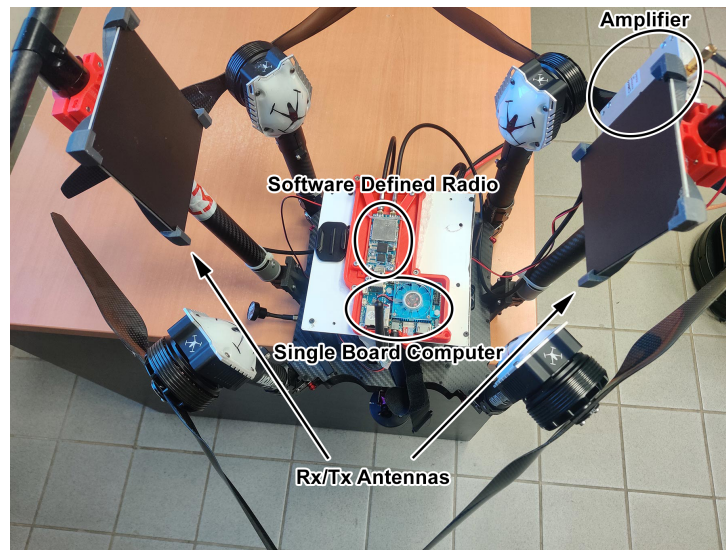


Figure 1.13: The underside of the drone with collapsed wing-arms featuring the mounting system, the Odroid, the LimeSRD mini, the amplifier and the antennas with their brackets.

The Linux-powered Odroid-XU4 unveiled a plethora of operational capabilities. Key among these was the capability to run GNU Radio, an essential tool for overseeing the software-defined radio (SDR) and subsequently processing the received data. Beyond this primary role, the single-board computer had an auxiliary function — facilitating communication. It was entrusted with the task of dispatching the processed data back to our base station, achieved through a custom ad-hoc WiFi link. Although this communication link was not imperative for the system's core functionality, it enabled real-time feedback giving operators live updates. Additionally, it empowered users with the capability to dynamically control the Odroid, truly exemplifying the term “on-the-fly” adjustments.

Software-Defined Radio

In order to fulfill our on-board radio requirements the aforementioned LimeSDR was utilized. The LimeSDR is a low-cost, open-source software-defined radio (SDR) platform that can be used to support just about any type of wireless communication standard. LimeSDR can send and receive UMTS, LTE, GSM, LoRa, Bluetooth, Zigbee, RFID,

and Digital Broadcasting. The LimeSDR Mini is a smaller, less expensive version of the original LimeSDR. However, it still packs a punch – at its core, the LimeSDR Mini uses the same LMS7002M radio transceiver as its big sibling. The Mini has two channels instead of four, SMA connectors instead of micro U.FL connectors and features Intel’s MAX 10 FPGA.

The full-scale LimeSDR served as the foundation upon which our system was designed and subsequently tested. Since the requirements of the system can be fulfilled by the SDR mini, the adaptor and the mini were used, since it reduces the cost of the overall system, as well as its lower power consumption increases battery lifetime.



Figure 1.14: The full-scale LimeSDR (left) and its smaller counterpart LimeSDR Mini (right).

RF Components

For the RF components required in this setup, two Flexiray SF-2110 antennas were used along with a Mini-Circuits ZRL-1200+ amplifier for the illumination chain. It was powered using a DC step-down converter directly connected to the drone’s battery, while for the rest of the components, a 5 V rail provided by the drones board was used.

The antennas were mounted using the previously created 3D printed holders and were attached on the drone’s lower part of the legs using custom-designed 3D printed brackets. Leveraging the drone’s ability to retract its legs in a horizontal position, the antennas, while having a horizontal orientation when the drone is on the ground, point to the ground when the legs are retracted. The increased distance of this position also helps with the decoupling of the antennas that is beneficial in the monostatic interrogation architecture used.

1.4 Roadmap

This dissertation embarks on a comprehensive exploration of the vast landscape of RFID technology. Our journey commences in Chapter 2, where we delve into the nuances of monostatic localization, leveraging a moving platform approach that harnesses phase measurements from diverse positions.

Building upon the insights garnered, we probe deeper into the constraints that limit localization precision within RFID systems. Notably, multipath propagation—arising from environmental reflectors—stands out as a predominant factor and is further studied in Chapter 3. While foundational research in other domains laid the groundwork for this part of our research, our application to commercial RFID systems and their subsequent limitations, marks a pioneering endeavor in the field.

Transitioning to Chapter 4, we shift our focus from the monostatic interrogation architecture to the bistatic-multistatic architecture. Leveraging its unique geometric properties, we explored an alternative method of tag localization without the need of antenna movement.

In Chapter 5, our narrative follows the intersection of RFIDs and Wireless Sensor Networks, studying the role and considerations surrounding interrogation architectures based on specific implementation parameters and needs.

A hallmark of our dissertation is the tangible, avant-garde experimental studies accompanying each chapter, resulting in near-market-ready systems primed for real-world deployments. A standout application manifests in the realm of robotics, where the Robotic Operating System (ROS) is employed to form a mobile interrogation and localization system. This system boasts the capability to pinpoint RFID tags with remarkable precision in complex environments, be it an office, library, or warehouse setting. Conversely, our bistatic architecture, devoid of movement, assures accurate tag localization under specific proven conditions, while its multistatic extension can augment area coverage. Completing our exploration, the UAV-based interrogation seamlessly merges with WSNs in an agricultural context, emerging as a valuable tool for monitored precision agriculture.

1.5 Thesis Contributions

Our research is a harmonious blend of theoretical exploration and practical realization. At its foundation, our work was steered by a theoretical study of signal characteristics, encompassing both monostatic and multistatic architectures. Additionally for the monostatic case, we studied the influence of a reflective surface by adopting and expanding

on compressive sensing formulation typically used for wideband through-the-wall-radar-imaging.

Transitioning from theory to practice, we undertook the formidable task of implementing our theoretical findings. This transition reinforced the real-world utility of our work, but was marked by a series of engineering challenges, each demanding a unique mixture of technical expertise and innovative problem-solving. Additionally, we managed to couple RFID with WSNs to provide valuable tools for precision agriculture and monitoring.

From optimizing the UAV-based interrogation of backscatter WSNs to ensuring seamless integration of RFID with robotic platforms, every challenge was met with a robust solution, underscoring our commitment to pushing the boundaries of what's possible with low-cost, narrowband, commodity-level equipment.

- Our exploration of the monostatic architecture led to the integration of a mobile reader with a robotic platform, capable of autonomously navigating the area of interest to localize tags. This market-ready system boasts an impressive real-time localization performance, registering a mean absolute error of merely 2 cm in 2D line-of-sight scenarios and an impressive 24 cm in 3D-search within cluttered domains.
- Our deep dive into reflections yielded an innovative methodology for the joint estimation of both tag and reflector locations, sans any prior knowledge. This innovative approach can pinpoint a reflector's position with remarkable accuracy, on the order of 5 cm.
- For the multistatic architecture, using a stationary reader setup, we offered a novel direction of arrival estimation technique, whose performance is on par with state-of-the-art techniques. Furthermore, our alternative localization method can offer an accuracy of 9 cm in 2D localization scenarios.
- Merging RFID and WSNs, our experimental system emerged as an example of cost-effectiveness, simplicity, and efficiency. This system effortlessly monitors a backscatter-based environmental WSN, effectively measuring the status of any capacitance-based sensor.

In summary, our work stands as a testament of the symbiotic relationship between theoretical mastery and hands-on engineering. Not only did we illuminate the lesser-known facets of the RFID paradigm through our theoretical explorations, but also manifested these insights into tangible, real-world applications. This harmonious confluence of theory and practice, interwoven with the myriad of engineering challenges we surmounted, sets our research apart, marking a significant milestone in the RFID arena.

Chapter 2

Monostatic Localization with a Robotic Platform

Radio-frequency identification (RFID) technology carries the potential to alter a myriad of sectors, from supply chain management to healthcare, and from agriculture to environmental monitoring. At the heart of this transformative potential lies the capability of RFID systems to enable identification, localization, and tracking of objects in real-time using wireless communication. Localization, in particular, plays a crucial role in applications, such as inventory management, indoor navigation, and asset tracking. However, in complex environments where signal interference is prevalent, the reliability and accuracy of RFID-based localization face significant hurdles.

Multipath propagation epitomizes these challenges. As radio signals from an RFID tag bounce off surfaces, such as walls and furniture, they forge numerous paths to reach the RFID reader. This scattering can cause significant phase alterations, wreaking havoc with tag localization. This issue urgently calls for an innovative, effective solution.

Most traditional RFID localization techniques rely on Received Signal Strength Indicator (RSSI) measurements to estimate the tag's location. However, the RSSI is often greatly affected by environmental factors, such as obstacles and signal attenuation, which makes it less reliable in complex environments. To overcome these challenges, phase measurement-based localization has proven to be the dominant approach in RFID systems. Phase measurements provide information with greater granularity than signal strength, allowing for more precise and robust localization in all sorts of environments. By analyzing the phase of the received RFID signals, it becomes possible to estimate the distances between the RFID tags and the reader, enabling precise location determination.

It is important to acknowledge that phase measurement-based localization also has its own disadvantages and challenges that need to be addressed. Phase measurements exhibit

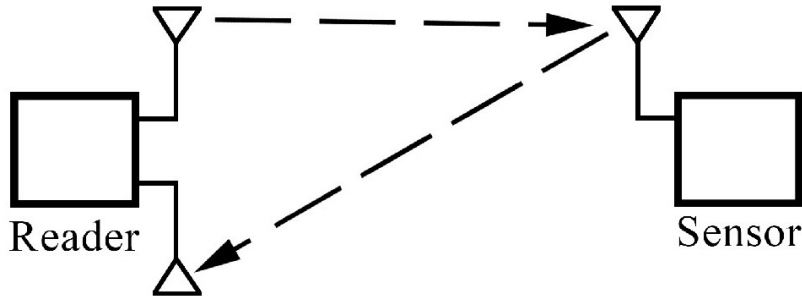


Figure 2.1: Single Reader Architecture

a periodic nature due to the sinusoidal properties of RF signals. This periodicity can lead to ambiguities, where a single phase value corresponds to multiple physical distances. Additionally, phase measurements can be sensitive to factors, such as tag orientation, environmental changes and electronic components, which can introduce errors and affect the accuracy of localization. Therefore, careful calibration and advanced signal processing techniques are required to mitigate these challenges and achieve reliable and accurate localization results. By addressing these concerns, the potential of phase measurement-based localization can be fully harnessed, leading to significant advancements in RFID localization capabilities.

Particle filters are a powerful computational tool for estimating the state of a system, especially when dealing with nonlinearities and non-Gaussian noise, attributes commonly associated with multipath propagation in RFID systems. By coupling these phase-based particle filters with the mobility and adaptability of a robotic system, we aim to create a dynamic system capable of handling the uncertainties inherent in multipath environments.

In the sections that follow, we will delve into the specifics of our approach, starting with a detailed examination of the phase model used in multipath environments. We will then explore the intricacies of phase-based particle filtering and discuss the role a mobile robot plays in the localization process. Through this focused approach, our goal is to significantly enhance the accuracy and reliability of RFID localization systems in multipath environments.

2.1 RFID Systems: Monostatic Architecture, and Phase-Based Distance Estimation

RFID systems constitute a significant technology in the realm of object localization and tracking. A typical RFID system consists of two main components: an RFID tag attached

to the object of interest, and an RFID reader which communicates with the tag via radio waves. The tag modulates its data on to these radio waves and reflects them back to the reader, providing information about the tag's identity and potentially sensor data.

There are two primary architectures for RFID systems: monostatic and bistatic. In a monostatic system, a single antenna/device is used for both transmission and reception of signals. In contrast, a bistatic RFID system utilizes separate antennas/devices for signal transmission and reception.

This chapter specifically adopts a monostatic architecture for its RFID system. In a monostatic system, the same direct signal path is used for both transmission and reception. This means that the Line of Sight (LoS) component, which refers to the signal that travels directly from the tag to the reader, is easier to isolate and analyze. This becomes particularly beneficial, when adopting a phase-based approach to RFID localization.

While conventional RFID localization techniques often rely on Received Signal Strength Indicator (RSSI) measurements, we focus on the phase of the signal. The phase, unlike the signal strength, is typically less affected by environmental factors and, with appropriate analysis and considerations, can offer improved accuracy in localization.

In this research, we concentrate on developing a joint phase-based model for the LoS component and all the indirect components of the RFID signal as well as the other factors that contribute to the phase measurements. In the following sections, we delve into the details of phase-based particle filtering, elaborating on its application in RFID localization. We also discuss the role of a mobile robot in enhancing the acquired data and expanding the capabilities of our system. By focusing on the phase of the received signal and collecting measurements from different locations, we aim to provide an accurate and robust RFID localization system.

2.1.1 Phase model

To understand the value of the phase-based approach, it is important to discuss how phase measurements relate to distance. Essentially, the phase of a signal correlates to the distance the signal has travelled, subject to the frequency of the signal. As the signal moves from the reader to the tag and backwards, it oscillates at a certain frequency. The phase of the signal at any given point can be thought of as the position in the oscillation cycle at that moment. Therefore, by measuring the phase of the signal at the reader, we can estimate the distance the signal has travelled, which provides key information for localization.

In order to model this phase, let us assume that an RFID tag location is denoted as $\mathbf{x}_T \triangleq [x_{\text{tag}} \ y_{\text{tag}} \ z_{\text{tag}}]$ and similarly, reader location as $\mathbf{x}_R \triangleq [x_{\text{reader}} \ y_{\text{reader}} \ z_{\text{reader}}]$. Focusing

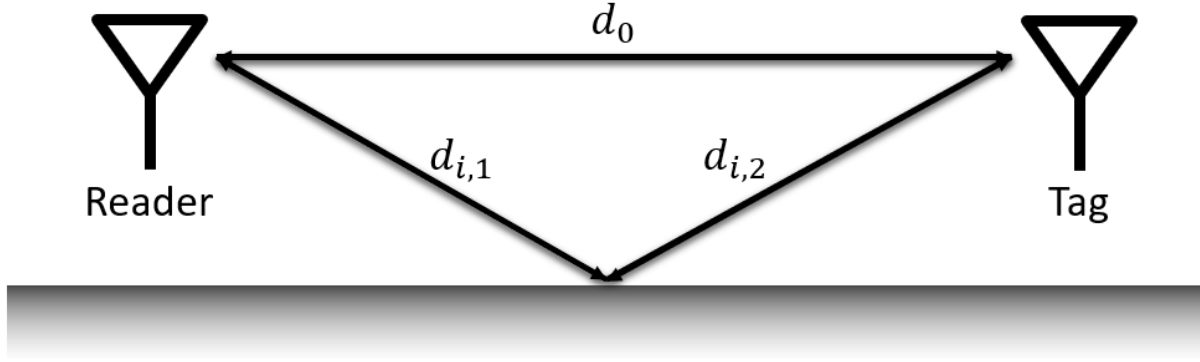


Figure 2.2: Propagation model with a single reflection off the ground.

on the direct path only, reader transmits a signal with carrier frequency f_c and phase ϕ_R , the signal propagates through the environment to be received by the tag with a time delay of $\tau = d_0/c = d_0/(\lambda f_c)$, where $d_0 \triangleq \|\mathbf{x}_R - \mathbf{x}_T\|_2$ is the reader to tag Euclidean distance, c is the speed of light and λ is the carrier's wavelength. For such a delay, the received signal at the tag has a phase of:

$$\phi_R - 2\pi f_c \tau = \phi_R - 2\pi d_0/\lambda = \phi_R - kd_0, \quad (2.1)$$

where $k = 2\pi/\lambda$ is the angular wavenumber. So, the (one-way) flat-fading wireless LoS channel induces a phase of $-kd_0$. In real-world scenarios, beyond the direct Line of Sight (LoS) propagation path, the signal can traverse multiple indirect paths from the receiver to the tag and back through the environment's reflectors. These indirect propagation paths contribute to a phenomenon known as multipath effect. The entirety of the channel can be written as follows:

$$\begin{aligned} h &= \underbrace{a_0 e^{-jk d_0}}_{\text{direct path}} + \underbrace{\sum_{i=1}^{N_m} a_i e^{-jk d_i}}_{\text{multipath}} \\ &= \underbrace{a_0 e^{-jk d_0}}_{h_0} \underbrace{\left(1 + \sum_{i=1}^{N_m} \frac{a_i}{a_0} e^{-jk(d_i - d_0)} \right)}_{h_m} \\ &= h_0 h_m, \end{aligned}$$

where d_i is the length of the i -th propagation path (out of N_m), that depends on the location of the reflectors, as well as the locations of the reader and tag, while complex coefficients a_i , $i \in \{1, \dots, N_m\}$ depend on space geometry, reflector's dielectric constants

and antenna gains. Thus, the induced phase of the roundtrip (two-way propagation channel h^2 (i.e., from reader-to-tag and back) can be written as follows:

$$\phi_{\text{prop}} \equiv \angle h^2 = 2(\angle h_0 + \angle h_m) = -2kd_0 + 2\angle h_m. \quad (2.2)$$

What is measured though is not the compound channel's phase ϕ_{prop} , but there are also several factors that contribute and affect the measured phase ϕ_{out} , such as the tag and its electrical components that induce a term ϕ_{tag} , the location of the reader and tag, delays due to cabling $\hat{\phi}_0$ and phase noise $\hat{\phi}_n$ at the reader's receive chain. So what we would expect as a measurement at the reader can be written as:

$$\begin{aligned} \phi_{\text{out}} &= \phi_{\text{R}} + \phi_{\text{prop}} + \hat{\phi}_0 + \phi_{\text{tag}} + \hat{\phi}_n \\ &= -2kd_0 + \underbrace{\phi_{\text{R}} + \hat{\phi}_0}_{\theta} + \underbrace{2\angle h_m + \phi_{\text{tag}} + \hat{\phi}_n}_{\phi_n} \\ &= -\frac{4\pi d_0}{\lambda} + \theta + \phi_n. \end{aligned} \quad (2.3)$$

Consequently, the received phase can be accurately represented by Eq. (2.3). In this model, the term of primary interest - which correlates to the tag-reader distance d_0 - is accompanied by an unknown constant phase term θ and a variable unknown term ϕ_n .

It is important to note that the readers typically reports a phase value within one of two ranges: either $[-\pi, \pi)$ or $[0, 2\pi)$. In the context of this work, the readers employed adhere to the latter range. Thus, the measured phase is the outcome of applying the modulo operation to ϕ_{out} , specifically:

$$\phi_{\text{meas}} = \phi_{\text{out}} \bmod 2\pi \quad (2.4)$$

$$= \left[-\frac{4\pi d_0}{\lambda} \bmod 2\pi + \theta \bmod 2\pi + \phi_n \bmod 2\pi \right] \bmod 2\pi \quad (2.5)$$

$$= \left[-\frac{4\pi d_0}{\lambda} \bmod 2\pi + \hat{\theta} + \hat{\phi}_n \right] \bmod 2\pi. \quad (2.6)$$

This operation ensures that the measured phase remains within the defined interval, while also introducing an additional level of complexity to the analysis due to the resultant “wrap-around” effect. If we temporarily ignore the noise terms in Eq. (2.6) we get:

¹using the property $(\alpha + \beta) \bmod \gamma = [(\alpha \bmod \gamma) + (\beta \bmod \gamma)] \bmod \gamma$

$$\phi_{\text{meas}} = \left(-\frac{4\pi d_0}{\lambda} \bmod 2\pi \right) \bmod 2\pi \quad (2.7)$$

$$\phi_{\text{meas}} = -\frac{4\pi d_0}{\lambda} \bmod 2\pi \quad (2.8)$$

At this point, it should be mentioned that it is common in the literature to find expressions of the measured phased, as in Eq. (2.3), omitting the minus sign, i.e,

$$\phi_{\text{out}} = +\frac{4\pi d_0}{\lambda} + \theta + \phi_{\text{n}}. \quad (2.9)$$

That is also valid, since the sign of the channel-dependent term $\frac{4\pi d_0}{\lambda}$ informs whether phase is added or subtracted to the phase of the reader, while also providing a more intuitive understanding of the behaviour of the phase, since when the distance increases so does the phase and vice versa. So, the transformation from phase measurement ϕ to distance d_0 , should explicitly state which formula is used, since $\phi_- \neq \phi_+$:

$$\phi_- = \left(-\frac{4\pi d_0}{\lambda} \right) \bmod 2\pi, \quad (2.10)$$

$$\phi_+ = \left(+\frac{4\pi d_0}{\lambda} \right) \bmod 2\pi. \quad (2.11)$$

Solving Eq. (2.8) for distance results in:

$$(2.8) \Rightarrow -\frac{4\pi d_0}{\lambda} = \phi_{\text{meas}} + \kappa 2\pi \quad (2.12)$$

$$\Rightarrow d_0 = \phi_{\text{meas}} \frac{\lambda}{4\pi} + \kappa \frac{2\pi\lambda}{4\pi} \quad (2.13)$$

$$\Rightarrow d_0 = \underbrace{\frac{\phi_{\text{meas}}}{2\pi} \lambda/2}_{\delta\rho} + \kappa\lambda/2 \quad (2.14)$$

$$\Rightarrow d_0 = \delta\rho + \kappa\lambda/2, \quad (2.15)$$

where $\delta\rho = d_0 \bmod \lambda/2$ and $\kappa \in \mathbb{N}$.

Upon examining Eq. (2.15), it becomes evident that when tags are positioned at distances that differ by an integer multiple of $\lambda/2$ away from the reader, the measured phase is the same. This phenomenon is attributed to the periodic nature of the phase and

inherently induces ambiguity to the distance estimation and, consequently, the localization of tags.

Another interesting aspect that led to one of the significant contributions of this study relates to the phenomenon that occurs when the tag’s position results in a phase measurement close to zero (and 2π). A neighboring position - though physically proximate - could potentially result in a phase measurement nearing 2π (and zero respectively).

The crux of this phenomenon lies in the “wrap-around” effect inherent to the phase measurement. When the phase reaches its maximum value of 2π , it resets to zero, creating a discontinuity. As a result, two spatially close positions may correspond to vastly different phase readings near the “wrap-around” point. This unconventional phenomenon, where a small spatial difference leads to a large phase difference is further enhanced when also considering the noise and can complicate the task of RFID localization.

Understanding and appropriately addressing these issues formed a central part of our research, and the strategies we adopted to handle this challenge will be discussed in the subsequent sections.

2.2 Particle Filtering for Phase-Based RFID Localization

2.2.1 Introduction to Particle Filtering

Particle filtering, also known as sequential Monte Carlo sampling, represents a state-of-the-art technique in the realm of probabilistic inference for systems that exhibit nonlinear dynamics or non-Gaussian noise. The technique is rooted in Bayesian filtering, offering a robust framework for estimating the posterior distribution of the system states.

Particle filters, through their sequential nature, permit the online processing of incoming data, making them particularly suitable for real-time applications. They provide an approximation of the desired posterior distribution using a set of particles, each representing a potential state of the system. These particles are then propagated over time, guided by the system’s dynamics and the incoming observations.

One of the distinct advantages of particle filtering is its ability to handle complex, multimodal distributions, which is often a challenge for other filtering techniques. Furthermore, they excel at estimating the state of systems with non-linear relationships between variables or where the noise isn’t Gaussian.

In the context of phase-based RFID localization, these characteristics are particularly beneficial. Given the phase’s periodic nature and the presence of phase ambiguities, the

problem involves dealing with a multimodal distribution - a situation where particle filtering can be leveraged. Furthermore, the inherent non-linearity in the relationship between phase and location, as well as potential non-Gaussian noise in real-world environments, makes particle filtering a fitting choice for tackling this problem.

In the following sections, we will delve into the details of how particle filtering is applied to resolve phase ambiguities and aid in robust distance estimation, thereby enhancing the accuracy of RFID localization.

2.2.2 Phase Based Particle Filtering

Within the sphere of phase-based RFID localization, one of the primary challenges is phase ambiguity. The 'wrap-around' effect means that varying distances between the known antenna locations and the stationary RFID tag can result in identical phase measurements, adding complexity to direct distance estimation.

Our strategy employs particle filtering, a technique well-regarded for handling multimodal distributions. In our application, each particle represents a potential position of the RFID tag within a 3-dimensional space. For a known antenna location, we can use the phase model described in the previous sections to assign a phase value to each particle. The weight of each particle is determined by the difference between the observed phase and the phase dictated by our model for the potential tag position represented by that particle.

A critical advantage of our particle filtering approach is the lack of requirement for continuity in the measurement data. This stands in contrast to a plethora of methods like phase-unwrapping, which demand continuous data and therefore struggle to adapt to real-world scenarios where measurements may be irregular or sporadic.

As measurements from different antenna locations are provided, the particle weights are updated. Through resampling, particles associated with less likely tag positions (those with larger phase discrepancies and, therefore, lower weights) are progressively eliminated. This strategy allows the particle filter to converge on the actual position of the RFID tag, effectively resolving phase ambiguities.

In the subsequent section, we will delve into the specifics of how our particle filtering approach enables robust distance estimation, even in the presence of strong multipath interference.

2.2.3 Robust Distance-based Particle Filtering (RDPF)

In order to illustrate the weighting process for the particle filter, consider Fig. 2.3. Here, we have a phase measurement, denoted as ϕ_{meas} , which is collected at the reader position $\mathbf{x}_R \triangleq [x_R, y_R, z_R]$. Each particle in the filter, representing a potential tag position, is denoted as $\mathbf{x}_T^* \triangleq [x_{\text{tag}}^*, y_{\text{tag}}^*, z_{\text{tag}}^*]$.

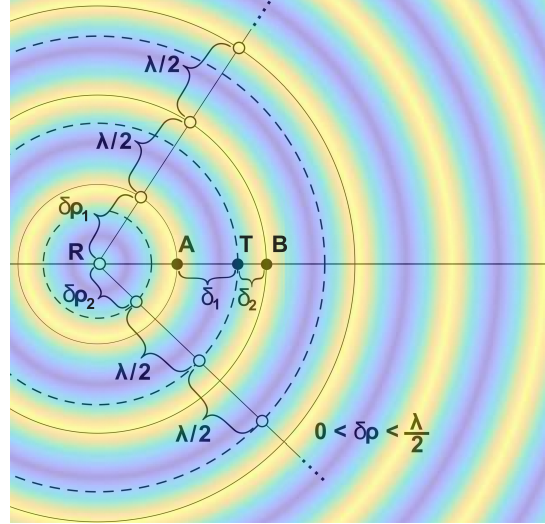


Figure 2.3: Particle weight visualization. The bright yellow concentric circles around the reader position correspond to a high particle weight assignment based on the measured phase.

The weight assigned to each particle is determined by evaluating the conditional likelihood function $p(\cdot|\cdot)$, which essentially quantifies the probability of observing the measured phase given the phase that our model predicts for that specific reader-tag distance:

$$w^* = p(\phi_{\text{meas}}|\phi_{\text{model}}) \quad (2.16)$$

$$\Rightarrow w^* = p(\phi_{\text{meas}}|\mathbf{x}_T^*, \mathbf{x}_R) \quad (2.17)$$

It is evident that knowledge of the conditional likelihood function is required to calculate the weights. Prior art techniques convert the reader-tag distance $d_{RT} = \|\mathbf{x}_R - \mathbf{x}_T\|_2$ to expected (noiseless) phase ϕ_{model}^* using a model like Eq. (2.8) and utilize the phase difference $\delta\phi = |\phi^* - \phi_{\text{meas}}|$ as a metric passing it through a Gaussian Kernel:

$$w^* \propto e^{-\delta\phi^2/(2\sigma_\phi^2)} \quad (2.18)$$

As we have previously discussed, phase discontinuities due to the “wrap-around” effect can lead to a peculiar scenario where spatially close points in a 3-dimensional space correspond to vastly different phase values. This results in a substantial phase difference, $\delta\phi$, which is close to the maximum of 2π , and consequently, a smaller weight is assigned to a particle that is close to the actual location of the tag that we are trying to locate.

A key contribution of this work lies in our method of circumventing this issue. Instead of relying on the phase difference metric, which can be problematic due to phase discontinuities, we propose a novel distance-based metric for determining the particle weights.

To understand this approach, consider Eq. (2.15), which illustrates the relationship between phase and distance. Here, the reader-tag distance can be divided into a “remainder” distance factor, $\delta\rho \in [0, \lambda/2)$, given by:

$$\delta\rho = \begin{cases} \lambda \frac{\phi_{\text{meas}}}{4\pi} & , \text{ for } \phi \text{ defined as } \phi_+, \\ \frac{\lambda}{2} \left(1 - \frac{\phi_{\text{meas}}}{2\pi}\right) & , \text{ for } \phi \text{ defined as } \phi_- \end{cases} \quad (2.19)$$

and an unknown multiple of $\lambda/2$. Under this formulation, the measured phase, ϕ_{meas} , can be translated into a locus of points. In the 2-dimensional case, these points form concentric circles, while in a 3-dimensional case, they form concentric spheres.

These circles or spheres are centered at the reader’s location, \mathbf{x}_R , with radii defined by $r = \delta\rho, \delta\rho + \lambda/2, \delta\rho + \lambda, \dots$. The closest distance between these circles or spheres and the location of the tag \mathbf{x}_T^* defines the utilized metric Δ of this work.

As can be seen in Fig. 2.3, in order to calculate the value of the metric Δ we just need to calculate the distances of the particle’s location to the two closest circles, δ_1 and δ_2 , and keep the smallest distance. Using Eq. (2.15) and Eq. (2.19), the “remainder” distance for the reader-particle locations and the “remainder” distance for the measured phase can be expressed as:

$$d_p = \delta\rho_1 + k\lambda/2 \quad (2.20)$$

$$\Rightarrow \delta\rho_1 = d_p \bmod \lambda/2, \quad (2.21)$$

where d_p is the reader particle distance and:

$$\delta\rho_2 = \lambda \frac{\phi_{\text{meas}}}{4\pi}, \quad (2.22)$$

where both $\delta\rho_1, \delta\rho_2 \in [0, \lambda/2)$. While it is not required to identify which of the two above equations corresponds to phase measurement or reader-particle distance, it is necessary to assign $\delta\rho_1$ the greater value. With the help of Fig. 2.3 and simple calculation it is easy to see that δ_1 and δ_2 can be expressed as:

$$\delta_1 = RT - RA \quad (2.23)$$

$$= (\delta\rho_1 - k_1\lambda/2) - (\delta\rho_2 - k_2\lambda/2) \quad (2.24)$$

$$= \delta\rho_1 - \delta\rho_2 + (k_1 - k_2)\lambda/2, \quad (2.25)$$

$$\delta_2 = RB - RT \quad (2.26)$$

$$= (\delta\rho_2 - k_3\lambda/2) - (\delta\rho_1 - k_4\lambda/2) \quad (2.27)$$

$$= \delta\rho_2 - \delta\rho_1 + (k_3 - k_4)\lambda/2, \quad (2.28)$$

where $k_1, k_2, k_3, k_4 \in \mathbb{N}$. Since $\delta_1, \delta_2, \delta\rho_1, \delta\rho_2 \leq \lambda/2$ and $\delta\rho_1 \geq \delta\rho_2$ we conclude that:

$$\delta_1 = \delta\rho_1 - \delta\rho_2 \quad (2.29)$$

$$\delta_2 = \lambda/2 - (\delta\rho_1 - \delta\rho_2). \quad (2.30)$$

Thus, the metric Δ can be calculated as follows:

$$\Delta = \min(\delta_1, \delta_2) \quad (2.31)$$

$$= \min(\delta\rho_1 - \delta\rho_2, \lambda/2 - (\delta\rho_1 - \delta\rho_2)) \quad (2.32)$$

Notice that for the case of a pair of phases where one is close to 0 (rad) and another close to 2π (rad), the $\delta\rho$'s corresponding to that pair are close to $\lambda/2$ (m) and 0 (m) and thus the above formula will offer a small distance metric Δ .

While the above derivation of the Δ metric provides an intuitive understanding, in practice the steps required reduce the performance of the algorithm. So in practice, a simpler but equivalent expression was devised and used in practice:

$$\Delta = \left| \frac{\lambda}{4} - \left(d_p - \left(\delta\rho - \frac{\lambda}{4} \right) \right) \bmod \frac{\lambda}{2} \right|, \quad (2.33)$$

where $\delta\rho$ is calculated from Eq. (2.19) using the measured phase and d_p is the distance between the known antenna location and the position of the particle.

Another noteworthy contribution of this work is the explicit consideration of the constant phase offset, θ . While previous studies have overlooked this offset, failing to incorporate it into the particle filter parameters or devise any strategies to mitigate its effects, our research actively accounts for this offset. We assign an additional variable, θ^* , to each particle, significantly improving the robustness of our approach.

Although this addition provides a more accurate localization estimate, the addition of an extra dimension in the search space (if the number of particles remains unchanged) can lower the performance of the algorithm.

The modifications required to calculate the particle weights under this new consideration are as follows:

$$\phi^* = (\phi_{\text{meas}} - \theta^*) \bmod 2\pi, \quad (2.34)$$

$$\delta\rho_\phi = \lambda\phi^*/(4\pi), \quad (2.35)$$

$$\delta\rho_d = \|\mathbf{x}_R - \mathbf{x}_T\|_2 \bmod 2\pi, \quad (2.36)$$

$$\delta\rho_1 = \max(\delta\rho_\phi, \delta\rho_d), \quad (2.37)$$

$$\delta\rho_2 = \min(\delta\rho_\phi, \delta\rho_d). \quad (2.38)$$

These values, $\delta\rho_1$ and $\delta\rho_2$, are subsequently fed into Eq. (2.32) to compute the metric Δ . Then, to calculate the weights of the particles, we use the following equation:

$$w^* \propto e^{-\Delta^2/(2\sigma^2)}, \quad (2.39)$$

where σ has units of distance and σ^2 is dependent on the power of the phase measurement noise, encapsulating all sources including multipath. The value of σ essentially determines how strictly the reader-particle distance should correspond to the phase-translated distance based on our model.

In scenarios where the Line of Sight (LoS) is the dominant contributor and the number of available measurements is relatively sparse, we employ smaller values of σ . This facilitates sufficient iterations in the particle distribution to pinpoint the actual tag location. Conversely, in environments characterized by strong multipath and denser measurements, it proves advantageous to tolerate a larger discrepancy between the model and actual distance.

Through extensive experimentation, we found that in low multipath conditions, σ values around 0.1λ yielded the best results. On the contrary, under strong multipath conditions, values around λ proved to be more suitable.

Our methodology aims to provide a localization solution that does not impose any kind of continuity (spatial or temporal) of the measurements to perform, which is often the case in real-world scenarios. Thus, the multiple measurements acquired for each specific tag are considered independent data points and each particle is assigned a number of weights equivalent to the total number of measurements. Each particle is initiated with a weight of 1, which is then dynamically updated for each successive measurement. The updated weight is determined by multiplying the current weight with the newly calculated weight, derived from Eq. (2.39). Subsequently, the weight for each particle is normalized relative to the cumulative weight of all particles.

This allows for a great flexibility in the algorithm since in order to accommodate multiple antennas, the only requirement is the measurements pair (line 11 of the algorithm) $\phi_{\text{meas}}, \mathbf{x}_A$, where \mathbf{x}_A is the position of the antenna, effectively treating the measurements from different antennas simply as unique measurements.

One of the key steps in particle filtering is the resampling of particles. Resampling schemes, such as low-variance resampling, can be applied, with the option to replace particles or not. This stage is crucial in dynamically changing environments where the target is in motion. It provides a more accurate representation of the probable states of a target by emphasizing particles with higher weights (i.e., particles that better explain the observations) and discarding those with lower weights.

In our case, the RFID tags that we aim to locate in our experiments remain stationary. While small performance improvements can be achieved with resampling, our investigations revealed that this process would require extensive fine-tuning of the parameters to yield reliable results. Due to the static nature of our target objects and the added complexity of fine-tuning, we decided to omit the resampling step from the final iterations of our algorithm. The exclusion of this step simplifies our method without significant compromise on the accuracy of our results in the context of locating stationary tags.

The final iteration of our algorithm, titled RDPF1 (Robust Distance-based Particle Filter 1), is summarized as follows: Particles are initialized based on a uniform distribution for each dimension bounded by the search area parameters provided. The dimensionality of the search area is defined by the number of parameters that are to be estimated. In 2D localization, the search space is three-dimensional, whereas in 3D localization, it is four-dimensional due to the addition of the offset parameter θ . If prior information about the position is available, it can be easily incorporated into the initialization process to

fine-tune the distribution of the particles. This flexible framework allows the algorithm to adapt to varying conditions and prior knowledge, making it robust and versatile in a range of applications.

RDPF Algorithm: RDPF1

```

1: Initialization of Variables:
2: Set  $M$  (number of Particles),  $N$  (number of Epochs)
3: Set  $X_{\min}^a, X_{\max}^a, Y_{\min}^a, Y_{\max}^a, Z_{\min}^a, Z_{\max}^a, \theta_{\min}, \theta_{\max}$  (search area dimensions)
4: Set  $T$  (time window of collected phase measurements)
5: for  $n = 1 : N$  do
6:   Initialization of All Particles:  $\forall m = 1 : M$ 
7:      $x^{[m]} \sim \mathcal{U}[X_{\min}^a, X_{\max}^a], y^{[m]} \sim \mathcal{U}[Y_{\min}^a, Y_{\max}^a],$ 
8:      $z^{[m]} \sim \mathcal{U}[Z_{\min}^a, Z_{\max}^a]$ 
9:      $\theta^{[m]} \sim \mathcal{U}[\theta_{\min}^a, \theta_{\max}^a]$ 
10:     $\boldsymbol{\chi}^{[m]} = [x^{[m]} \ y^{[m]} \ z^{[m]} \ \theta^{[m]}]^T$ 
11:    Select  $T$  measurement pairs  $\{\phi_{\text{meas}}^{[t]}, \boldsymbol{x}_R^{[t]}\}$ 
12:    Initialize all particle weights:  $w^{[m]} = 1, \forall m = 1 : M$ 
13:    for  $t = 1 : T$  do { measurement index }
14:      for  $m = 1 : M$  do { particle index }
15:        Set  $\boldsymbol{x}_T^* = [x^{[m]} \ y^{[m]} \ z^{[m]}]^T$  from  $\boldsymbol{\chi}^{[m]}$ 
16:        Set  $\theta^* = \theta^{[m]}$  from  $\boldsymbol{\chi}^{[m]}$ 
17:        Calculate  $\delta\rho_1, \delta\rho_2$  (in m) from Eqs. (2.34)-(2.38)
18:        Calculate  $\Delta$  (in m) from Eq. (2.32)
19:         $w^{[m]} = w^{[m]} p(\Delta | \boldsymbol{\chi}^{[m]}) \equiv w^{[m]} \mathcal{N}(\Delta; 0, \sigma^2)$ 
20:      end for
21:      Weight Normalization:
22:       $w^{[m]} = w^{[m]} / \sum_{m=1}^M w^{[m]}, \forall m = 1 : M$ 
23:      % Optional: Low Variance Particle Resampling
24:    end for
25:     $\hat{\boldsymbol{x}}_T^{[n]} = \sum_{m=1}^M w^{[m]} \boldsymbol{\chi}^{[m]} = [\hat{x}_{\text{tag}}^{[n]} \ \hat{y}_{\text{tag}}^{[n]} \ \hat{z}_{\text{tag}}^{[n]} \ \hat{\theta}^{[n]}]^T$ 
26: end for

```

Modifications for Accelerated Execution: RDPF2

To accelerate execution time while keeping the offset θ as an unknown, the algorithm described above can be further refined. In the modified algorithm, each particle represents only the tag coordinates, excluding θ . Meanwhile, an external loop (line 5) can be used to iterate through a predefined set of potential θ values, each of which is applied globally across all particles. This approach effectively reduces the search space for a given number of particles, M . Alternatively, this means that a smaller number of particles can be utilized to adequately probe the modified search space. In order to obtain the final estimate of the tag position, a mean is calculated over the estimated positions for all the θ values tested. The benefit is a significant reduction in computational overhead without sacrificing the robustness of the solution.

In this alternative version, titled RDPF2, the following simple modifications are required:

- Line 9 is omitted and the initialization is modified to use a set of values for θ with a resolution of $\delta\theta = (\theta_{\max} - \theta_{\min})/N$, where N is the number of repetitions to perform.
- Line 10: $\boldsymbol{\chi}^{[m]} = [x^{[m]} \ y^{[m]} \ z^{[m]}]^T$
- Line 16: Set $\theta^* = \theta_{\min} + (n - 1)\delta\theta$
- Line 25: $\hat{\boldsymbol{x}}_{\text{T}}^{[n]} = \sum_{m=1}^M w^{[m]} \boldsymbol{\chi}^{[m]} = [\hat{x}_{\text{tag}}^{[n]} \ \hat{y}_{\text{tag}}^{[n]} \ \hat{z}_{\text{tag}}^{[n]}]^T$
- Finally line 27 was added to report the final location estimate:

$$\hat{\boldsymbol{x}}_{\text{T}} = \frac{1}{N} \sum_{n=1}^N \hat{\boldsymbol{x}}_{\text{T}}^{[n]} = [\hat{x}_{\text{tag}}^{[n]} \ \hat{y}_{\text{tag}}^{[n]} \ \hat{z}_{\text{tag}}^{[n]}]^T$$

Experimental results have demonstrated that RDPF2 operates an order of magnitude faster than RDPF1, while maintaining similar performance levels. Furthermore, it was found through experimentation that in environments with light multipath interference, the estimated tag location changes almost continuously across different values of θ . This behavior is contrasted in environments with rich multipath interference. Consequently, the behavior of RDPF2 could potentially be used as a classifier to evaluate the degree of multipath richness in an environment.

Additionally, by selecting a single random value θ , the modified algorithm can generate satisfactory results in a significantly shorter span of time. This finding presents opportunities for quick, efficient, and relatively accurate localization in scenarios where time is of the essence or computational resources are limited.

Calibration Process

In addition to these modifications, another key aspect of this work is the implementation of a calibration process that efficiently manages the phase offset disparities across an array of antennas and reader chains. This process, used in conjunction with data preprocessing, effectively reduces the discrepancies caused by these phase offset differences.

This calibration process begins by positioning a tag at a fixed location, with an antenna mount firmly secured at an arbitrary distance, typically around 1 meter, facing the tag. Each antenna, along with its associated cabling used in the experiments, is then connected to its corresponding receiver chain.

Each antenna, in turn, is placed on the mount, and measurements are gathered for that specific chain for a duration of ten seconds. Once the measurements for one antenna are collected, the next antenna is placed on the mount, and the process is replicated for all antennas in use. This procedure is designed to maintain an identical topology and environment for the reader-tag channel across all antennas, effectively isolating the constant phase offset differences.

Once the data are collected, a “wrap-around” phase mean is calculated for each antenna. In scenarios where measurements are recorded close to both boundary values of the interval $[0, 2\pi)$, indicating a phase “wrap-around”, a traditional mean calculation would result in skewed results. To circumvent this, in such cases the interval is divided into two halves, $[0, \pi)$ and $[\pi, 2\pi)$, and 2π is added to the measurements belonging to the lower half. The traditional mean is then calculated; if its value surpasses the $[0, 2\pi)$ interval, a $\text{mod } 2\pi$ operation is applied to it, resulting in the final “wrap-around” mean.

The ten-second duration and the mean operation are utilized to ensure optimal averaging out of the variable phase noise terms. After this, the constant phase offset for each antenna is calculated relative to the first antenna, and it is corrected during the data preprocessing phase using the following equation:

$$\phi_{\text{corr}}^{[i]} = \left(\phi_{\text{meas}}^{[i]} - \phi_{\text{offset}}^{[i]} \right) \text{mod} 2\pi, \quad (2.40)$$

where, i serves as an indicator for the i -th antenna. This detailed calibration process further increases the accuracy and reliability of our localization process.



Figure 2.4: Our robotic platform

2.2.4 Experimental Results and Analysis

We conducted four indoor experimental campaigns using an Impinj Speedway R420 RFID reader. To effectively control the reader’s parameters, we developed software utilizing Impinj’s LTK API. Our setup involved an MTI MT-242032 7 dBiC reader antenna and up to three FlexiRay SF-2110 5 dBi antennas. The reader’s transmission (Tx) power was configured within the range of 20 dBm to 30 dBm.¹ Across all campaigns, we observed that an increase in the reader’s Tx power correspondingly increased the number of tag measurements.

During the first campaign (Fig. 2.5), the tag was successfully interrogated at 56 and 20 positions, at Tx powers of 30 and 20 dBm, respectively. In the second and third campaigns (Fig. 2.7), each tag was interrogated approximately 900 times at 30 dBm and about 400 times at 20 dBm. In the fourth and final campaign, each tag was interrogated about 300 times at 30 dBm and approximately 100 times at 20 dBm. However, at these respective Tx powers, 4 and 51 tags could not be interrogated. Due to the low success

¹Cable losses, as well as the reader’s output power, were measured using a Vector Network Analyzer (VNA) and a spectrum analyzer, respectively.

rate of unique tags being interrogated at 20 dBm, measurements at this power level were not included in this campaign.

For the purpose of comparison, we also implemented two state-of-the-art RFID phase-based localization methods: BackPos [43] and Relock [21]. The performance metrics used were the Mean Absolute Localization Error (MAE) $E[|e|]$ and the Root Mean Squared Localization Error (RMSE) $\sqrt{E[|e|^2]}$. Here, $e \triangleq \|\hat{\mathbf{x}}_T - \mathbf{x}_T\|_2$ represents the estimation error metric.

Campaign 1 - Light Multipath

During the first experimental campaign (Fig. 2.5), an Impinj Speedway R420 RFID reader equipped with a single MTI MT-242032 antenna was used. This antenna was connected to the reader via a 0.9 dB loss coaxial cable, and an Alien ALN-9540 (Higgs-2) RFID tag was placed in a fixed position within an unobstructed indoor setting. The experiment involved manually moving the antenna along a three-meter-long line in increments of five centimeters. The tag was placed on the bisector of the antenna's trajectory at a distance of one meter away. Both the antenna and the tag were placed at a height of 1.52 meters to reduce multipath interference.



Figure 2.5: Campaign I

Once the setup was established, we carried out tag interrogation measurements at every antenna position for four seconds per transmission power level. Upon the completion of the measurement acquisition process, we calculated a “wrap-around” mean phase for every position and power level. This modified mean was utilized once again (as described in Section 2.2.3) to average out the phase noise and deal with the discontinuities caused by the phase fluctuations near the interval boundaries.

The results of the first campaign are shown in Fig.2.6. All methods tested produced satisfactory results, achieving a mean absolute error (MAE) below 2 cm at higher transmission power. In relative terms, this absolute error represents less than 2% of the one-meter tag-to-reader range set for this campaign. However, a distinct trend was observed: ReLock’s performance appeared to improve with an increase in the number of measurements, while both RDPF1 and RDPF2 showed consistent performance irrespective of the measurement count. Meanwhile, BackPos demonstrated notable sensitivity to the availability of measurements, and its error margin appeared to increase with greater transmission power, possibly due to amplified multipath interference.

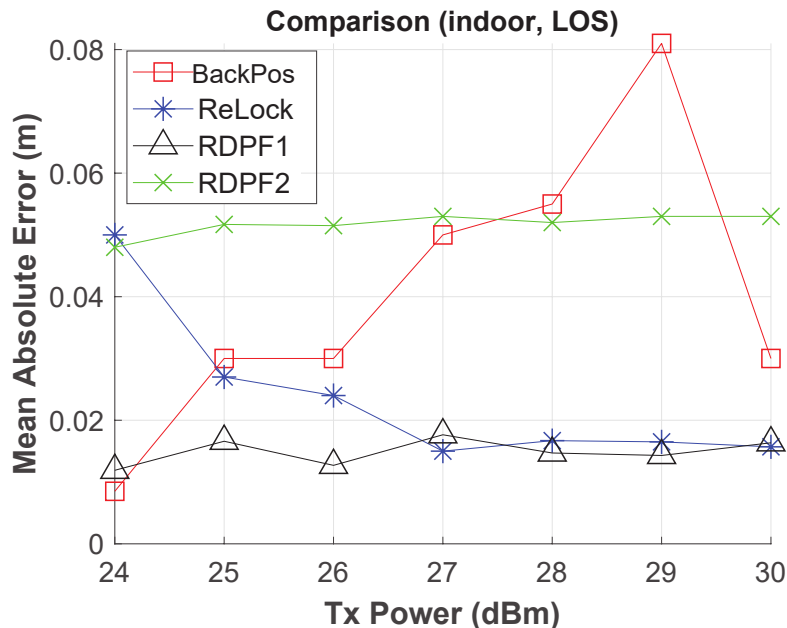


Figure 2.6: Campaign I: localization error vs Tx power

Regarding the implementation of RDPF methods, we set a search area of $1\text{m} \times 1\text{m}$ for particle initialization. The particle count was set at $M = 10^5$ for RDPF1 and $M = 10^4$ for RDPF2, the latter requiring fewer particles due to its distinct approach of employing a common θ across all particles instead of individual randomization. It is worth noting that, given the height of the tag and the reader antenna, the tag localization problem has

two unknown parameters to estimate, $[x_{\text{tag}}, y_{\text{tag}}]$, allowing for a comparison with BackPos, which is a 2D tag localization method by design. Due to the relatively low number of measurement locations, all execution times remained well below one second.

Campaign 2 - Rich Multipath

The second campaign replicated the manual reader movement setup of the first experiment, but with alterations to introduce a multipath-rich environment. Two scenarios were set up: Scenario A) involved placing 15 tags on books, neatly placed on a bookshelf, each approximately 5.5 cm apart, and Scenario B) had tags only on the two books at opposite ends of the bookshelf (see right part of Fig. 2.7). The same reader, antenna, and cables from the previous campaign were used and measurements were taken every 5 cm as before.

The aim of this campaign was to stress test the algorithms in an environment laden with additional reflections and multipath effects among the tags. Scenario A, in particular, was designed to challenge the operational limits of the tags due to the close proximity that causes coupling. Alien ALN-9740 (Higgs-4) tags were used in this campaign. The results for Scenario A are presented in Table 2.1.

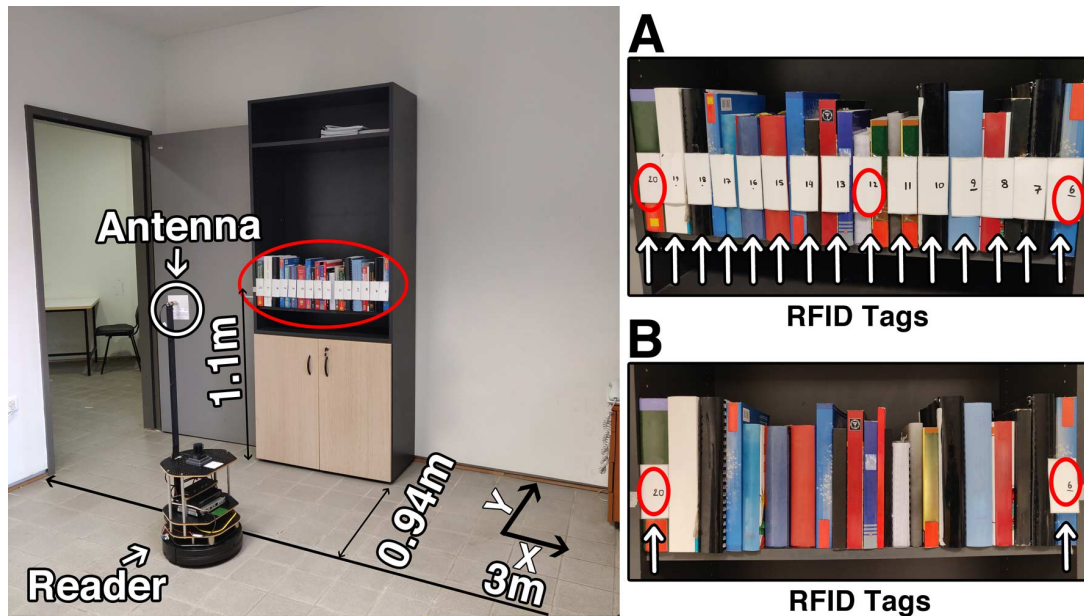


Figure 2.7: Campaigns II & III: Robotic platform and bookshelf tag placement for cases A (top-right) and B (bottom-right).

Despite the clustering of tags, the performance of the algorithms did not appear to be significantly affected, rendering the results of Scenario B unnecessary. Notably, BackPos

produced excessive errors in some instances, likely due to stronger multipath effects, and was subsequently excluded from future campaigns.

In both the second and third campaigns, the RDPF1 and RDPF2 methods consistently outperformed ReLock and BackPos at the lower transmission power of 20 dBm. Given that the number of measurements was dictated by the transmission power, it can be deduced that RDPF1 and RDPF2 provide robust estimates when the measurement quantities fluctuate. Table 2.1 illustrates the absolute error \mathbf{e} , and $\mathbf{e}_x \triangleq |\hat{x}_{\text{tag}} - x_{\text{tag}}|$, which represents the error along the x axis, parallel to the bookshelf, for three different tags. The minimum error value for each scenario among the compared methods is highlighted in bold.

Campaign 3 - Rich Multipath with a Robot

In the third campaign (Fig. 2.7), a custom robotic setup was employed using a Turtlebot2 equipped with a Kobuki mobile base for movement and a Hokuyo UST-20LX LIDAR sensor for Simultaneous Localization and Mapping (SLAM) operations. The antenna and cables were replaced with more compact counterparts; a 0.74 dB loss coaxial cable and a FlexiRay SF-2110 5 dBi antenna. The height of the antenna and tags was also reduced to 1.1 m, further intensifying the multipath effects.

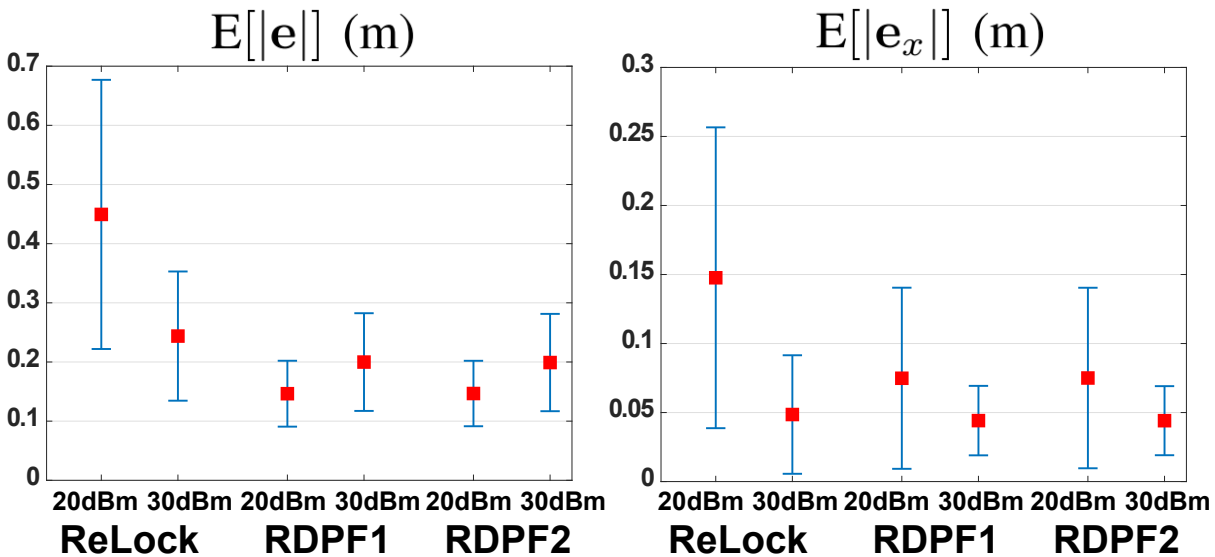


Figure 2.8: Campaign III (moving robot) average absolute error between 2 standard deviations across all 15 bookshelf tags.

The robot's position was accurately estimated using Google's Cartographer [44] for mapping the environment and the Adaptive Monte Carlo Localization (AMCL) [45, 46] during experiments. The robot moved at a steady speed of 10 cm/sec, with measurements

taken continuously at an average interval of 0.5 cm. The results of this campaign are presented in Table 2.1 and Fig. 2.8.

The RDPF methods maintained the same search area and particle numbers as in the previous campaigns. The execution time for RDPF1, in the worst-case scenario (i.e., the largest number of measurements), was 2.5 sec per repetition per RFID tag, while RDPF2 required 0.25 sec per value of θ per tag. For ReLock, a pre-filtering algorithm was implemented to identify the largest window of consecutive measurements, ensuring that every measurement location is within 5 cm of the next. This was necessary, as ReLock requires that the phase between two consecutive measurements does not change drastically, so phase unwrapping can work reliably. ReLock’s execution time per tag at the same processing unit for the largest number of measurements was 0.25 seconds. Given that the robot moves at a rate of 10 cm/sec, covering a trajectory of 3 meters required 30 sec. Thus, all the methods were considered “real-time” for the given scenarios.

Table 2.1: Experimental results of the bookshelf campaigns with all 15 tags placed for Campaigns III & IV (case A).

			Tag ID					
			#20 leftmost tag		#12 center tag		#6 rightmost tag	
			$E[e]$ (m)	$E[e_x]$ (m)	$E[e]$ (m)	$E[e_x]$ (m)	$E[e]$ (m)	$E[e_x]$ (m)
Campaign 2 - Manual	ReLock	20dBm	0.225	0.033	0.755	0.104	0.112	0.013
		30dBm	0.016	0.012	0.032	0.025	0.048	0.012
	RDPF1	20dBm	0.063	0.006	0.102	0.036	0.029	0.013
		30dBm	0.103	0.012	0.087	0.017	0.018	0.014
	RDPF2	20dBm	0.067	0.006	0.109	0.036	0.050	0.013
		30dBm	0.106	0.012	0.079	0.018	0.051	0.013
	BackPos	20dBm	0.223	0.043	0.361	0.041	0.194	0.001
		30dBm	0.186	0.165	0.091	0.075	0.294	0.293
Campaign 3 - Robot	ReLock	20dBm	0.630	0.211	0.411	0.066	0.621	0.197
		30dBm	0.363	0.090	0.172	0.036	0.251	0.058
	RDPF1	20dBm	0.182	0.099	0.132	0.021	0.104	0.008
		30dBm	0.254	0.068	0.158	0.046	0.138	0.051
	RDPF2	20dBm	0.181	0.099	0.132	0.021	0.102	0.009
		30dBm	0.251	0.067	0.158	0.046	0.137	0.051

Fig. 2.8 illustrates the third campaign’s average value of e and e_x (red squares) across all 15 tags, within two standard deviations (the vertical lines span 2 standard deviations).

At 30 dBm, the methods performed adequately with error e_x below 5 cm, which corresponds to relative (to tag-reader distance) error below 5%; however, the RDPF methods presented smaller variance, with a standard deviation of the order of 2 cm at 30 dBm Tx power. For 20 dBm Tx power, RDPF1 and RDPF2 outperform Relock, probably due to the sensitivity of the latter to the available number of measurements.

Campaign 4 - Rich Multipath 3D

The fourth and final campaign reemployed the robotic setup in a distinct, multipath-rich environment. This time the objective was to assess the algorithms' effectiveness across varied environments and their capability to execute 3D localization.

There were 70 tags in this campaign, attached to either the backs or to the insides of books. These books, which had different orientations relative to the robot-antenna's movement, were positioned on metallic shelves, thereby enhancing reflections. The books were set at various heights, ranging from 0.15 to 2.3 m. The overall topology can be observed in Fig.2.9. The actual trajectory of the robot, as computed by Cartographer, is presented in Fig.2.10.



Figure 2.9: Campaign IV: Library topology.

In terms of the robotic platform, a longer pole was attached to accommodate more antennas at greater heights. The number of FlexiRay SF-2110 antennas was increased to three, located at heights of 1.06, 1.46, and 1.86 m. This setup expanded the area within which tags could be effectively interrogated and resolved the localization ambiguity on

the vertical z -axis. For this campaign, the search space was broadened to a $2.5 \text{ m} \times 1 \text{ m} \times 2.5 \text{ m}$ space, while the number of particles remained at 10^5 .

Table 2.2: 3D Experimental Results Across 70 Tags for different number of available measurements per tag.

	$E[e]$ (m)	$\sqrt{E[e ^2]}$ (m)
Measurements per tag > 50	0.31	0.38
Measurements per tag > 100	0.29	0.36
Measurements per tag > 200	0.24	0.26

To the best of our knowledge, ReLock does not utilize multiple antennas simultaneously, so it was excluded from this campaign. The results of the campaign, which can be found in Table 2.2, demonstrate that RDPF1 can accurately locate the tags in 3D space. This accuracy increases with the number of available measurements. Specifically, in cases where the number of measurements exceeds 200 (with an average number of measurements being 300), our method locates the tags with a Mean Absolute Error (MAE) of 24 cm. This error equates to 9.6% of the maximum search space dimension (i.e., 2.5 m in this case). The longest execution time for RDPF1 in the 3D scenario was 5 seconds, a result of the increased number of measurements.



Figure 2.10: Campaign IV: Real map of the library produced by the Cartographer algorithm, including the robot's estimated trajectory and the actual location of the tags.

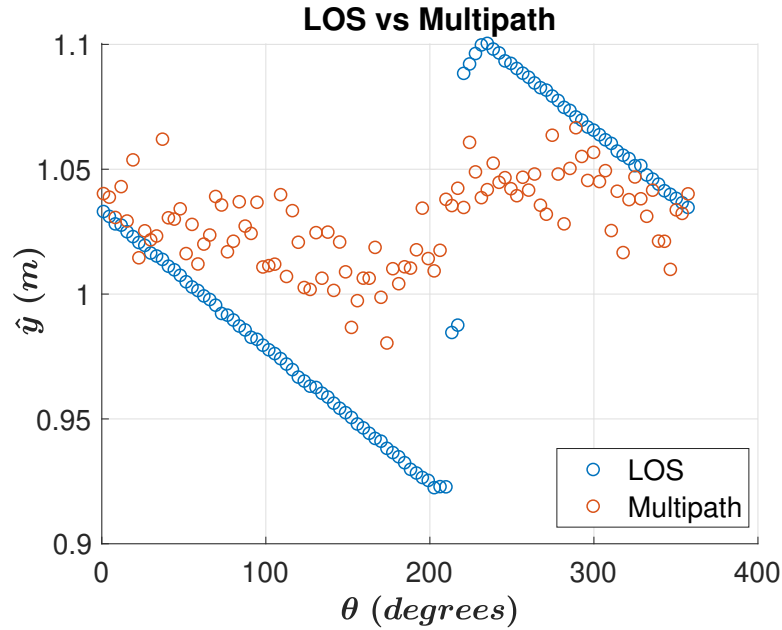


Figure 2.11: Visualization of \hat{y}_{tag} with respect to θ for two different environments: LoS/light multipath (campaign I) vs strong multipath (campaign III). This behavior could be exploited for classification of the environment as multipath-rich or not.

2.3 Conclusion

Our proposed phase-based localization technique has demonstrated robust performance amidst the challenges presented by complex and multipath-rich environments. The method has proven to be resilient even in situations where the number of phase measurements from the RFID tags is inconsistent and sporadic. Uniquely, this method can smoothly adapt to varying numbers of reader antennas and efficiently capitalizes on the mobility of the reader, as well as the autonomous self-localization ability of robot-readers.

In settings such as a library, the method has shown a remarkable capability to achieve decimeter-level localization accuracy for 3D RFID tag localization. This level of precision has been achieved without the need for excessive bandwidth usage or the presence of any reference tags. The results and the testing environment effectively mimic realistic settings where such technologies might be deployed, enhancing the applicability and real-world relevance of our findings.

Moreover, our research has unveiled a potentially invaluable classification method. This method can assist in characterizing an environment based on its multipath characteristics, enabling a more tailored and efficient deployment of localization methods. By determining whether an environment is multipath-rich or not, systems can be adjusted and optimized accordingly to achieve the best performance.

During the design and execution of these algorithms, special attention was paid to execution speed. The aim was to match the algorithm's processing time with the operational speed of the robot, ensuring real-time operation. This consideration is particularly crucial in applications where swift and real-time localization is necessary, making our method a promising solution for a variety of real-world scenarios.

Chapter 3

Reflection and Tag Joint Localization

3.1 Introduction

Radio frequency identification (RFID) technology has shown promise in various applications, including logistics, healthcare, and smart cities, among others. While the preceding chapter of this dissertation has explored various factors of RFID-based localization, yet one issue remains conspicuously underexamined: the complex interference caused by reflections from nearby objects, often termed as "multipath effects."

Reflections from walls, furniture, and other objects in the environment can introduce complexities that are often overlooked in conventional localization schemes. These reflections do not merely act as noise; they can significantly distort the electromagnetic field in a nonconcise way and, consequently, the phase and received signal strength indicators (RSSIs) used in localization algorithms. If not carefully taken into account, it can lead to compromised system accuracy that can be misleading and unreliable, particularly in cluttered or dynamically changing environments.

The presence of these reflections introduces a multifaceted challenge. First, the sheer number of variables introduced by reflections complicates the mathematical modeling of signal propagation, making conventional algorithms less effective. Second, reflections can create "ghost" locations—spurious positions that appear valid to localization algorithms but do not correspond to the actual position of the RFID tags. Finally, the unpredictable nature of these reflections, influenced by various factors such as the material of reflecting surfaces and their relative position to both the RFID tags and readers, adds an additional layer of complexity to the problem.

Ignoring this nuanced issue has real-world implications. Whether it is the inaccurate localization of assets in an industrial setting or the risk of misidentification in tracking systems, the consequences can be both a deterring factor for the use of RFID based systems. As RFID technologies find applications in increasingly intricate environments, understanding and mitigating the impact of reflections becomes a pressing, real-world challenge.

In light of these challenges, this chapter aims to examine the specific issue of reflections in RFID-based localization. We will delve into an innovative approach that provides a method for the joint estimation of both RFID tags and reflectors' locations. By doing so, this methodology offers a robust solution that significantly mitigates the adverse impact of reflections on localization accuracy. Furthermore, we will examine the theoretical underpinnings of this approach, discuss its implementation nuances, and explore its potential applications in real-world scenarios ¹.

Through this focused exploration, our aim is to contribute to a more nuanced understanding of the challenges and solutions surrounding reflections in RFID localization and provide practical, reliable applications in increasingly complex real-world settings, while also paving the way for future research in this often overlooked yet crucial aspect of RFID-based localization.

3.2 Reflection and Measurement Modeling

Again in this study, we consider a monostatic RFID reader configured with M distinct carrier frequencies, specified by an index $m \in \{0, 1, \dots, M - 1\}$. The reader is mobile, potentially integrated within a robotic platform, thereby allowing it to gather N measurements at distinct locations. These locations are numerically indexed by $n \in \{0, 1, \dots, N - 1\}$. The spatial coordinates of the reader during the n -th measurement are denoted as $\mathbf{x}_T^{(n)} = [x_T^{(n)} \ y_T^{(n)}]^\top$, while the coordinates of the RFID tag in question are represented as $\mathbf{x} = [x_{\text{tag}} \ y_{\text{tag}}]^\top$.

For the purpose of modeling large-scale path loss, we introduce the following equation:

$$L_X = \left(\frac{\lambda_m}{4\pi d_0^X} \right)^2 \left(\frac{d_0^X}{d_X} \right)^{u_X}, \quad (3.1)$$

¹In the development of this methodology, substantial insights were derived in the extended work of Spyridon Peppas in their diploma work [47].

where d_0^X is denotes reference distance, and d_X the distance specific to link X. The types of links considered in this setup include point-to-reader (PT), point-to-wall (PW), wall-to-reader (WT), and reader-to-virtual point (TV). These links are relevant when the reader is located at a position designated T, a point of interest is at P, and its virtual image with respect to a given reflector or wall is at V. The variable λ_m denotes the carrier wavelength corresponding to the m -th frequency, and u_X is the path-loss exponent.

When the path-loss exponent $u_X = 2$, the large-scale path loss model simplifies to:

$$L_X = \left(\frac{\lambda_m}{4\pi d_0^X} \right)^2 \left(\frac{d_0^X}{d_X} \right)^2 = \left(\frac{\lambda_m}{4\pi d_X} \right)^2. \quad (3.2)$$

3.2.1 Modeling 1st and 2nd Order Reflections

As already mentioned, the signal reflections from the environment can cause significant variations in the expected phase and RSSI measurements. Modeling the behavior of line-of-sight (LoS) as well as the effect of reflected multipath signals is crucial for achieving reliable and accurate localization. The focus of this subsection is to provide an extensive model that accounts for both 1st and 2nd order reflections along with LoS signals. The geometrical considerations can be found in Figure 3.1.

Modeling of Line-of-Sight (LoS) Signal

We commence by describing the model for the LoS signal. Here, we consider an RFID tag located at a specific point P (as illustrated in Fig. 3.1). The mathematical expression that represents the LoS signal received from the tag at the reader location n and carrier frequency m is:

$$x_0[m, n] = \sqrt{2P_c \eta L_{\text{PT}, \text{PT}}} \exp \left(-j2\pi \frac{d_{\text{PT}}^{(n)} + d_{\text{PT}}^{(n)}}{\lambda_m} \right) \quad (3.3)$$

$$= \underbrace{\sqrt{2P_c \eta L_{\text{PT}}}}_{\mu_0} \exp \left(-j4\pi \frac{d_0^{(n)}}{\lambda_m} \right). \quad (3.4)$$

Here, P_c refers to the carrier transmission power at passband, and η stands for the backscattering efficiency of the tag. $d_0^{(n)}$ is the direct path distance between the RFID reader and the tag for the n -th measurement. Importantly, Eq. (3.4) incorporates the

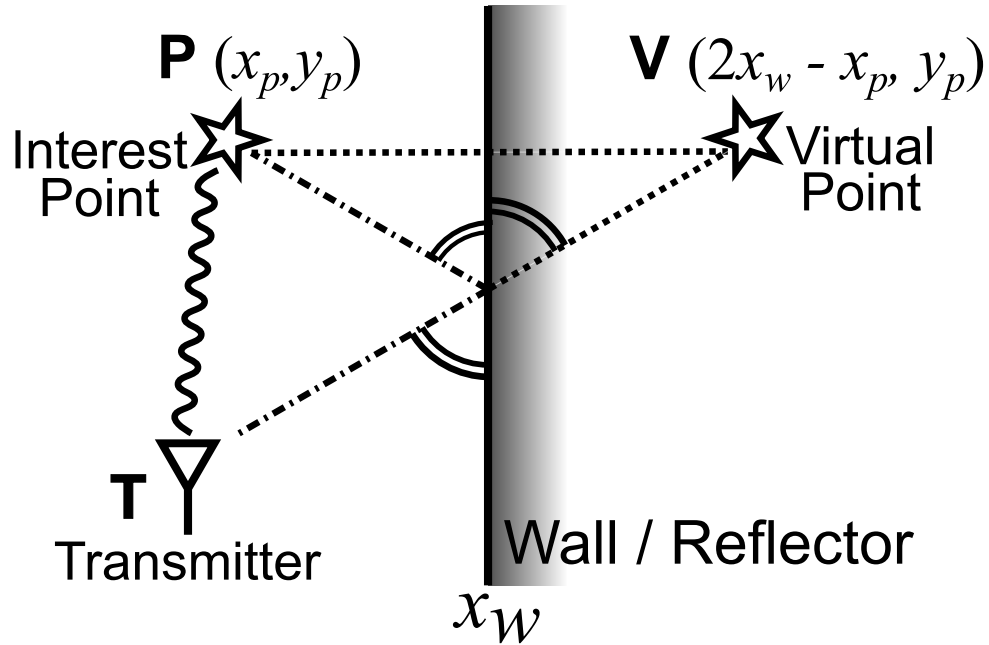


Figure 3.1: Reflections with a wall. T is the transmitter, P is a grid point and V is the image point of P

notion of a round-trip path—meaning the signal travels from the reader to the point of interest and then returns.

Exploration of First and Second Order Reflections/Multipath

Alongside the LoS propagation, this study also delves into the impacts of first and second-order reflections, also known as multipath effects. These effects are critical in environments where there are multiple reflective surfaces such as walls or metallic objects.

- **1st Order Multipath:** In this case, the signal path from the reader to the point of interest (tag) differs from the return path to the reader.
- **2nd Order Multipath:** Here, the signal that travels on the round-trip path is reflected twice, typically against a wall or some other reflector.

These reflections create interference patterns that can either amplify or diminish the resultant signal at the reader and change the measured phase, thereby affecting the accuracy of localization methods.

Understanding these first and second-order reflections is pivotal for the design and optimization of RFID systems, especially in complex environments with numerous reflective surfaces. It helps improve the robustness of the system against localization errors due to multipath phenomena.

It is worth mentioning that while higher-order multipath effects do exist, they are generally considered negligible for practical applications. The rationale behind this is the exponentially diminishing power of these higher-order reflections. Each successive reflection causes the signal to lose energy, rendering the effects of higher orders increasingly trivial compared to the 1st and 2nd order effects. Therefore, this study mainly focuses on understanding and modeling the 1st and 2nd order multipath phenomena, as they are the most impactful in terms of both power and potential to cause localization errors.

First Order Reflection

The inclusion of first order reflections can significantly improve the accuracy of the received signal model. Illustrated in Fig. 3.1, these reflections emerge when the RFID reader captures signals that have encountered a single reflective surface before arriving at the reader. The reflective surface can often be a wall, partition, or any other object with reflective properties.

The expression for the reflected signal component received at the reader's n -th location, on the m -th carrier frequency, can be described by the following mathematical model²:

$$x_1[m, n] = \sqrt{\gamma_w 2P_c \eta L_{PT} L_{TV}} \exp\left(-j2\pi \frac{d_{PT}^{(n)} + d_{PW}^{(n)} + d_{WT}^{(n)}}{\lambda_m}\right) \quad (3.5)$$

$$= \underbrace{\sqrt{\gamma_w 2P_c \eta L_{PT} L_{TV}}}_{\mu_1} \exp\left(-j2\pi \frac{d_0^{(n)} + d_r^{(n)}}{\lambda_m}\right). \quad (3.6)$$

Here, $\gamma_w \in (0, 1)$ represents the reflection coefficient, specifying the fraction of the incident signal that is reflected upon striking the wall. The direct Point-to-Tag distance is denoted by $d_0 \equiv d_{PT}$. The parameter $d_r^{(n)}$ represents the distance of the indirect/reflected path, calculated based on image theory and the concept of a virtual point (or image point) generated by the reflection.

Assuming a reflector or wall located at a position $x = x_w$, parallel to the y -axis (Fig. 3.1), the reflected path's distance $d_r^{(n)}$ is equal to the distance between its virtual or image point and the reader at its n -th location:

²The term L_{TV} is evaluated according to Eq. (3.2) where $d_{TV} = d_{TW} + d_{WV} = d_{TW} + d_{WP} \triangleq d_r$. This follows the assumption of specular reflection, which is aligned with ray-based geometry models, for example, the two-ray model. Alternative scattering models that employ $L_{TV} = L_{TW} \times L_{WV}$ were also examined but yielded significantly attenuated reflections. It is critical to have sufficiently "large" reflected power for the algorithm to function effectively, as will be elaborated further.

$$d_r^{(n)} = \sqrt{(2x_w - x_{\text{tag}} - x_T^{(n)})^2 + (y_{\text{tag}} - y_T^{(n)})^2}. \quad (3.7)$$

Second Order Reflection

Similarly, the second-order reflection can play a crucial role in complex environments with multiple reflective surfaces and certain geometric conditions. This is modeled as follows:

$$x_2[m, n] = \sqrt{\gamma_w \gamma_w 2P_c \eta L_{\text{TV}} L_{\text{TV}}} \exp\left(-j2\pi \frac{d_{\text{PW}}^{(n)} + d_{\text{WT}}^{(n)} + d_{\text{PW}}^{(n)} + d_{\text{WT}}^{(n)}}{\lambda_m}\right) \quad (3.8)$$

$$= \underbrace{\gamma_w \sqrt{2P_c \eta L_{\text{TV}}}}_{\mu_2} \exp\left(-j4\pi \frac{d_r^{(n)}}{\lambda_m}\right) \quad (3.9)$$

Here, γ_w is the reflection coefficient for the wall, assumed to be the same for both reflections. The product $\gamma_w \gamma_w$ indicates that the signal undergoes two reflections. L_{TV} denotes the path loss between the Transmitter and the Virtual point of reflection. The exponential term accounts for the phase shift experienced due to the traveled distance. Notably, $d_r^{(n)}$ is the one way distance of the reflection path.

Compound Signal Model

In a practical setup, the received signal $y[m, n]$ is a combination of various components: the LoS signal $x_0[m, n]$, multipath signals $x_i[m, n]$, and noise $w[m, n]$:

In the general case, the compound received signal with all the possible multipath effects can be modeled as the superposition of the individual signals as follows:

$$y[m, n] = \underbrace{x_0[m, n]}_{\text{LoS}} + \underbrace{\sum_{i=1}^{\infty} x_i[m, n]}_{\text{multipath}} + \underbrace{w[m, n]}_{\text{white noise}}. \quad (3.10)$$

Here, the noise $w[m, n] \sim \mathcal{CN}(0, \sigma^2)$ is assumed to be white, circularly symmetric complex Gaussian noise with zero mean and variance σ^2 .

Due to computational and practical considerations, such as signal attenuation, we limit our focus to first and second-order reflections. Hence, from Eq. (3.10) the simplified model becomes:

$$y[m, n] = \underbrace{x_0[m, n]}_{\text{LoS}} + \underbrace{x_1[m, n]}_{\text{1st order}} + \underbrace{x_2[m, n]}_{\text{2nd order}} + \underbrace{\mathcal{CN}(0, \sigma^2)}_{\text{white noise}}. \quad (3.11)$$

Signal-to-noise-ratio is calculated considering the reflected signals as useful signals as is defined as:

$$\text{SNR} = \frac{\mathbb{E} \left[|x_0[m, n] + x_1[m, n] + x_2[m, n]|^2 \right]}{\sigma^2}, \quad (3.12)$$

where $\mathbb{E}[\cdot]$ denotes the expected value.

3.2.2 Adopted Signal Model

LoS Formulation

The region of interest is divided into a regular square grid of $N_x \times N_y$ points with d_x, d_y resolution, representing the number of points in x and y -axis, respectively. Let σ_p be the complex reflectivity of the p -th spatial grid point of interest (or equivalently the p -th target), where $p = 0, 1, \dots, N_x N_y - 1$. Note that the absence of a target at a particular grid point is simply represented by a zero value for the corresponding target reflectivity:

$$\sigma_p = \begin{cases} 0, & \text{absence of a target} \\ a, & \text{presence of a target } \{a \in \mathbb{C} \mid a \neq 0\}. \end{cases} \quad (3.13)$$

For monostatic reader operation the target response can be expressed as follows:

$$y[m, n] = \sum_{p=0}^{N_x N_y - 1} \sigma_p \exp(-j2\pi f_m \tau_{p,n}), \quad (3.14)$$

Here $\tau_{p,n}$ denotes the round-trip propagation delay between the p -th target/point of interest and reader antenna at the n -th location and is equal to:

$$\tau_{p,n} = \frac{2d_{p,n}}{c} = \frac{2\lambda_m d_{p,n}}{f_m}. \quad (3.15)$$

where $d_{p,n}$ is the one-way trip distance between the p -th target/point of interest and reader antenna at the n -th location and c the speed of light.

The measured data vector $\mathbf{y} \in \mathbb{C}^{MN \times 1}$ is obtained by stacking the measurements $y[m, n]$ into a single column vector:

$$\mathbf{y} = \begin{bmatrix} y[0, 0] \\ \vdots \\ y[M-1, 0] \\ y[0, 1] \\ \vdots \\ y[M-1, N-1] \end{bmatrix}. \quad (3.16)$$

The complex reflectivities σ_p can also be vectorized in $\mathbf{s} \in \mathbb{C}^{N_x N_y \times 1}$ as follows:

$$\mathbf{s} = \begin{bmatrix} \sigma_0 \\ \sigma_1 \\ \vdots \\ \sigma_{N_x N_y - 1} \end{bmatrix}. \quad (3.17)$$

Finally the matrix $\mathbf{A} \in \mathbb{C}^{MN \times N_x N_y}$ contains the phase terms of the target model and can be modelled as:

$$\mathbf{A} = \exp \left(-j2\pi \begin{bmatrix} f_0 \tau_{0,0} & f_0 \tau_{1,0} & \cdots & f_0 \tau_{N_x N_y - 1, 0} \\ f_1 \tau_{0,0} & f_1 \tau_{1,0} & \cdots & f_1 \tau_{N_x N_y - 1, 0} \\ \vdots & \vdots & \ddots & \vdots \\ f_{M-1} \tau_{0,0} & f_{M-1} \tau_{1,0} & \cdots & f_{M-1} \tau_{N_x N_y - 1, 0} \\ f_0 \tau_{0,1} & f_0 \tau_{1,1} & \cdots & f_0 \tau_{N_x N_y - 1, 1} \\ f_1 \tau_{0,1} & f_1 \tau_{1,1} & \cdots & f_1 \tau_{N_x N_y - 1, 1} \\ \vdots & \vdots & \ddots & \vdots \\ f_{M-1} \tau_{0,N-1} & f_{M-1} \tau_{1,N-1} & \cdots & f_{M-1} \tau_{N_x N_y - 1, N-1} \end{bmatrix} \right), \quad (3.18)$$

or expressed like this:

$$\{\mathbf{A}\}_{ip} = \exp(-j2\pi f_m \tau_{pn}), \quad m = i(\bmod M), n = \lfloor i/M \rfloor, \quad (3.19)$$

$$i = 0, 1, \dots, MN - 1. \quad (3.20)$$

Using the above, the following linear system is formed, utilizing $M \times N$ measurements from RFID tags that could potentially be at $N_x \times N_y$ points:

$$\mathbf{y} = \mathbf{A}\mathbf{s}. \quad (3.21)$$

Extended Reflections Formulation

In practical scenarios, the received signal is influenced by multiple propagation paths due to obstacles and reflectors in the environment. To accurately represent this phenomenon, we can expand on the LoS formulation described above by introducing a new complex reflectivity vector, denoted as $\tilde{\mathbf{s}}$, which consolidates all the different propagation paths. Formally, the vector $\tilde{\mathbf{s}}$ is defined as:

$$\tilde{\mathbf{s}} = \left[\left(\mathbf{s}^{(0)} \right)^\top \quad \left(\mathbf{s}^{(1)} \right)^\top \quad \dots \quad \left(\mathbf{s}^{(K-1)} \right)^\top \right]^\top, \quad \tilde{\mathbf{s}} \in \mathbb{C}^{N_x N_y K \times 1}. \quad (3.22)$$

In this expression, $\mathbf{s}^{(0)}$ represents the complex reflectivity of the LoS path, whereas $\mathbf{s}^{(k)}$ represents the complex reflectivity for the k -th propagation path. The subscript $K - 1$ indicates that a total of K paths are being considered, including the LoS and various reflection paths.

To accommodate the multiple propagation paths, we also define an augmented matrix $\tilde{\mathbf{A}}(\mathbf{w})$. This matrix contains the phase terms corresponding to each of the K propagation paths:

$$\tilde{\mathbf{A}}(\mathbf{w}) = \left[\mathbf{A}^{(0)} \quad \mathbf{A}^{(1)}(\mathbf{w}) \quad \dots \quad \mathbf{A}^{(K-1)}(\mathbf{w}) \right], \quad \tilde{\mathbf{A}} \in \mathbb{C}^{MN \times N_x N_y K}. \quad (3.23)$$

In this matrix, $\mathbf{A}^{(0)}$ refers to the phase terms associated with the LoS path. All other matrices, $\mathbf{A}^{(k)}(\mathbf{w})$ for $k \geq 1$, represent the phase terms for the k -th reflected propagation path and depend non-linearly on a parameter vector \mathbf{w} . This vector encapsulates the characteristics of the various walls or reflectors in the environment.

With these new definitions, we can now represent the entire system using a linear, with respect to \mathbf{y} , $\tilde{\mathbf{A}}$ and $\tilde{\mathbf{s}}$, equation that incorporates all the propagation paths:

$$\mathbf{y} = \tilde{\mathbf{A}}(\mathbf{w}) \tilde{\mathbf{s}}. \quad (3.24)$$

It is crucial to note that while the system appears linear, the dependency on the wall parameters encapsulated in \mathbf{w} is inherently non-linear. Therefore, despite the linearized representation, the complexity of real-world environments and their non-linear interactions are accounted for in this formulation.

Solving for Known Walls

When the locations of walls and reflectors are known a priori, the reflection model expressed in Equation (3.24) can be treated as a linear system. Previous research on this subject has been conducted, such as the work presented in [48]. However, it is important to note that their study differs from the current work in several aspects. Notably, they employed wideband transceivers operating in the frequency range of 1 to 3 GHz. Moreover, their model does not take into account the propagation losses that arise in the vector \mathbf{y} .

It is important to note that each vector $\mathbf{s}^{(k)}$ is sparse and all vectors have the same support. This attribute enables us to frame the problem as an optimization task focused on minimizing the mean squared error while promoting group sparsity. Mathematically, the optimization problem can be formulated as follows:

$$\hat{\mathbf{s}} = \arg \min_{\tilde{\mathbf{s}}} \frac{1}{2} \left\| \mathbf{y} - \tilde{\mathbf{A}} \tilde{\mathbf{s}} \right\|_2^2 + \tau \|\tilde{\mathbf{s}}\|_{2,1}. \quad (3.25)$$

Here, $\|\cdot\|_{2,1}$ refers to the $l_{2,1}$ -norm, which promotes group sparsity, and τ is the regularization parameter controlling the trade-off between fidelity to the data and sparsity. The $l_{2,1}$ -norm is defined as:

$$\|\tilde{\mathbf{s}}\|_{2,1} \triangleq \sum_{p=0}^{N_x N_y - 1} \left\| \left[s_p^{(0)}, s_p^{(1)}, \dots, s_p^{(K-1)} \right]^\top \right\|_2. \quad (3.26)$$

To solve this optimization problem of Eq. (3.25), specialized numerical tools are often required. In this context, we utilize the SpaRSA toolbox [49] to find the solution.

The toolbox provides efficient algorithms for sparse reconstruction and has been proven effective for problems of similar nature.

By solving this optimization problem, we can effectively estimate the complex reflectivity vector $\tilde{\mathbf{s}}$, which enables us to localize the target.

3.3 Joint Wall and Tag Localization

In the general case of real-world applications, the environment is seldom as predictable as one would hope; any object could serve as a reflector, and thus, its precise location remains uncertain. Consequently, the wall parameter vector, denoted as \mathbf{w} , is also not definitively known. To tackle this issue, we introduce an optimization problem that aims for the joint estimation of both the wall parameter vector \mathbf{w} and the complex reflectivity vector $\tilde{\mathbf{s}}$. The optimization problem can be formally expressed as:

$$\min_{\mathbf{w}} \min_{\tilde{\mathbf{s}}} \frac{1}{2} \left\| \mathbf{y} - \tilde{\mathbf{A}}(\mathbf{w}) \tilde{\mathbf{s}} \right\|_2^2 + \tau \|\tilde{\mathbf{s}}\|_{2,1}. \quad (3.27)$$

The overall optimization problem is non-convex, but it can be dissected into two components. Specifically, the inner minimization problem involving $\tilde{\mathbf{s}}$ is convex, while the outer minimization with respect to \mathbf{w} is non-convex. This dual-structured optimization scheme can be solved in an alternate optimization manner and has precedents in literature; for example, a similar approach was employed in [50] for wall error correction. That study utilized Particle Swarm Optimization (PSO) and Quasi-Newton methods (QN) to solve the outer minimization problem, leveraging prior knowledge of wall locations obtained through building layout estimation techniques.

However, in the context of our study, we opt for a different path. Only narrowband measurements are used and no prior knowledge of wall locations is assumed. The estimation of wall positions is achieved through the use of a parameter search grid. While this grid-based approach increases the accuracy of the estimation, it simultaneously increases computational demands. To manage this heightened complexity, our strategy employs a coarsely-discretized grid initially. Once a candidate parameter, represented by $\hat{\mathbf{w}}$, is identified, we then refine this approximation by introducing random perturbations in its vicinity. The purpose of these perturbations is to fine-tune the estimate, thus offering a balance between computational efficiency and estimation accuracy.

3.4 Experimental Evaluation

Outdoor experiments were conducted in order to further examine and verify the behaviour of the proposed method. An Impinj Speedway R420 RFID reader was utilized which is able to report both the phase and the RSSI of the received signal. Due to the modeling described in the previous sections, it is possible to exploit both phase and RSSI measurements. In particular, if μ_{RS} is the RSSI measurement vector, which is converted from the reader-reported power units (dBm) to amplitude units (V) and ϕ_{reader} is the phase measurement vector in the interval $[0, 2\pi)$, then the measurements that will be included in the SpaRSA algorithm are:

$$\mathbf{y} = \mu_{\text{RS}} \odot \exp(-j\phi_{\text{reader}}). \quad (3.28)$$

Two antennas were tested, namely FlexiRay SF-2110 (circularly polarized, directional) and VERT 900 (linearly polarized, omni-directional), assuming far field conditions (2.8 m distance from reader-to-tag). Reader's transmission power was set to 30 dBm and the carrier frequency used was 866.9 MHz. A single location estimate was obtained, from about 40 phase/RSSI pairs, one from each location of the reader. Two Alien ALN-9740 (Higgs-4) RFID tags were used and IDs 1 and 2 were assigned to them. Tags 1 and 2 were placed 0.84 m and 2.35 m away from the wall, respectively. The tags and the reader were at the same height (1.52 m for FlexiRay and 1.8 m for VERT) above ground (Fig. 3.2). Aluminum foil was placed on the wall to ensure a strongly reflective surface. Intuitively, it is expected for the reflector/wall to have a stronger impact on the measurements associated with tag 1, due to its wall proximity.

Joint tag-wall localization and known wall location methods assuming 2 reflection modes (1st order or 2nd order reflection), were examined. Methods that assume only LoS were compared, namely SpaRSA with the direct path only ($K = 1$) by solving a complex LASSO problem, Weighted Cosine Likelihood Algorithm (WCLA) [51], which exploits phase measurement differences and the RDPF particle filtering method.

An exhaustive search method was also used which utilized a 1 m wall grid with a resolution of $d_w = 5$ cm (containing the wall's true location). The alternating optimization utilized 1 m wall grid with a resolution of $d_w = 20$ cm which does not coincide with the true location of the wall. The tag grid for all the methods was a $2\text{m} \times 2\text{m}$ square, with a resolution of 3 cm. The tags' grid also did not coincide with the tags' true locations.

The tag and wall localization errors are offered in Tables 3.1, 3.2, respectively. It is observed that the experiments with the directional FlexiRay, fully enjoy the benefits

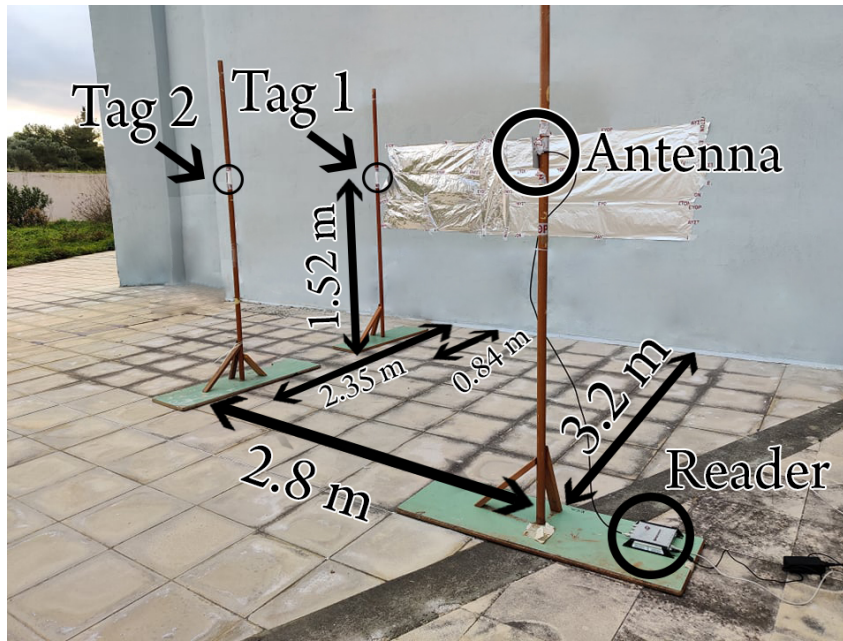


Figure 3.2: Experimental setup using aluminum foil to imitate and reinforce reflections

offered by considering a first order reflection model; it can be seen that while tag 1 is successfully localized, the localization for tag 2 fails (in the case of tag 2 larger errors are observed). That is an expected behaviour, since tag 1 suffers from a strong reflection from the side wall (due to its proximity to the wall). This consideration is also corroborated from the high error offered by the LoS methods. In the case of tag 2, which is far away from the wall, the modeling is unable to capture the reflector, because the amplitude of the reflected signal is significantly attenuated. In addition, it is important to mention that second order reflection modeling, given the radiation pattern of the FlexiRay antenna, does not fit well enough with the errors considering joint search of the tag and wall position.

For the experiments utilizing the VERT 900, the joint algorithms are failing to give the exact location of the wall. Additionally, 2nd order reflection offers smaller tag localization error for the closer-to-the-wall tag 1 (as opposed to the FlexiRay case, where 1st order performs better). In the VERT 900 case, while the localization error for the tag's location is small, the error in finding the wall's location is relatively high. These interesting findings are under investigation and it is conjectured that the utilization of the specific VERT antenna, which is omnidirectional in the horizontal plane, introduces more modes of reflection/propagation, compared to the directional FlexiRay, not taken into modelling account.

Table 3.1: Tag localization error (near wall: Tag 1, far from wall: Tag 2).

	$e = \ \mathbf{x} - \hat{\mathbf{x}}\ _2$ (cm)			
	FlexiRay		Vert 900	
	Tag 1	Tag 2	Tag 1	Tag 2
SpaRSA ($K = 1/\text{LoS}$)	79	32	82	8
WCLA	79	35	73	23
RDPF ($\sigma = 0.03$)	52	27	79	12
RDPF ($\sigma = 0.06$)	19	31	50	49
SpaRSA ($K = 2$, 1st Order)	5	20	8	11
SpaRSA ($K = 2$, 2nd Order)	5	17	8	11
Exh. Search (1st Order)	5	29	22	11
Exh. Search (2nd Order)	14	32	2	201
Alt. Opt. (1st Order)	14	29	85	11
Alt. Opt. (2nd Order)	14	201	14	201

Table 3.2: Wall localization error.

	$e = x_w - \hat{x}_w $ (cm)			
	FlexiRay		Vert 900	
	Tag 1	Tag 2	Tag 1	Tag 2
Exh. Search (1st Order)	0	10	20	5
Exh. Search (2nd Order)	45	50	50	50
Alt. Opt. (1st Order)	5	14	24	3
Alt. Opt. (2nd Order)	45	51	45	48

3.5 Conclusion

What this work clearly demonstrated is that overlooking the presence of a strong reflector while solely relying on a Line-of-Sight (LoS) model can severely compromise the accuracy and reliability of RFID-based localization systems. This oversight can result in significant performance degradation, as the model will fail to capture the complex signal interactions

in the environment. Conversely, efforts to eliminate multipath effects may be counter-productive when the reflections are considerably weak and have a minimal impact on the received signal. Such misguided attempts to mitigate non-impactful multipath reflections could inadvertently introduce new errors into the system.

The research presented here not only introduces novel algorithms for the simultaneous localization of both reflectors and tags but also underscores the critical importance of properly accounting for the various environmental conditions that can influence system performance. We have empirically demonstrated the potential pitfalls of neglecting these factors, offering a robust, real-world validation of theoretical predictions.

One promising avenue for future research involves the creation of adaptive algorithms capable of classifying environmental conditions as either LoS or non-LoS. Such algorithms should also determine the order of reflections, whether first or second order, in non-LoS settings. This type of intelligent classification can enable more accurate localization by dynamically adjusting the algorithm's assumptions based on the specific characteristics of the environment in which it operates.

Additionally, the challenges posed by limited bandwidth can be mitigated through clever experimental design, such as by increasing the spacing between measurements. This approach could make the system more robust to bandwidth limitations and possibly pave the way for the deployment of mobile readers, adding another layer of flexibility to RFID localization efforts.

In summary, this work serves as both a demonstration of the effects of undermodeling and proof of concept for future research in the realm of RFID localization. It underscores the nuanced interplay between various types of reflections and their impact on system performance, while also laying the groundwork for the development of more adaptive and intelligent localization schemes.

Chapter 4

Bistatic - Multistatic Localization

4.1 Introduction

This chapter introduces a novel approach to address estimation of Direction of Arrival (DoA) and localization by employing phase-based, narrow-band measurements and intersections of ellipses derived from the bistatic architecture model.

The research presented herein explores a unique multistatic architecture. In this setup, both the illuminating and the receiving antennas are strategically aligned in a straight line. While this arrangement might appear unconventional when compared to traditional configurations, it unlocks a suite of advantages, particularly in addressing and leveraging the inherent ambiguities of phase measurements. As we journey through this chapter, we will analyze how these ambiguities, which are typically viewed as challenges, are innovatively transformed into tools for enhanced DoA estimation.

By the end of this chapter, a comprehensive understanding of this innovative method and its comparison to the revered MUSIC algorithm will be provided. In the case of 2D localization accuracy, this approach surpasses existing state-of-the-art algorithms. Lastly, the potential of extending this method to cater to 3D scenarios will also be touched upon, offering a glimpse into future possibilities of RFID localization.

The interrogation architecture plays a pivotal role in the performance and capabilities of RFID systems. While the monostatic architecture and its applications were discussed in the previous chapters, this section focuses on the bistatic/multistatic architecture, discussing its inherent advantages, drawbacks, and its implications on DoA estimation.

In contrast with the monostatic approach, the bistatic architecture utilizes two separate antennas to handle transmission and reception, while the multistatic architecture (as a bistatic extension) can utilize multiple antennas for transmission and reception. This separation can offer enhanced flexibility in antenna placement and orientation, potentially

leading to improved coverage and signal quality. The architecture's design can help mitigate some of the challenges inherent in phase measurements, particularly the ambiguities in distance. However, the increased hardware complexity might pose challenges in terms of system cost and integration.

When it comes to the realm of DoA estimation, the choice of architecture can profoundly influence the results. The research encapsulated in this chapter leans towards a multistatic approach, which, while sharing similarities with bistatic configurations, introduces its unique advantages, especially in the elliptical DoA estimation method being presented ¹.

4.2 Problem Formulation and Phase Model

One of the fundamental challenges in RFID systems is the accurate and reliable estimation of the Direction of Arrival (DoA). Traditional methodologies often encounter challenges due to the inherent ambiguities associated with phase measurements. These ambiguities, which are a consequence of the periodic nature of phase, introduce uncertainties in distance estimations. Let's formulate this more explicitly.

Within the domain of RFID localization, multistatic setups offer a unique advantage due to their diverse observational viewpoints. In the configuration posited in this work, a single transmitter (Tx) antenna works in tandem with a set of $M > 1$ receiver (Rx) antennas, all of which are precisely aligned along the same line, unless specified otherwise.

For this co-linear arrangement, the Tx and Rx antennas, in conjunction with the RFID tag, define a distinct plane. The RFID tag's position on this plane is denoted as $\mathbf{x}_T \triangleq [x_{\text{tag}} \ y_{\text{tag}}]^T$. Similarly, the positions of the Tx and Rx antennas on this plane are denoted as $\mathbf{x}_{\text{Tx}} \triangleq [x_{\text{Tx}} \ y_{\text{Tx}}]^T$ and $\mathbf{x}_{\text{Rx},i} \triangleq [x_{\text{Rx},i} \ y_{\text{Rx},i}]^T$, with i spanning from 1 to M representing the i^{th} receiving antenna, respectively. It is also noted that the Tx and Rx antennas are facing towards the same direction, effectively covering the same half-plane.

The end-2-end complex channel gain for path i is denoted as follows:

$$h_i = h_{\text{CT}} h_{\text{TR},i} = |h_{\text{CT}} h_{\text{TR},i}| e^{-j\phi_i} \in \mathbb{C}, \quad (4.1)$$

where h_{CT} and $h_{\text{TR},i}$ denote the baseband complex channel coefficients for the TX (Carrier emitter) antenna-to-tag and tag-to- i^{th} Receiver antenna, respectively. Furthermore, $h_i \in \mathbb{C}$, $|h_{\text{CT}} h_{\text{TR},i}| \in \mathbb{R}_+$ and $\phi_i \in [0, 2\pi)$. Thus, the induced phase of the propagation i^{th} path can be expressed as follows:

¹A more extensive version of this work has been conducted by Konstantinos Skyvalakis and is presented as a part of his master's thesis [52].

$$\phi_{\text{prop},i} \equiv \phi_i = \angle h_i = \frac{2\pi}{\lambda}(d_{CT} + d_{TR,i}) + \phi_i^{\text{mult}}, \quad (4.2)$$

where $d_{CT} \triangleq \|\mathbf{x}_{\text{Tx}} - \mathbf{x}_{\text{T}}\|_2$ denotes the Euclidean distance between the Tx antenna and the RFID tag, $d_{TR,i} \triangleq \|\mathbf{x}_{\text{Rx},i} - \mathbf{x}_{\text{T}}\|_2$ denotes the Euclidean distance between the tag and the i^{th} Rx antenna, λ represents the carrier wavelength and the ϕ_i^{mult} accounts for phase shifts induced by the multipath effect during transmission from the Tx antenna and reception from the i^{th} Rx antenna.

In multistatic configurations, it is common to have each Tx and Rx antenna belonging to separate devices. Given that every individual device operates with its unique internal oscillator, there is an inherent risk of slight discrepancies causing carrier frequency offsets (CFO) and carrier phase offsets (CPO) between the devices.

In this work, these offsets were mitigated by utilizing an external function generator, effectively synchronizing the different software-defined radios (SDR) used.

Similarly to what was described in the previous chapters, the phase measured at the reader is influenced by a number of factors aside from the spatial configuration and the direct transmission channel. The tag's type and its reflection coefficient induce a phase variation represented by the term ϕ_{tag} . In addition, the constant phase offset $\hat{\phi}_0$ from cabling delays as well as the variable phase noise $\hat{\phi}_i^n$, must be considered.

Taking into account all these determinants, the comprehensive phase model at Rx i can be delineated as follows:

$$\begin{aligned} \phi_{\text{out},i} &= \phi_{\text{prop},i} + \hat{\phi}_0 + \phi_{\text{tag}} + \hat{\phi}_i^n \\ &= \frac{2\pi}{\lambda}(d_{CT} + d_{TR,i}) + \underbrace{\phi_i^{\text{mult}} + \hat{\phi}_0 + \phi_{\text{tag}} + \hat{\phi}_i^n}_{\phi_i^n} \\ &= \frac{2\pi}{\lambda}(d_{CT} + d_{TR,i}) + \phi_i^n \end{aligned}$$

Since the phase measured by typical RFID readers is periodic in the range $[0, 2\pi)$, a modulo operator has to be applied to $\phi_{\text{out},i}$ to obtain the measured phase:

$$\begin{aligned}
\phi_{R_x,i} &= \phi_{\text{out},i} \bmod 2\pi \\
&= \left[\frac{2\pi}{\lambda} (d_{CT} + d_{TR,i}) + \phi_i^n \right] \bmod 2\pi \\
&\stackrel{(*)}{=} \left[\frac{2\pi}{\lambda} (d_{CT} + d_{TR,i}) \bmod 2\pi + \underbrace{\phi_i^n \bmod 2\pi}_{\tilde{\phi}_i^n} \right] \bmod 2\pi \\
&= \left[\frac{2\pi}{\lambda} (d_{CT} + d_{TR,i}) \bmod 2\pi + \tilde{\phi}_i^n \right] \bmod 2\pi,
\end{aligned} \tag{4.3}$$

where at $\stackrel{(*)}{=}$, the property $(\alpha + \beta) \bmod \gamma = [(\alpha \bmod \gamma) + (\beta \bmod \gamma)] \bmod \gamma$ was exploited and $\tilde{\phi}_i^n$ the phase noise term with support in $[0, 2\pi)$.

Temporarily ignoring the phase noise term $\tilde{\phi}_i^n$ and solving the above equation for the sum of distances:

$$d_{CT} + d_{TR,i} = \lambda \frac{\phi_{R_x,i}}{2\pi} + k_i \lambda, \quad k_i \in \mathbb{N}, \tag{4.4}$$

we can clearly observe the source of the distance ambiguity inherent in the conversion of phase measurement to distance since the same phase measurement $\phi_{R_x,i}$ corresponds to an infinite number of sum of distances that differ by λ .

4.3 Ellipses based Method and Ambiguity Resolution

Addressing the intricacies of distance ambiguity and phase noise stands as the cardinal challenge of this research. The approach described in the chapter is based on leveraging the geometric properties derived by the phase model described above. This work introduces a novel technique for estimating the direction of arrival and localizing tags. Central to this technique are the ellipses derived from the phase model. This distinctive utilization of ellipses lends the method its distinctive moniker: Elliptical DoA (ElIDoA).

As can be seen in Eq. (4.4), given a receiving antenna i and its phase measurement, a set of compound distance values $(d_{CT} + d_{TR,i})$, can be calculated for a number of k_i values in the $\{0, 1, \dots, K\}$ set. Each of those compound distances defines a concentric ellipse on the plane with foci the locations of the Tx and i^{th} Rx antennas. For a clearer visualization of this intricate geometric arrangement, one may refer to Fig. 4.1, which showcases the

scenario with $M = 2$ Rx antennas and a total of $K = 5$ concentric ellipses for each Tx-Rx pair.

According to the model described above, Eq. (4.4) provides the major axis $2a_i$ (longest diameter) of the ellipse:

$$2a_i[k_i] = (d_{CT} + d_{TR,i}) = \lambda \frac{\phi_{Rx,i}}{2\pi} + k_i \lambda. \quad (4.5)$$

The linear eccentricity c_i (and the semi-minor axis $b_i[k_i]$, assuming $b_i[k_i] \leq a_i[k_i]$) can be easily found using the known coordinates of the foci; c_i is independent of k_i :

$$c_i = \|\mathbf{x}_{Tx} - \mathbf{x}_{Rx,i}\|_2/2, \quad (4.6)$$

$$b_i[k_i] = \sqrt{a_i^2[k_i] - c_i^2}. \quad (4.7)$$

To estimate the Direction of Arrival (DoA) of a tag's signal, a configuration with only two receiving antennas is required. Specifically, we focus on cases where the number of antennas M is set to 2, corresponding to the indices $i \in 1, 2$.

By convention, it is assumed that all antennas, whether transmitting or receiving, are positioned along the x -axis. Thus, the coordinate vector for the transmitting antenna is denoted as $\mathbf{x}_{Tx} \triangleq [x_{Tx} \ 0]^T$ and for the i^{th} receiving antenna, it is represented by $\mathbf{x}_{Rx,i} \triangleq [x_{Rx,i}^i \ 0]^T$. Given this configuration, the central points of the ellipses generated from each receiving antenna's measurement are also located on the x -axis².

An essential parameter in this setup is δx , which denotes the distance between the two receiving antennas. It is defined as $\delta x \triangleq |x_{Rx}^1 - x_{Rx}^2|$.

Building on the above framework, the ellipses associated with the measurements from the two receiving antennas (for $i \in 1, 2$) can be mathematically characterized by the equation:

$$\frac{(x - x_i)^2}{a_i^2[k_i]} + \frac{y^2}{b_i^2[k_i]} = 1, \quad k_i \in 0, \dots, K, \quad (4.8)$$

²It is worth noting that this convention is not necessary. Even if the entire setup was mobile and could be rotated, we could always translate and remap our coordinate system so that the antennas retain their position on the x -axis. This ensures notational simplicity and consistency regardless of the actual physical orientation of the equipment. This aspect of the design is particularly advantageous when considering real-world scenarios in which antenna configurations might need to be adjusted or moved.

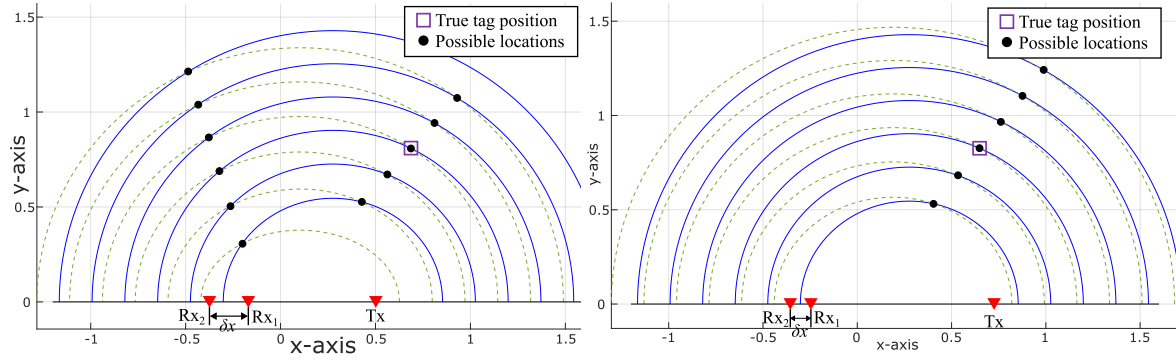


Figure 4.1: EllDoA method; with (left), without (right) ambiguity; $\delta x > \lambda/2$, $\delta x < \lambda/2$, respectively.

where the coordinates $(x_1, 0)$ and $(x_2, 0)$ denote the centers of the ellipses derived from the first and second receiving antennas, respectively. These centers can be straightforwardly determined given the known positions of the antennas.

One of the most compelling features of this setup is its ability to pinpoint the DoA of a signal based on the intersection points of the ellipses produced by the two receiving antennas. An illustration of this can be found in Fig. 4.1-left. However, a challenge arises in the form of ambiguity: the two ellipses might intersect at two distinct points, suggesting two potential DoA directions. While one way to resolve this ambiguity involves dynamically steering the antenna axis (using mechanisms such as a robotic platform), this might be operationally complex and not always feasible.

Remarkably, this is where the theorem provides a pivotal insight. If the inter-antenna spacing δx is constrained such that $\delta x < \lambda/2$ (with λ representing the wavelength of the signal), the ambiguity is naturally eradicated. The unambiguous DoA estimation when adhering to this constraint can be visualized in Fig. 4.1-right. With a reduced inter-antenna spacing, the ellipses' intersections are limited, alleviating the challenge of multiple DoA estimations.

Lemma 4.1. *Assuming one Tx and two Rx antennas are located on the same line, if the distance δx between the two receiving antennas is $\delta x < \lambda/2$, then a unique direction of arrival (DoA) θ of the tag signal can be found, irrespective of the location of the Tx antenna.*

The lemma is a direct consequence of the following theorem, which offers such unique DoA in closed form, when $\delta x < \lambda/2$.

Theorem 4.1. Assume one Tx and two Rx antennas located at the same line, $\phi_A \equiv \phi_{Rx,1}$, $\phi_B \equiv \phi_{Rx,2}$ denote the phase at the receiving antennas, respectively and $\alpha \triangleq \|\mathbf{x}_T - \mathbf{x}_{Rx,1}\|_2$, $\beta \triangleq \|\mathbf{x}_T - \mathbf{x}_{Rx,2}\|_2$.

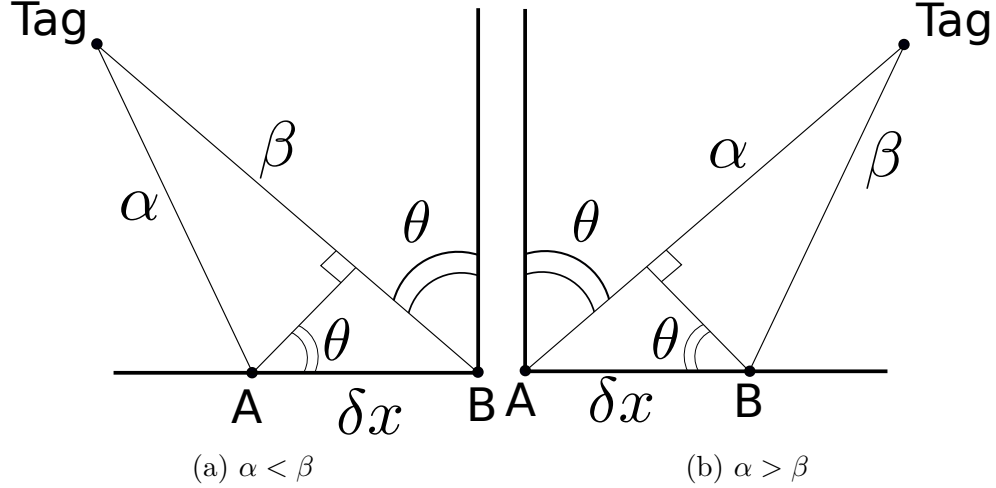


Figure 4.2: Direction of Arrival (DoA) angle θ .

If the distance δx between two receiving antennas satisfies $\delta x < \lambda/2$, then direction of arrival (DoA) $\theta \in (0, \pi/2)$ of the tag signal (Fig. 4.2) i.e., the angle between the direction of arrival and the perpendicular to the line of the antennas, passing from one of the Rx antennas (from receiving antenna that offers ϕ_A if $\alpha > \beta$, or from receiving antenna that offers ϕ_B if $\beta > \alpha$), shown in Fig. 4.2, is given by:

For $\alpha > \beta$,

$$\theta \approx \begin{cases} \sin^{-1} \left(\frac{\lambda(\phi_A - \phi_B)}{2\pi \delta x} \right), & \text{if } \phi_A > \phi_B, \\ \sin^{-1} \left(\frac{\lambda(\phi_A - \phi_B + 2\pi)}{2\pi \delta x} \right), & \text{if } \phi_A < \phi_B. \end{cases}$$

and for $\alpha < \beta$,

$$\theta \approx \begin{cases} \sin^{-1} \left(-\frac{\lambda(\phi_A - \phi_B - 2\pi)}{2\pi \delta x} \right), & \text{if } \phi_A > \phi_B, \\ \sin^{-1} \left(-\frac{\lambda(\phi_A - \phi_B)}{2\pi \delta x} \right), & \text{if } \phi_A < \phi_B. \end{cases}$$

Theorem 4.1 assumes far-field propagation, i.e., tag is located at least 10λ away from the antennas, so that according to Fig. 4.2, $\sin \theta \approx (\alpha - \beta)/\delta x$ for $\alpha > \beta$ (and a similar approximation for $\beta > \alpha$). The theorem's proof follows:

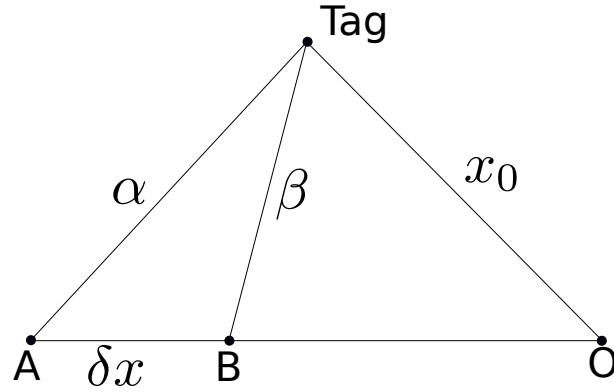


Figure 4.3: Topology of one Tx (point O), two Rx antennas (points A and B) and a tag.

Proof of Theorem

Proof. Lets assume that one Tx and two Rx antennas are placed at collinear points **O**, **A** and **B** respectively. A tag is placed on a random location as depicted in Fig. 4.3.

According to this topology and using Eq. (4.3) ignoring the noise term $\tilde{\phi}_i^n$, the phase measured by the two antennas can be expressed as:

$$\phi_B = \frac{\beta + x_0}{\lambda} \cdot 2\pi \bmod 2\pi \quad (4.9)$$

and taking into account that $(x + y) \bmod 2\pi = (x \bmod 2\pi + y \bmod 2\pi) \bmod 2\pi$,

$$\begin{aligned} \phi_A &= \frac{\alpha + x_0}{\lambda} \cdot 2\pi \bmod 2\pi \\ &= \frac{\alpha + x_0 + \beta - \beta}{\lambda} \cdot 2\pi \bmod 2\pi \\ &= \left(\frac{x_0 + \beta}{\lambda} \cdot 2\pi + \frac{\alpha - \beta}{\lambda} \cdot 2\pi \right) \bmod 2\pi \\ &= \left(\frac{x_0 + \beta}{\lambda} \cdot 2\pi \bmod 2\pi + \frac{\alpha - \beta}{\lambda} \cdot 2\pi \bmod 2\pi \right) \bmod 2\pi \\ &= \left(\phi_B + \left(\frac{\alpha - \beta}{\lambda} \cdot 2\pi \right) \bmod 2\pi \right) \bmod 2\pi. \end{aligned} \quad (4.10)$$

Assuming that $\delta x < \lambda/2$, from the triangular inequality it holds that:

$$\begin{aligned} |\alpha - \beta| &< \delta x \\ \Rightarrow |\alpha - \beta| &< \lambda/2 \end{aligned} \quad (4.11)$$

Lets suppose now that $\alpha > \beta$, Eq. (4.11) can be written as:

$$\begin{aligned} 0 &< \alpha - \beta < \lambda/2 \\ 0 &< \frac{\alpha - \beta}{\lambda} \cdot 2\pi < \pi. \end{aligned} \quad (4.12)$$

Thus, from Eqs. (4.10), (4.12) we obtain:

$$\begin{aligned} \phi_A &= \left(\phi_B + \frac{\alpha - \beta}{\lambda} \cdot 2\pi \right) \bmod 2\pi \\ \Rightarrow \phi_B + \frac{\alpha - \beta}{\lambda} \cdot 2\pi &= \phi_A + k2\pi \\ \Rightarrow \phi_A - \phi_B &= \frac{\alpha - \beta}{\lambda} \cdot 2\pi - k2\pi. \end{aligned} \quad (4.13)$$

Assuming that $\phi_A > \phi_B$ and since $\phi_A, \phi_B \in [0, 2\pi)$,

$$\begin{aligned} 0 &< \phi_A - \phi_B < 2\pi \\ \stackrel{(4.13)}{\Rightarrow} 0 &< \frac{\alpha - \beta}{\lambda} \cdot 2\pi - k2\pi < 2\pi \\ \stackrel{(4.12)}{\Rightarrow} k &= 0, \end{aligned} \quad (4.14)$$

while if $\phi_A < \phi_B$,

$$\begin{aligned} -2\pi &< \phi_A - \phi_B < 0 \\ \stackrel{(4.13)}{\Rightarrow} -2\pi &< \frac{\alpha - \beta}{\lambda} \cdot 2\pi - k2\pi < 0 \\ \stackrel{(4.12)}{\Rightarrow} k &= 1. \end{aligned} \quad (4.15)$$

Thus for $\alpha > \beta$,

$$\phi_A - \phi_B = \frac{\alpha - \beta}{\lambda} \cdot 2\pi, \quad \text{if } \phi_A > \phi_B, \quad (4.16)$$

and

$$\phi_A - \phi_B = \frac{\alpha - \beta}{\lambda} \cdot 2\pi - 2\pi, \quad \text{if } \phi_A < \phi_B. \quad (4.17)$$

In the far field of the antennas and for $\alpha > \beta$, it is safe to claim the following, stemming from Fig. 4.2-right:

$$\begin{aligned}
\alpha - \beta &\approx \delta x \sin \theta \\
\Rightarrow \sin \theta &\approx \frac{\alpha - \beta}{\delta x} \\
\Rightarrow \sin \theta &\approx \begin{cases} \frac{\lambda \cdot (\phi_A - \phi_B)}{\delta x \cdot 2\pi}, & \text{if } \phi_A > \phi_B \\ \frac{\lambda \cdot (\phi_A - \phi_B + 2\pi)}{\delta x \cdot 2\pi}, & \text{if } \phi_A < \phi_B \end{cases}, \quad (4.18)
\end{aligned}$$

and $\theta \in (0, \pi/2)$. Solving for θ , offers the first part of the theorem.

Similarly, for $\alpha < \beta$ the following hold:

$$\begin{aligned}
0 &< -(\alpha - \beta) < \delta x < \lambda/2 \\
\Rightarrow 0 &< -\frac{\alpha - \beta}{\lambda} \cdot 2\pi < \pi \\
\Rightarrow -\pi &< \frac{\alpha - \beta}{\lambda} \cdot 2\pi < 0 \quad (4.19)
\end{aligned}$$

Then from Eqs. (4.10), (4.19), the following holds:

$$\begin{aligned}
&\left(\phi_B + 2\pi + \frac{\alpha - \beta}{\lambda} \cdot 2\pi \right) \bmod 2\pi = \phi_A \\
\Rightarrow \phi_B + 2\pi + \frac{\alpha - \beta}{\lambda} \cdot 2\pi &= k2\pi + \phi_A \\
\Rightarrow \phi_A - \phi_B = 2\pi + \frac{\alpha - \beta}{\lambda} \cdot 2\pi - k2\pi \quad (4.20)
\end{aligned}$$

Assuming that $\phi_A > \phi_B$ and $\phi_A, \phi_B \in [0, 2\pi)$,

$$\begin{aligned}
0 &< \phi_A - \phi_B < 2\pi \\
\stackrel{(4.20)}{\Rightarrow} 2\pi + \frac{\alpha - \beta}{\lambda} \cdot 2\pi - k2\pi &< 2\pi \\
\stackrel{(4.19)}{\Rightarrow} k &= 0, \quad (4.21)
\end{aligned}$$

while if $\phi_A < \phi_B$,

$$\begin{aligned}
-2\pi &< \phi_A - \phi_B < 0 \\
\stackrel{(4.20)}{\Rightarrow} -2\pi &< 2\pi + \frac{\alpha - \beta}{\lambda} \cdot 2\pi - k2\pi < 0 \\
\stackrel{(4.19)}{\Rightarrow} k &= 1. \quad (4.22)
\end{aligned}$$

Thus, for $\alpha < \beta$,

$$\phi_A - \phi_B = \frac{\alpha - \beta}{\lambda} \cdot 2\pi + 2\pi, \quad \text{if } \phi_A > \phi_B, \quad (4.23)$$

and

$$\phi_A - \phi_B = \frac{\alpha - \beta}{\lambda} \cdot 2\pi, \quad \text{if } \phi_A < \phi_B. \quad (4.24)$$

In the far field of the antennas and for $\alpha < \beta$, it is safe to claim the following, stemming from Fig. 4.2-left:

$$\begin{aligned} \beta - \alpha &\approx \delta x \sin \theta \\ \Rightarrow \sin \theta &\approx -\frac{\alpha - \beta}{\delta x} \\ \Rightarrow \sin \theta &\approx \begin{cases} -\frac{\lambda \cdot (\phi_A - \phi_B - 2\pi)}{\delta x \cdot 2\pi}, & \text{if } \phi_A > \phi_B \\ -\frac{\lambda \cdot (\phi_A - \phi_B)}{\delta x \cdot 2\pi}, & \text{if } \phi_A < \phi_B \end{cases}, \end{aligned} \quad (4.25)$$

and $\theta \in (0, \pi/2)$. Solving for θ , offers the second part of the theorem, concluding the proof. □

4.4 Elliptical DoA Estimation and Localization

4.4.1 Multistatic Elliptical DoA Estimation (EllDoA)

To achieve an accurate estimation of a tag's signal Direction of Arrival (DoA), two trivial conditions must be met:

- First, the spacing between adjacent receiving antennas should be less than half the wavelength of the signal, mathematically denoted as $\delta x < \lambda/2$. This condition helps mitigate directional ambiguities, as was elucidated earlier.
- Second, any intersection points that occur behind the receiver antennas must be completely ignored. This is critical because these points do not contribute to a valid DoA estimation and correspond to a complementary angle.

Upon meeting these conditions, one can proceed to estimate the DoA using any of the intersection points that satisfy the second condition. The coordinates of such an intersection point are represented as $\mathbf{p} = [p[1] \ p[2]]$.

The DoA estimate is then computationally derived using the formula:

$$\hat{\theta}_0 = 90^\circ - \tan^{-1} \left(\frac{p[2]}{p[1] - x_s} \right) \cdot \frac{180^\circ}{\pi}. \quad (4.26)$$

In this equation, $x_s = \frac{x_{\text{Rx}}^1 + x_{\text{Rx}}^2}{2}$ represents the x -axis coordinate of the midpoint between the two receiving antennas. This is particularly useful if the antennas are not positioned at the origin of the coordinate system. The arctangent function $\tan^{-1}(\cdot)$ returns an angle in the closed interval $[-\pi, \pi]$, and the final DoA estimate $\hat{\theta}_0$ ranges within the $[-90^\circ, 90^\circ]$ interval.

For enhanced robustness and to account for potential variations, one can improve the DoA estimate by averaging over K intersection points \mathbf{p}_k . The refined estimate is given by:

$$\hat{\theta}_0 = 90^\circ - \frac{1}{K} \sum_{k=1}^K \tan^{-1} \left(\frac{p_k[2]}{p_k[1] - x_s} \right) \cdot \frac{180^\circ}{\pi}, \quad (4.27)$$

By incorporating multiple intersection points into the estimation process, this approach yields a more reliable and robust DoA estimate, thereby enhancing the system's overall performance.

4.4.2 Multistatic 2D Localization

Extending the multistatic setup to include a third receiver antenna dramatically improves the system's capability to uniquely identify a target's location. Specifically, within the constraints and assumptions of this work—such as all antennas being positioned along the same line—the incorporation of a third receiver ensures that there exists a single, unique point on the half-plane where all three ellipses intersect. This crucial insight is illustrated in Fig. 4.4.

There are multiple methodologies to ascertain these unique intersection points, each with its own merits:

1. **Conic Section Intersection:** The first method employs the geometric intersection rules for conic sections as delineated in the work by [53]. This approach mathematically solves for the points where the ellipses intersect.
2. **Double DoA Intersection:** A second approach calculates two separate DoA estimates using the receiver pairs Rx1 - Rx2 and Rx2 - Rx3. Lines passing through the

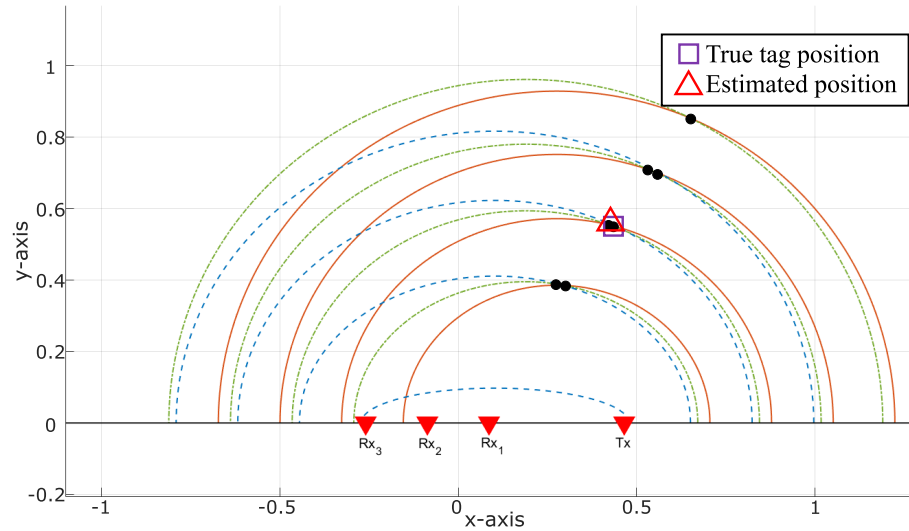


Figure 4.4: 2D localization requires a third antenna in the same line.

midpoints (medians) of these two antenna pairs are drawn, and their intersection point is computed. This method capitalizes on simplicity of the intersection of two lines, minimizing the computational effort required.

3. **Equation Equating Method:** The third method involves directly equating the left-hand sides of Eq. (4.9) for all possible pairs of $i = 1, 2, 3$. This generates a set of equations that can be solved to find the common intersection point of all three pairs. Given the special condition that all ellipse foci lie on the same line, these equations turn out to be relatively simple to solve.

Each of these methodologies offers its own set of advantages and disadvantages, including computational efficiency, ease of implementation, and robustness against noise or errors. However, what remains consistent across all three is the ability to uniquely pinpoint the target's location when a third receiver antenna is incorporated into the setup.

4.4.3 Multistatic 3D Localization

Extending the system to a three-dimensional (3D) environment involves a few additional complexities but is highly feasible within the framework of this study. Specifically, the methodology allows for an easy transition to 3D localization with the introduction of a fourth receiver antenna.

In a scenario where a tag may not necessarily be at the same height as the reader's antennas, the 2D localization method—utilizing three co-linear receiver antennas—pro-

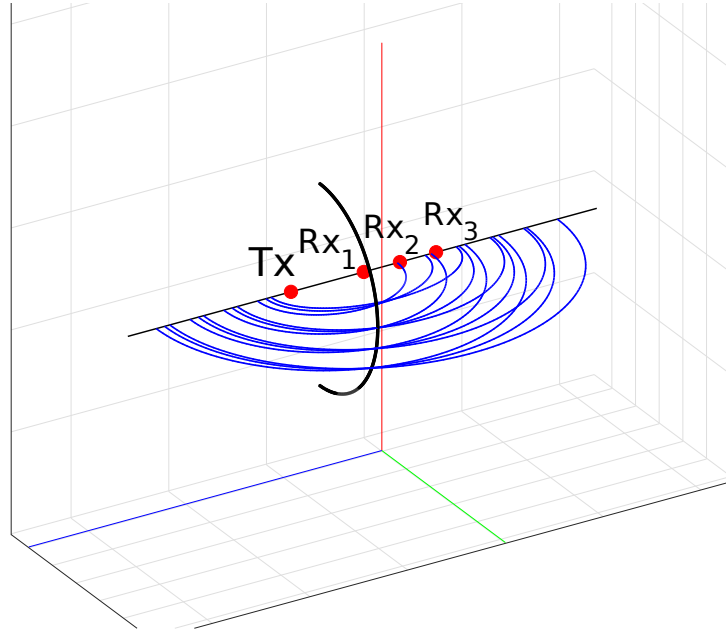


Figure 4.5: The possible tag locations in 3D form a half-circle pivoted around the axis that the receiving antennas lay.

vides an initial estimate. This method, outlined in Sec. 4.4.2, assumes that the tag exists in the same plane as that of the reader’s antennas, resulting in an estimated 2D location. However, this location may not be accurate since it rests on the assumption that the tag is at the same height as the antennas, an assumption which does not hold true when localizing a tag in 3D space.

To generalize this to 3D, imagine the ellipses “*pitching up and down*” akin to a door swinging on its hinge. This swinging action reveals that the tag can essentially be located anywhere along a half-circle in the 3D space. The half-circle essentially represents all the possible locations where the tag could be, assuming it’s not restricted to the height of the antennas. This is visually represented in Fig. 4.5.

To accurately pinpoint a single location for the tag in this 3D half-circle, the inclusion of a fourth receiver antenna becomes necessary. This additional antenna should be positioned not in line or at the same height as the other three antennas. In our specific example, the fourth receiver antenna is placed above the first Rx antenna but at a different elevation, thereby introducing a new set of K ellipses.

It can be shown that there exists a unique intersection point between this new set of ellipses generated by the fourth Rx antenna and the aforementioned 3D half-circle. This single intersection point explicitly identifies the true location of the tag in 3D space. The entire concept and proof of uniqueness of this intersection point falls out of the context of this primal 3D localization technique, but a visualization can be seen in Fig. 4.6.

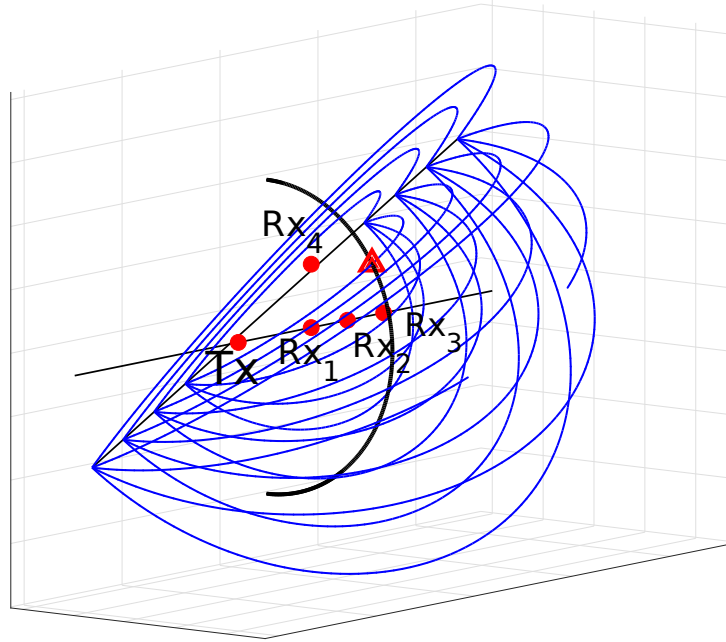


Figure 4.6: 3D localization can be achieved utilizing a fourth antenna at a different height.

Therefore, the addition of a fourth, non-collinear receiver antenna effectively resolves the inherent ambiguity in 3D tag localization, enhancing the system's capabilities and ensuring a unique solution for the tag's spatial coordinates.

4.5 Experimental Evaluation

In this section, performance evaluation of the proposed algorithms for Direction of Arrival (DoA) estimation as well as 2D and 3D localization is conducted. The evaluation is executed through two distinct methodologies: 1) computer-based simulations using MATLAB and 2) empirical testing utilizing actual experimental data. These two approaches enable us to comprehensively assess the efficacy and robustness of our proposed algorithms, under both idealized and real-world conditions.

In all experiments, a Gen2 UHF RFID tag of type ZEBRA 4"×2" Z-PERFORM 1500T was affixed to an empty box. The box was strategically placed at varying distances ranging from 0.6 m to 1.7 m away from the antennas. The specifics of the experimental setup are illustrated in Fig. 4.7. The hardware included two USRP N200 Software Defined Radio (SDR) devices, each fitted with an SBX-40 daughterboard, facilitating the implementation of a Gen2 RFID reader operating at a frequency of 868 MHz [54].

For the receiving end, two circularly-polarized MTI MT-242032 antennas were used, each boasting a gain of 7 dBic. On the transmitting side, a single FlexiRay SF-2110

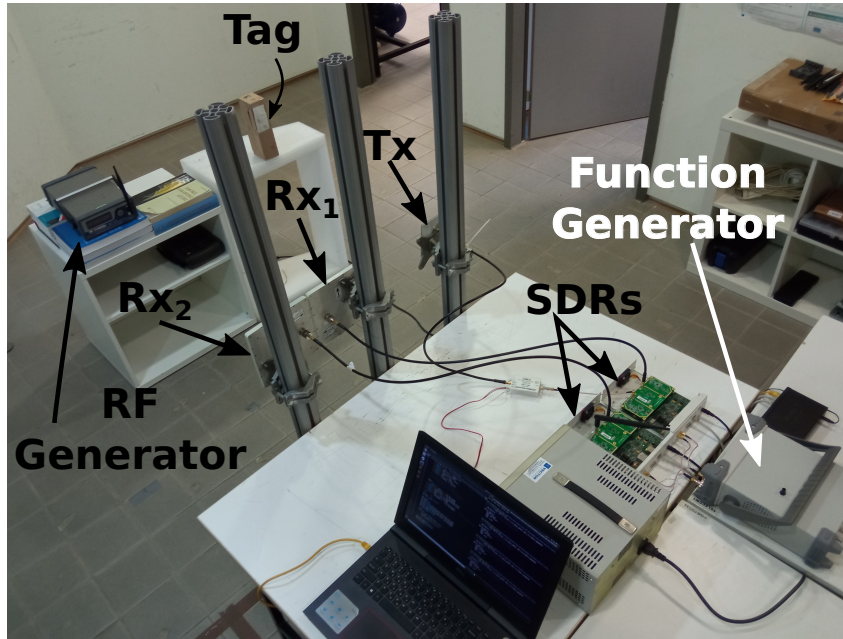


Figure 4.7: Experimental setup for Elliptical DoA and 2D localization.

antenna with a 5 dBi gain was utilized. For the DoA and 2D localization experiments, all antennas and the RFID tag were aligned at the same height, and three different heights—0.9 m, 1.2 m, and 1.5 m—were tested out. In these configurations, the orientation of the tag was designed to be parallel to the face of the antennas.

To ensure precise synchronization, a function generator provided a common 10 MHz reference clock and a 1 Pulse Per Second (PPS) input to both USRPs. This was achieved using cables of equal length. UHD Timed commands were employed to synchronize the two SDRs, adhering to the manufacturer’s guidelines. Although during the experiments, it was observed that the two SDRs demonstrated four constant and randomly repeating phase offsets.

To compensate for these phase offsets, an RF signal generator was utilized. This generator was placed 1 m away from the median of the receiver antennas at a Direction of Arrival (DoA) of 0° and equidistant from both receiving antennas. Prior to initiating the reader’s interrogation process, this RF signal generator emitted a 868 MHz tone, which was essential for ensuring synchronization and compensating the random constant phase offset.

An angle finder tool was utilized to measure the true DoA of the backscattered signal, necessary for comparison to the estimated DoA and for the placement of the RF signal generator.

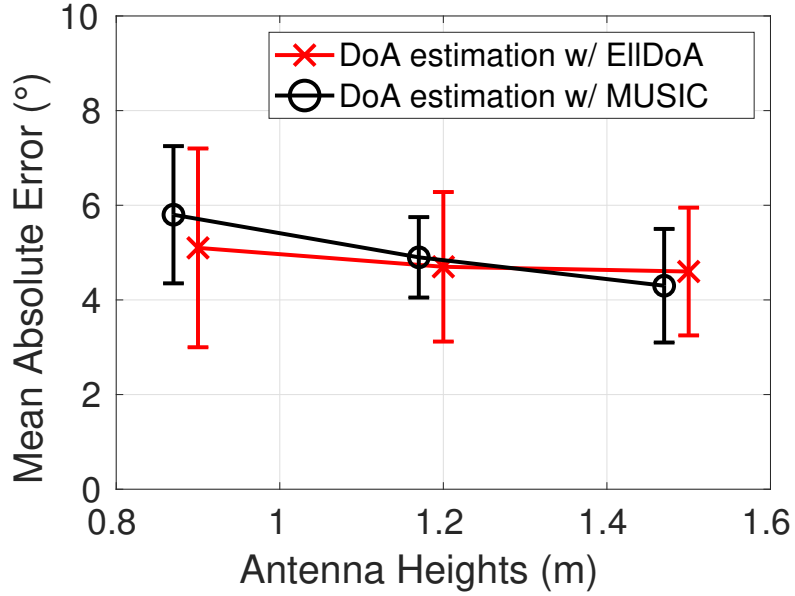


Figure 4.8: MUSIC vs ElIDoA mean absolute error estimation with ± 1 standard deviation.

Finally, a 24 dB amplifier was incorporated into the setup on the transmitting chain, and a network switch was used to facilitate the connection between the two USRPs and the laptop computer that was controlling the experiment.

The above setup allowed for rigorous testing of the proposed DoA estimation and 2D localization algorithms under real-world conditions, providing valuable insights into their performance and limitations.

4.5.1 Experimental Evaluation of ElIDoA vs MUSIC

A total of $N_e = 20$ experiments were conducted for each of the antenna heights tested, yielding a robust set of data for analysis. The transmission power of the reader was set at 25 dBm. Additionally, an angle finder tool was employed to measure the true Direction of Arrival (DoA) of the backscattered signal. This true DoA served as a reference point for assessing the accuracy of the estimated DoA obtained through the proposed algorithms. Various angles were tested during the experiments, while the RFID tag was randomly placed from 1 m, up to 1.7 m away from the antenna array. The Mean Absolute Error was measured as follows:

$$\text{MAE} = \frac{\sum_{i=1}^{N_{\text{exp}}} |\theta_0^i - \hat{\theta}_0^i|}{N_{\text{exp}}}, \quad (4.28)$$

where θ_0^i and $\hat{\theta}_0^i$ are the true and estimated DoA of the i^{th} experiment, respectively.

The comparative results of the MUSIC and EllDoA algorithms is depicted in Fig. 4.8. The data clearly indicate that both algorithms exhibited comparable performance, as reflected by the mean absolute error (MAE) values which ranged approximately between 4° and 5° . Moreover, it is shown that the estimation error is reduced for higher elevations since the impact of the ground reflection is weakened.

These results not only validate the effectiveness of the proposed EllDoA algorithm but also demonstrate its competitive performance and simplicity when juxtaposed with the established MUSIC algorithm. Hence, the experimental evaluations corroborate the feasibility and reliability of the proposed DoA estimation.

4.5.2 Experimental Evaluation of 2D Localization Algorithms

The same experimental setup with the DoA experiments was also used for the 2D localization evaluation. However, due to hardware constraints it was not possible to utilize a third synchronized antenna. In order to bypass this limitation, it was decided to emulate the presence of the third receiver antenna. This was achieved by relocating the second antenna to a predefined position, denoted as $(x_{\text{Rx}}^3, y_{\text{Rx}}^3)$, after the desired 500 interrogation rounds were completed. This relocation was performed without interrupting the reader's ongoing processes, thus mitigating the need for another calibration step. By strategically averaging over specific time intervals—essentially, periods when the antennas were static—we effectively gathered phase measurements from three distinct Rx antenna positions.

Two transmission power levels were assessed: 20 dBm and 25 dBm at the amplifier's output. For each power level and methodology, $N_e = 10$ experiments were performed at each of the antenna heights while the tags were placed randomly at a distance of 0.6 m to 1.7 m from the antenna array. To ascertain the true position of the tags, (x_T, y_T) , a laser distance meter was employed. This data was critical for quantifying the error in the tags' localization estimate. The algorithms executed swiftly, with all completion times falling under 1 second. This efficiency is attributable to the relatively low number of ellipses, $K = 15$, used for each bistatic pair which can theoretically cover a distance of up to 2.5 m.

Benchmarking was also performed against existing the particle filtering algorithm RDPF described in Chapter 2, ReLock [21], and a variant of BackPos [43]. RDPF and ReLock were tested using phase measurements from a monostatic RFID reader mounted on a mobile robot in our laboratory. For BackPos, which employs phase difference and hyperbolic intersections, measurements were manually collected by moving an antenna

Table 4.1: Experimental MAE/RMSE localization results.

Height	Loc. Method	Tx Power	$\mathbb{E}[e]$ (cm)	$\sqrt{\mathbb{E}[e ^2]}$ (cm)
0.9 m	Multistatic	20 dBm	12.85	13.29
		25 dBm	12.39	13.21
	RDPF	20 dBm	15.24	15.74
		25 dBm	15.77	16.14
	ReLock	20 dBm	23.26	24.23
		25 dBm	17.19	17.57
	BackPos	20 dBm	47.79	62.18
		25 dBm	26.4	27.64
1.2 m	Multistatic	20 dBm	10.27	10.64
		25 dBm	10.91	11.73
	RDPF	20 dBm	14.98	15.21
		25 dBm	15.58	16.32
	ReLock	20 dBm	19.54	20.67
		25 dBm	17.12	17.39
	BackPos	20 dBm	37.28	46.75
		25 dBm	40.16	45.53
1.5 m	Multistatic	20 dBm	9.18	9.98
		25 dBm	9.55	10.06
	RDPF	20 dBm	15.83	16.25
		25 dBm	15.68	15.89
	ReLock	20 dBm	17.89	18.96
		25 dBm	17.38	17.68
	BackPos	20 dBm	34.97	38.34
		25 dBm	51.06	62.95

pole along a 3-meter linear path in increments of 5 cm. This manual approach was implemented to eliminate any ambiguities regarding the antenna locations.

Performance comparisons between the various methodologies are tabulated in Table 4.1, focusing on key performance indicators like Mean Absolute Error (MAE) and Root Mean Squared Error (RMSE).

The performance evaluation clearly indicates the superiority of the proposed method over the other algorithms under consideration. Notably, the error associated with the proposed method diminished with increasing antenna height, registering as low as about 9 cm. This improvement is attributed to the reduced impact of ground reflection and the resulting multi-path effects at greater heights.

In comparison, ReLock’s performance was sensitive to the number of measurements, showing improvement with higher Tx power but still lagging behind the proposed method for this transmission power level. RDPF, on the other hand, produced robust and concise estimates but was outperformed by the results achieved by the proposed multistatic approach.

As for BackPos, the methodology was noticeably impacted by an increase in phase noise variance. This limitation arises from the method’s reliance on the difference of phase measurements, which inherently boosts the phase noise and, in turn, the error. Given these results, it is evident that the proposed method offers an accurate and reliable means for DoA estimation and 2D localization in RFID systems.

4.5.3 Simulated 3D Localization Results

The evaluation of the proposed 3D localization method, although only conducted via MATLAB simulations due to hardware and equipment constraints, shows promise in terms of accuracy. The use of MAE and RMSE as performance metrics, coupled with assumptions on phase noise, offers a comprehensive preliminary assessment of the algorithm’s effectiveness. It is encouraging that the 3D method exhibits similar accuracy metrics to the 2D algorithm under comparable conditions, which suggests robustness and scalability in the design.

Table 4.2: Simulation results of multistatic 3D localization.

	$\mathbb{E}[e]$ (cm)	$\sqrt{\mathbf{E}[e ^2]}$ (cm)
$\phi_i^n \sim \mathcal{N}(0, 1^\circ)$	6.93	11.93
$\phi_i^n \sim \mathcal{N}(0, 25^\circ)$	17.87	24.78

However, the significant computational time, estimated around one minute per position, could limit the algorithm’s applicability in real-time scenarios. This is a critical

bottleneck and represents an area where further optimization is essential, especially if the algorithm is to be used in time-sensitive applications.

4.5.4 Conclusion

In this study, we introduced two novel approaches to the field of RFID-based localization and Direction of Arrival (DoA) estimation: EllDoA and a multistatic 2D/3D localization algorithm. Each contributes unique methodologies and offers new possibilities for both theoretical exploration and practical application.

Starting with EllDoA, it brings a novel paradigm to the table by leveraging the geometry of ellipses in a bistatic or multistatic RFID setup. Unlike conventional methods that often depend on complex mathematical models or extensive computational resources, EllDoA utilizes the inherent properties of ellipse formations to deliver robust DoA estimates. Impressively, the performance of EllDoA was found to be comparable to state-of-the-art methods, such as MUSIC, which has been a go-to solution for DoA estimation. This positions EllDoA as a viable alternative or even a complementary approach in systems where bistatic or multistatic configurations can be implemented.

Our second major contribution, the multistatic 2D localization algorithm, is equally groundbreaking. It demonstrated remarkable resilience and accuracy, achieving centimeter-level 2D localization errors as low as 9 cm. What makes this accomplishment particularly noteworthy is the absence of typical facilitators for high accuracy, such as anchor tags and additional bandwidth, which means that the system can deliver highly accurate results within real-world constraints.

Finally, the promise shown by our 3D localization method should not be overlooked. Although the technique is currently in the simulation stage, preliminary results indicate a solid level of accuracy. Although further research and hardware-based validation are required, initial simulations suggest that this 3D localization approach has a high potential to deliver centimeter-level accuracy.

Chapter 5

Wireless Sensor Network Interrogation and Path Planning

In this chapter, we delve into the realm of backscatter technology, a field where reflection radio principles can be extensively applied. RFID tags, instead of actively transmitting a signal, leverage the principle of backscatter radio. They modulate their information on an illuminating RF signal, thus minimizing their power consumption.

The ultra-low-power and low-complexity nature of backscatter radio technology has made it an appealing choice for use in wireless sensor networks (WSNs). It has been employed in a variety of applications, demonstrating the capabilities of digital, frequency shift keying (FSK)-based, backscatter radio communication and deployments of backscatter radio-based WSNs. Other research has explored the use of analog, backscatter radio-based WSNs, as well as the utilization of pre-existing signals for RF illumination in backscatter radio-based WSN nodes.

Traditionally, the assumption has been an immobile interrogation setup, i.e., the receiver of backscattered signals and the RF illuminator are stationed at fixed locations. Although there have been studies involving unmanned aerial or ground vehicles (UAV/UGV) for the interrogation of backscatter radio-based sensors/tags, these have generally focused on system-level optimization.

In this work, we present an experimental study on UAV-based interrogation of a backscatter agricultural WSN. We have implemented a system capable of measuring humidity (and other attributes) at various points in a field, leveraging wireless backscatter technology. The gathered data can then be analyzed to infer the overall condition of the field. Such information allows farmers to monitor their crops more effectively and manage the resources distributed to the field accordingly, leading to more sustainable and efficient agricultural practices.

Our research primarily focuses on comparing different backscatter radio architectures in terms of interrogation speed and efficiency. The backscatter radio architectures employed require a carrier-wave to illuminate the sensor's antenna and can be categorized into two types:

- Monostatic: A single software-defined radio (SDR) is used to illuminate the sensors and receive and decode the backscattered signal.
- Bistatic: Two discrete devices are used - a carrier-wave emitter to illuminate the sensors and a remote SDR to receive and decode the signal. For the bistatic architecture, we considered two scenarios - a pedestrian versus a drone carrying the illuminator.

Experiments were conducted in both small and large scale deployments, across two distinctly different fields.

5.1 Backscatter Wireless Sensor Networks

5.1.1 WSN Deployments

Two separate deployments were conducted in the course of this research, each involving a different physical environment and distribution of RF soil moisture tags.

The first deployment consisted of a flat field with no obstructions, facilitating direct, line-of-sight paths between the tags and the receiver. A total of 10 RF tags were dispersed over an area of 307 m². The arrangement of this relatively small-scale deployment permitted an easy comparison between the efficiency of a pedestrian carrying an RF transmitter and a drone in interrogating the tags.

The second deployment was of a larger scale, involving a total of 15 RF tags scattered across a rocky, non-flat field of more than 4000 m² with olive trees. The tags were placed on top of the trees, at heights ranging from 2 to 4 meters. The substantial difference in the physical characteristics of the terrain, along with the higher distance between neighboring tags, was intended to provide a more challenging scenario, testing the efficiency of the different interrogation techniques under more demanding conditions.

The paths followed by the pedestrian and the drone in both deployments were determined by the Traveling Salesman Problem (TSP) algorithm, optimizing the sequence of tags to be interrogated. The planned paths, along with the deployment setup, are shown in Fig.5.5 for the first deployment and Fig.5.7 for the second one.

In both deployments, the drone’s take-off and landing position, denoted by a star symbol in the figures, were kept constant to ensure consistent conditions for each interrogation technique under test.

Next, we provide a detailed description of the hardware and tools used in these deployments, followed by an analysis of the different interrogation techniques employed.

5.1.2 Components

This research made use of several key hardware components in order to carry out the experiments.

A drone equipped with an SDR was one of the primary hardware tools. The SDR of the drone used in this work has the ability to simultaneously transmit and receive RF signals, which is crucial for both bistatic and monostatic interrogations. The SDR on the drone acted as a reader, providing both the illuminating signal and the receiver for processing and decoding the tag-backscattered signal during monostatic interrogation. For bistatic interrogation, only the transmit chain of the drone’s SDR was utilized to provide RF illumination.

For bistatic interrogation cases, a secondary SDR (USRP N200) was used as a receiver. This receiver was placed in a fixed position, separate from the transmitter, and was responsible for decoding the signal backscattered by the tags.

RF soil moisture tags were the targets of the interrogation in our experiments. These passive devices, when illuminated by RF signals, backscatter a modulated signal containing their measurement information, which can be decoded by the receiver.

Furthermore, an RF transmitter (Silicon Laboratories Si1064) was utilized in the pedestrian case. The transmitter was carried by a pedestrian who would walk the path dictated by the TSP algorithm’s solution, illuminating the tags as they proceeded.

The frequency and transmission power of the RF illumination in all cases was set to 868 MHz and 13 dBm, respectively. This ensured that the tags could be efficiently interrogated and operated within the regulated parameters for each scenario, allowing for a direct comparison of the results.

5.1.3 Interrogation Techniques

Three distinct methods of tag interrogation were employed in this work: a) bistatic interrogation by a pedestrian carrying an RF transmitter, b) bistatic interrogation with illumination provided by a drone, and c) monostatic interrogation using the drone, which both illuminates the tag and receives the backscattered signal.

In the bistatic pedestrian scenario (a), the person followed a path, holding an RF transmitter (Silicon Laboratories Si1064) to illuminate the tags. This scenario is illustrated in Figure 5.4 (left).

In the bistatic drone scenario (b), the drone followed a similar path, providing the RF illumination, while the backscattered signal was processed by a stationary SDR receiver. The illustration of this scenario can be seen in Figure 5.4 (right).

The monostatic drone scenario (c) saw the drone carrying out a dual role: providing RF illumination and processing the backscattered signals. The drone carried an SDR capable of simultaneous transmission and reception of RF signals, thus acting as a complete reader, emitting the illuminating signal, and receiving and decoding the tag-backscattered signal. Figure 5.4 (middle) visualizes this process.

5.2 Path Planning Algorithms

In order to interrogate all tags while traveling the minimum distance, different path planning approaches were explored. These strategies aim to optimize the drone's and pedestrian's route, either by navigating directly to each tag location or by covering the entire area defined by the tags' positions. The two approaches that were employed include: the Travelling Salesman Problem (TSP) solution and the Min-Waypoint approach.

5.2.1 Travelling Salesman Problem (TSP) Solution

The Travelling Salesman Problem (TSP) approach is one of the most widely studied problems in combinatorial optimization. It is named after a theoretical scenario where a salesman must travel between cities to sell their goods, with the goal of finding the shortest possible route that allows them to visit each city only once and return to their starting city. In the context of this project, each sensor/tag is treated as a city and the "distances" between the cities are the Euclidean distances between the tags. The interrogator's task is to find the shortest route that allows it to visit each tag location once and return to its starting point. This not only saves time, but in the case of the drone, it also conserves battery power.

The TSP problem is NP-hard, meaning that it is computationally intensive to solve exactly, especially as the number of cities (or tags) increases. Two different MATLAB tools were used to solve the TSP problem: MATLAB's binary integer programming solver and J. Kirk's "Traveling Salesman Problem - Genetic Algorithm," a genetic algorithm-based solver available on MATLAB Central File Exchange.

Binary integer programming is a category of integer programming where the goal is to discover the values of decision variables that minimize or maximize an objective function. In this context, the objective function is the total travel distance.

The Genetic Algorithm (GA) is a search heuristic that is inspired by Charles Darwin's theory of natural evolution. The algorithm reflects the process of natural selection where the fittest individuals are selected for reproduction in order to produce offspring of the next generation. It is used to find exact or approximate solutions to optimization and search problems.

Both methods performed optimally for the two deployment scenarios of 10 and 15 tags. For a theoretical case of 100 tags, they provided sub-optimal but satisfactory solutions. This is crucial for large-scale tag deployments, as the computation time of an exact TSP solver increases exponentially with the number of tags. Hence, an efficient TSP solver, such as the ones used, enables scalable deployment and efficient interrogation of soil moisture tags.

Fig. 5.1 shows the paths calculated by these TSP solvers for the first deployment scenario with 10 tags, and for the second deployment scenario with 15 tags. For each deployment, the paths were computed with the drone's take-off and landing position set as the TSP path's origin and ending points. It is important to note that these TSP paths determined the minimum path that had to be followed for the successful interrogation of all tags.

The steps of the TSP approach applied to the project can be elaborated as follows:

1. *Input Points*: The process begins by recording the coordinates of the tags/sensors using a GPS-enabled device (such as a mobile phone). These points represent the set of locations that the interrogator needs to visit.
2. *TSP Solving*: These points are then inputted into the TSP solver. The TSP solver utilizes one of techniques mentioned above to find the shortest possible route that visits each point once and returns to the starting point.
3. *Obtain Sequence*: Once the TSP solver has processed the input points, it provides an optimal sequence that represents the shortest possible route. This sequence forms the basis for the path of the interrogator.
4. *Waypoints Setting*: With the optimal sequence of tag locations, these points are then set as waypoints for the interrogator to visit. The drone can navigate from one waypoint to the next following straight paths, while the pedestrian has also to take into account possible geological obstacles present.

In addition, it is worth noting that the TSP approach can be adapted to accommodate real-world constraints and considerations. For instance, if there are areas that the drone or pedestrian cannot traverse through due to obstacles or no-fly zones, these areas can be incorporated into the TSP model as additional constraints, allowing for more practical and feasible routes.

Despite the high computational complexity of the TSP, it was found that the TSP approach was suitable for the purposes of this project, providing efficient and optimized paths for the interrogators to read all tags.

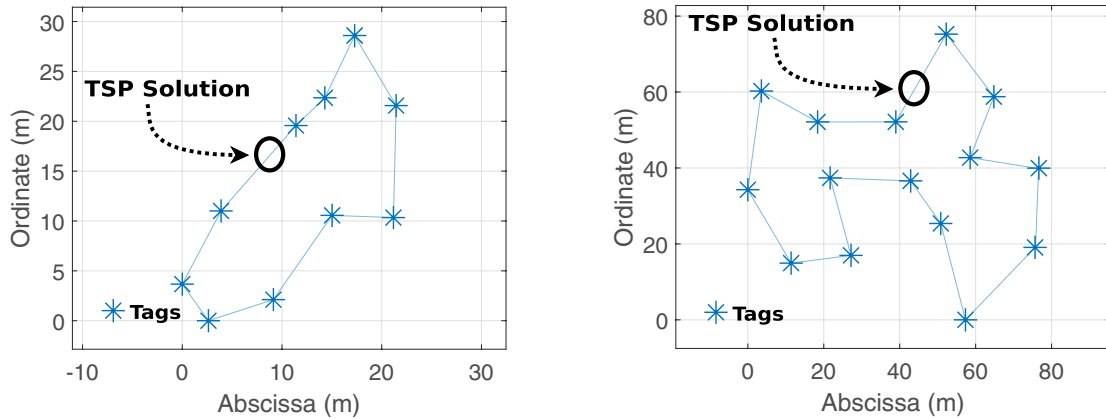


Figure 5.1: Travelling Salesman Problem approach path planning solution for 10 and 15 nodes. The total length of the solution path was 77.8 m and 314.5 m for the first deployment (left, small scale) and the second deployment (right, large scale), respectively.

5.2.2 Min-Waypoint Approach

The Min-Waypoint approach is a different strategy for the interrogator's path planning that aims to cover the whole area (convex hull) defined by the locations of the tags. Unlike the TSP approach, which is solely focused on visiting each tag once, the Min-Waypoint approach also collects data from intermediate points between tags. This can be especially useful when the exact locations of the tags are not available or when the drone is equipped with a camera or other sensors that can collect additional data as it flies between tags.

The core concept of the Min-Waypoint approach is to minimize the number of waypoints required to define the route, thus reducing the interrogator's travel time. Especially for the drone, since it has to gradually decrease its speed each time it reaches a waypoint, fewer waypoints result in a smoother and more efficient flight. The steps of the Min-Waypoint approach are as follows:

1. The convex hull of the tags' locations is constructed.

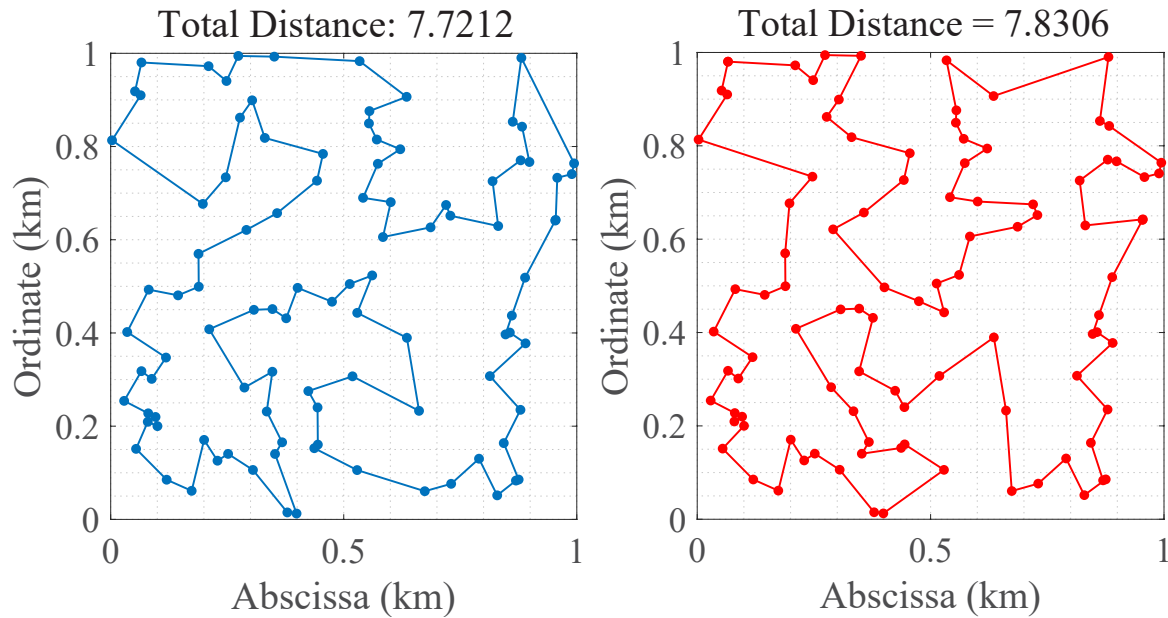


Figure 5.2: Comparison between binary integer programming (left) and genetic algorithm (right) TSP solution for 100 nodes, randomly placed

2. The perpendicular distance from each vertex of the hull to its antipodal edge is calculated. In case of an even number of edges, the distances to both antipodal edges are calculated.
3. The minimum of the distances computed in the previous step is found, and the direction of the parallel paths is determined by the edged corresponding to the minimum distance.
4. The interrogator moves in parallel lines and crosses the convex hull from one side to another. The direction of motion is determined in the previous step. The distance d_p between two adjacent lines depends on the flight altitude, the camera's/antenna's field of view, and the percentage of area overlap between two consecutive passes of the hull.
5. The distance between the edge determined at step 3 and its nearest of the parallel lines is set to be half the distance between two adjacent lines $d_p/2$. The path lines are drawn and the intersection points with the convex hull are set as the waypoints.
6. The waypoints are ordered to create the path of the drone in a way that shapes the desired parallel path lines. Four waypoints are candidates as the start of the route, with the closest to the drone's take-off location set as the beginning of the path.

A few modifications were made to the original algorithm to adapt it to the needs of this project.

- First, in the case of a convex hull with an even number of edges, two distances are computed instead of one to determine the direction of the path lines.
- Second, the starting waypoint is chosen considering the coordinates of the drone's take-off location.

The results of the Min-Waypoint approach were highly dependent on the flight altitude. Figs. 5.3 (left and right) show the paths produced by the Min-Waypoint algorithm for three different flight altitudes and for the tag locations used in Fig. 5.1. The antenna's angle of view was set to 120 degrees, and a 50% overlap was assumed for each crossing of the convex hull. As altitude decreased, more passes were required to cover the area of the tags, resulting in longer overall path lengths. Despite the increased path lengths, the Min-Waypoint approach was found to be an effective way to cover a larger area and collect more comprehensive data.

The same algorithm was also implemented for the tag locations that were used in Fig. 5.1 (right), and the results are shown in Fig. 5.3 (right). Three different routes were produced for 3 different flight altitudes, while sharing the same parameters as with the small scale setup (antenna's angle of view was set to 120° and an overlap of 50% was assumed at each crossing). The area of the convex hull in this deployment is significantly greater than previously, thus the routes occur to be longer too. For an altitude of 10 meters 4 passes are required, for 5 meters 8 passes, while for 1.8 meters 22 passes. Finally, the overall path length for altitude of 10, 5 and 1.8 meters is 332.9, 578.3 and 1415.4 meters, respectively.

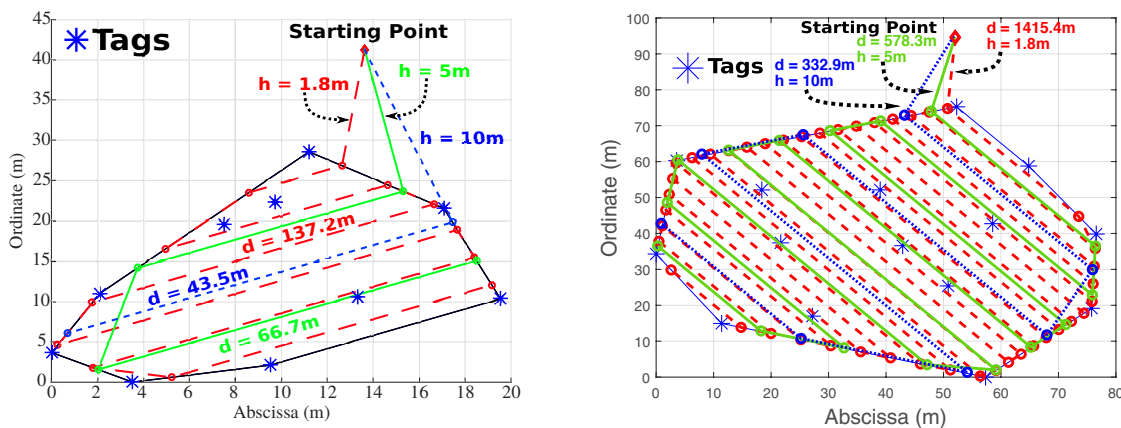


Figure 5.3: Min-Waypoint approach path planning solution for 10 and 15 nodes.

5.3 Implementation and Results

In this study, tag interrogation was performed using three techniques: bistatic interrogation by a pedestrian carrying an RF transmitter (Silicon Laboratories Si1064) illuminating the tags (Fig. 5.4 left), bistatic interrogation with illumination provided by the drone (Fig. 5.4 right), and monostatic interrogation using the same drone, where the drone illuminates a tag and receives the backscattered signal (Fig. 5.4 middle). For the second deployment, only cases a) and c) were considered. The frequency and transmission power of the RF illumination was set to 868 MHz and 13 dBm, respectively, for all cases.

The drone is equipped with an SDR with the capability to simultaneously transmit and receive RF signals. For bistatic interrogation, only the transmit chain of the SDR was used for providing RF illumination, while for monostatic interrogation, the drone’s SDR acted as a reader, providing both the illuminating signal and the receiver for processing and decoding the tag-backscattered signal. In the bistatic cases (pedestrian and drone) a secondary SDR (USRP N200) was used as the receiver (Figs. 5.4 left and middle).



Figure 5.4: The three experimental scenarios studied: bistatic pedestrian (left), bistatic drone (middle) and monostatic drone (right).

The paths followed by the pedestrian and the drone were generated by the TSP algorithm described in Sec. 5.2.1. These paths are demonstrated in Fig. 5.5 for the first deployment and in Fig. 5.7 for the second, as recorded by GPS. Notably, the drone’s take-off and landing positions are denoted by a star symbol.

Each soil moisture sensor/tag was considered to be successfully interrogated by evaluating the measurements of a (known) voltage reference reported back by the tag. Energy, time, and altitude data were acquired from the drone’s flight logs, while the pedestrian time was recorded using a stopwatch.

Garden Deployment

The initial deployment of the tags was carried out in a flat field with no obstructions, offering direct line-of-sight paths between the tags and the receiver, as shown in Fig. 5.5.

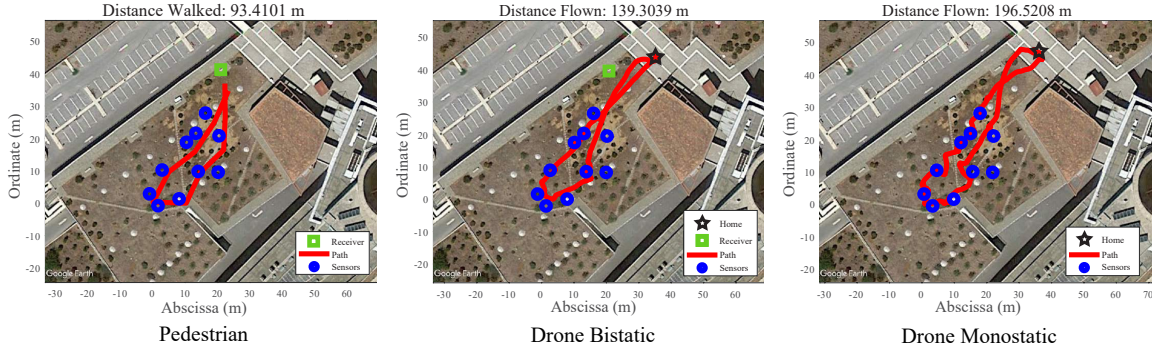


Figure 5.5: Garden deployment of 10 nodes (covering a area of 307m²) along with the respective paths that were followed during interrogation.

The time and energy spent for the tags’ interrogations are demonstrated in Fig. 5.6. It is evident from the figure that for a relatively small-scale deployment of tags (10 tags over 307 m²), walking while holding an RF transmitter for illuminating the tags (pedestrian case) was more efficient than using a drone.

Fig. 5.6 also indicates that the resources consumed, in terms of energy (Watt-hours) or time spent (seconds), roughly doubled from pedestrian bistatic to drone bistatic and then to drone monostatic interrogation for this relatively small-scale deployment. Interestingly, the bistatic drone interrogation proved to be more efficient than the monostatic interrogation.

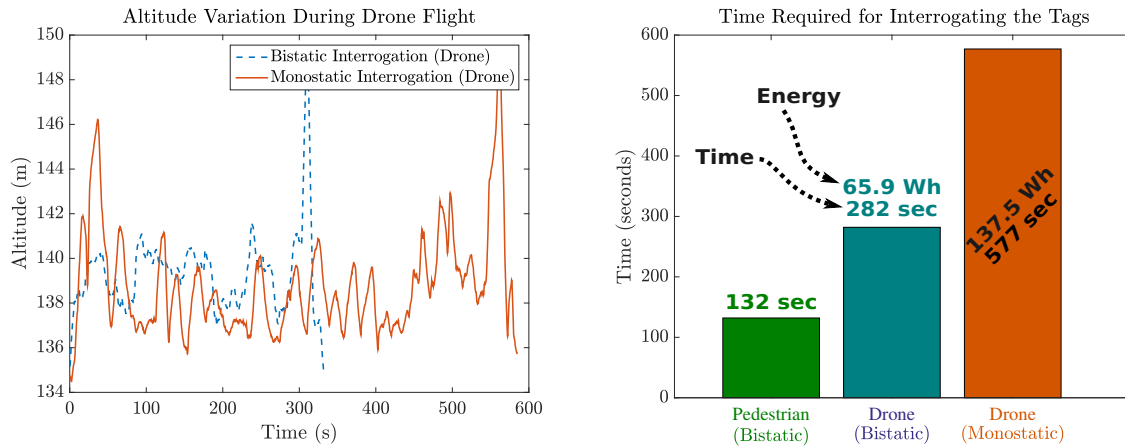


Figure 5.6: Drone altitude variations and time spent comparison for the different architectures.

The less efficient performance of the monostatic drone interrogation can be attributed to its geometry, leading to a worst-case scenario with respect to the power of the backscattered signal [55]. Given the limited scattering efficiency of the tags and their proximity to the ground, the drone had to hover at an “appropriate” location near each tag during monostatic interrogation until a successful read was recorded. This caused significant variations in the drone’s altitude and consequently incurred a significant time and energy overhead. In contrast, during the bistatic interrogation, the drone simply flew over the tags to provide RF illumination and the reception was handled by a remote SDR receiver (Fig.5.4 right), without intentional altitude variations. This is clearly illustrated by the intense altitude variations during monostatic interrogations as shown in Fig.5.8 (left).

It is also important to note that both drone experiments (bistatic and monostatic) were conducted under the same environmental conditions on a windy day. In the monostatic case, flying at low altitudes proved to be an additional disadvantage compared to the bistatic case where the drone flew at a higher altitude with the sole purpose of providing the RF illumination signal.

Field Deployment

In the second, larger deployment, 15 tags were scattered over a field of over 4000 m² as shown in Fig. 5.7. This deployment took place in a rocky, non-flat terrain populated by olive trees. The tags were positioned at the top of these trees, with heights ranging between 2 and 4 meters.

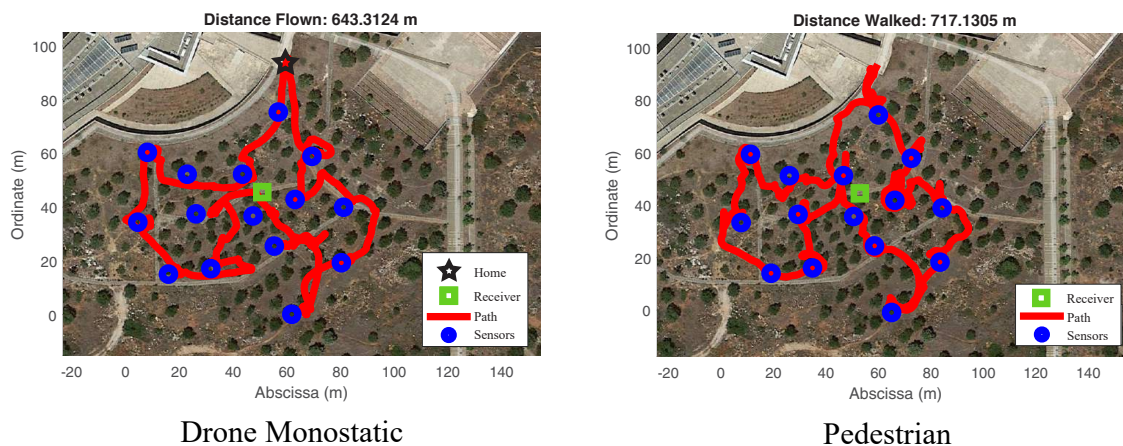


Figure 5.7: Field deployment of 15 nodes (covering and area > 4000m²) along with the respective paths that were followed during interrogation.

The time and energy resources required to interrogate the tags in this deployment are depicted in Fig. 5.8. These results demonstrate that, under the conditions of this particular terrain, the performance in terms of the time required for the interrogation was practically identical for all approaches.

Similarly to the first deployment, these experiments were conducted on a windy day and required the drone to fly at relatively low altitudes above the ground. However, the rough terrain also posed challenges for the pedestrian, resulting in additional delays in reaching each tag or tree. These factors contributed to the similar performance observed among all types of interrogation in this deployment.

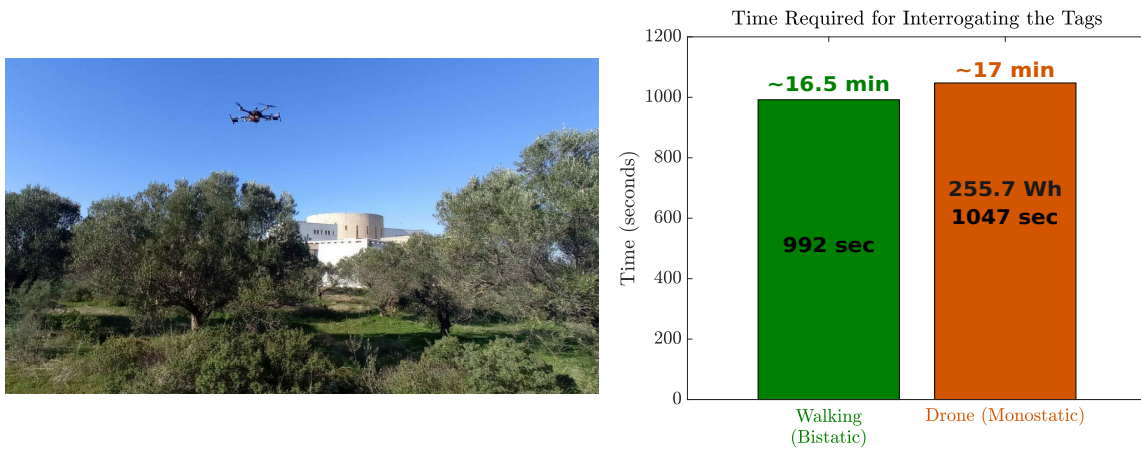


Figure 5.8: Indicative image of the tricky environment the drone had to operate in and time spent comparison for the different architectures.

These results, combined with those of the first deployment, underline the fact that there is no one-size-fits-all strategy in choosing the type of tag interrogation. The choice must be made considering the specific conditions of the terrain and other environmental factors.

Chapter 6

Conclusion

6.1 Recapitulation

This dissertation has been a profound journey through the intricate domain of RFID technology. From theoretical revelations to practical realizations, each chapter has unfolded a unique facet of RFID, illuminating its transformative capabilities and inherent challenges.

6.2 Major Findings and Achievements

A cornerstone of our exploration was the rigorous study presented in Chapter 2, where we delved into the intricacies of monostatic localization. The theoretical study and practical experiments conducted produced a narrowband phase-based localization method that offers robust performance in the presence of multipath, even when the tag phase measurements are sparse. By leveraging reader mobility, adaptable antenna counts, and robot-reader self-localization, our system showcased 24 cm mean average 3D localization error for RFID tags within a cluttered library setting. Remarkably, this was achieved without resorting to excessive bandwidth or reference tags. A classification method was also found that could assist in characterising the environment as multipath-rich or not. The findings from this chapter laid a strong foundation, guiding our subsequent investigations and shaping our understanding of the constraints and potentialities inherent to RFID systems.

As our journey progressed, we confronted the challenges posed by the multipath effect, specifically reflections originating from a wall. Our work in Chapter 3 set a precedent, marking the first, to our knowledge, application of such research on commercial RFID systems. We demonstrated that relying solely on a Line-of-Sight model, while ignoring potent reflectors can significantly hinder the performance of RFID localization. Moreover,

attempting to counteract multipath effects in scenarios where reflections are substantially attenuated could also inadvertently degrade system performance. While offering a unique algorithm for joint reflector and tag localization, this work provided a reflector localization accuracy of 5 cm and an insight on reflection order considerations.

Transitioning to the bistatic/multistatic architecture in Chapter 4 our study offered EllDoA and a multistatic 2D/3D localization method. EllDoA is an innovative Direction-of-Arrival (DoA) estimation method inspired by elliptical formations inherent to bistatic/multistatic RFID configurations. EllDoA's performance, benchmarked against established DoA techniques, showcased similar performance with a mean absolute error of 5° . Additionally, our proposed multistatic 2D localization technique provided robust 9 cm localization accuracy.

Lastly, in Chapter 5 we combined RFID and WSNs to create system—both pedestrian and UAV-backed—capable of interrogating backscatter sensors across agricultural areas using the monostatic or multistatic architecture. Our findings emphasized the context-dependent nature of interrogation type selection, underscoring the variability in performance across diverse deployment scales and terrains.

In summary, our research stands out for combining theoretical studies with their practical applications through our engineering prowess. From the integration of RFID with the Robotic Operating System (ROS) to the UAV-based interrogation of backscatter WSNs, our work has ushered in tangible, real-world systems primed for deployment in diverse scenarios, like warehouses, libraries, and agricultural landscapes.

6.3 Future Directions

While this dissertation has charted significant milestones in the realm of the ever evolving RFID technology, the horizon still presents numerous avenues for exploration. The complexities inherent to 3D localization, suggest potential refinements and advancements to enhance accuracy and robustness. As the environment and scenarios become more intricate, so does the challenge of maintaining precise localization estimates. Moreover, with the continued evolution of technology, there exists potential for deeper integration of RFID with other emergent systems, possibly creating hybrid solutions that draw upon the strengths of multiple domains. The continuous adaptation to and optimization for real-world scenarios, especially in dynamic environments, beckons further research.

Some promising directions for future research, though not exhaustive, include:

- **Leveraging Robotic Mobility:** The agility and mobility inherent to the robotic platform can be further exploited to diversify measurements. By altering the navi-

gation path and angles, we can potentially enhance localization accuracy, providing a richer data composition for analysis.

- **Trajectory Tracking:** Building upon our localization groundwork, there is potential to evolve these methodologies for real-time trajectory tracking.
- **Multi-Entity Estimation:** The joint tag-reflector estimation technique showcases promise for scalability. Extending this approach to concurrently estimate multiple tags and reflectors could significantly boost robustness and applicability.
- **Environment Characterization:** Devising algorithms capable of discerning between LoS and Non-LoS conditions, coupled with the ability to determine the dominant order of reflection (e.g., 1st or 2nd order).
- **Machine Learning Integration:** The vast data generated by RFID systems coupled with the mobility of our platforms presents an ideal playground for machine learning. Applying neural network techniques could not only help denoise measurements, but also offer precise localization estimates.
- **Harnessing SDR Capabilities:** Software-Defined Radio (SDR) devices, with their flexibility and adaptability, beckon further exploration. Delving deeper into their capabilities could elevate system practicality and performance, ensuring RFID systems that are both agile and efficient.

6.4 Closing Remarks

In conclusion, our research stands as a testament to the power of rigorous academic exploration coupled with hands-on problem solving. As we reflect on the milestones achieved, we remain optimistic about the transformative impact of RFID technology and eagerly anticipate the innovations that the future holds.

Bibliography

- [1] K. Finkenzeller, *RFID Handbook: Fundamentals and Applications in Contactless Smart Cards, Radio Frequency Identification and Near-Field Communication*, 3rd ed. Wiley, 2010.
- [2] D. M. Dobkin, *The RF in RFID: Passive UHF RFID in Practice*. Oxford, Boston: Newnes (Elsevier), 2008.
- [3] R. Want, “An introduction to RFID technology,” *IEEE Pervasive Computing*, vol. 5, no. 1, pp. 25–33, 2006.
- [4] “EPC Radio-Frequency Identity Protocols, Class-1 Generation-2 UHF RFID Protocol for Communications at 860 MHz - 960 MHz, version 1.2.0 EPC Global,” 2008.
- [5] J. D. Griffin and G. D. Durgin, “Gains for RF tags using multiple antennas,” *IEEE Trans. Antennas Propagat.*, vol. 56, no. 2, pp. 563–570, Feb. 2008.
- [6] J. D. Griffin and G. D. Durgin, “Multipath fading measurements at 5.8 GHz for backscatter tags with multiple antennas,” *IEEE Transactions on Antennas and Propagation*, vol. 58, no. 11, pp. 3693–3700, 2010.
- [7] G. Vannucci, A. Bletsas, and D. Leigh, “A software-defined radio system for backscatter sensor networks,” *IEEE Trans. Wireless Commun.*, vol. 7, no. 6, pp. 2170–2179, Jun. 2008.
- [8] P. N. Alevizos, G. Vougioukas, and A. Bletsas, “Batteryless backscatter sensor networks—part i: Challenges with (really) simple tags,” *IEEE Communications Letters*, vol. 27, no. 3, pp. 763–767, 2023.
- [9] J. Kimionis, A. Bletsas, and J. N. Sahalos, “Bistatic backscatter radio for tag read-range extension,” in *Proc. IEEE Int. Conf. on RFID-Technologies and Applications (RFID-TA)*, Nice, France, Nov. 2012.

- [10] J. Kimionis, A. Bletsas, and J. N. Sahalos, "Bistatic backscatter radio for power-limited sensor networks," in *Proc. IEEE Global Commun. Conf. (Globecom)*, Atlanta, GA, Dec. 2013, pp. 353–358.
- [11] J. Kimionis, A. Bletsas, and J. N. Sahalos, "Increased range bistatic scatter radio," *IEEE Trans. Commun.*, vol. 62, no. 3, pp. 1091–1104, Mar. 2014.
- [12] E. Kampianakis, J. Kimionis, K. Tountas, C. Konstantopoulos, E. Koutroulis, and A. Bletsas, "Backscatter sensor network for extended ranges and low cost with frequency modulators: Application on wireless humidity sensing," in *Proc. IEEE Sensors Conf. (Sensors)*, Baltimore, MD, USA, Nov. 2013.
- [13] C. Konstantopoulos, E. Koutroulis, N. Mitianoudis, and A. Bletsas, "Converting a plant to a battery and wireless sensor with scatter radio and ultra-low cost," *IEEE Trans. Instrum. Meas.*, vol. 65, no. 2, pp. 388–398, Feb. 2016.
- [14] S. N. Daskalakis, S. D. Assimonis, E. Kampianakis, and A. Bletsas, "Soil moisture scatter radio networking with low power," *IEEE Trans. Microwave Theory Tech.*, vol. 64, no. 7, pp. 2338–2346, Jul. 2016.
- [15] G. Vougioukas and A. Bletsas, "24 μ W 26m range batteryless backscatter sensors with FM remodulation and selection diversity," in *Proc. IEEE Int. Conf. on RFID-Technologies and Applications (RFID-TA)*, Warsaw, Poland, Sep. 2017.
- [16] G. Vougioukas and A. Bletsas, "Switching frequency techniques for universal ambient backscatter networking," *IEEE J. Select. Areas Commun.*, pp. 1–1, 2018.
- [17] C. Men, L. Mao, and L. Wu, "The research of RFID localization technology based on bi-directional RSSI," in *2012 8th International Conference on Wireless Communications, Networking and Mobile Computing*, 2012, pp. 1–4.
- [18] X. Zhang, J.-M. Akre, S. Baey, A. Fladenmuller, B. Kervella, M. Zancanaro, and M. Fonseca, "Towards localization of RFID tags based on experimental analysis of RSSI," in *2014 IFIP Wireless Days (WD)*, 2014, pp. 1–4.
- [19] S. Siachalou, A. Bletsas, J. Sahalos, and A. G. Dimitriou, "RSSI-based maximum likelihood localization of passive RFID tags using a mobile cart," in *2016 IEEE Wireless Power Transfer Conference (WPTC)*, 2016, pp. 1–4.
- [20] A. Buffi, P. Nepa, and F. Lombardini, "A phase-based technique for localization of UHF-RFID tags moving on a conveyor belt: Performance analysis and test-case measurements," *IEEE Sensors J.*, vol. 15, no. 1, pp. 387–396, Jan. 2015.

- [21] A. Tzitzis, S. Megalou, S. Siachalou, T. Yioultis, A. Kehagias, E. Tsardoulis, A. Filotheou, A. Symeonidis, L. Petrou, and A. G. Dimitriou, "Phase ReLock - Localization of RFID tags by a moving robot," in *Proc. IEEE European Conf. on Antennas and Propagation (EuCAP)*, Krakow, Poland, Mar. 2019, pp. 1–5.
- [22] Z. Liu, Z. Fu, T. Li, I. White, R. Penty, and M. Crisp, "A phase-based relative localization method using a mobile platform with minimal reference tags," in *2022 IEEE International Conference on RFID (RFID)*, 2022, pp. 150–154.
- [23] F. Martinelli, "A robot localization system combining RSSI and phase shift in UHF-RFID signals," *IEEE Transactions on Control Systems Technology*, vol. 23, no. 5, pp. 1782–1796, 2015.
- [24] D. Vasicht, S. Kumar, and D. Katabi, "Decimeter-level localization with a single WiFi access point," in *Proc. USENIX Symposium on Networked Systems Design and Implementation (NSDI)*, Santa Clara, USA, Mar. 2016, pp. 165–178.
- [25] R. Miesen, F. Kirsch, and M. Vossiek, "Holographic localization of passive UHF RFID transponders," in *Proc. IEEE Int. Conf. on RFID*, Orlando, USA, Apr. 2011, pp. 32–37.
- [26] F. Martinelli, "Simultaneous localization and mapping using the phase of passive UHF-RFID signals," *Journal of Intelligent & Robotic Systems (JINT)*, vol. 94, no. 3-4, pp. 711–725, Jul. 2019.
- [27] S. Wang, M. Xia, and Y.-C. Wu, "Backscatter data collection with unmanned ground vehicle: Mobility management and power allocation," *IEEE Trans. Wireless Commun.*, vol. 18, no. 4, pp. 2314–2328, 2019.
- [28] G. Yang, R. Dai, and Y.-C. Liang, "Energy-efficient UAV backscatter communication with joint trajectory design and resource optimization," *IEEE Trans. Wireless Commun.*, vol. 20, no. 2, pp. 926–941, 2021.
- [29] J. S. Choi, B. R. Son, H. K. Kang, and D. H. Lee, "Indoor localization of unmanned aerial vehicle based on passive UHF RFID systems," in *International Conference on Ubiquitous Robots and Ambient Intelligence (URAI)*, 2012, pp. 188–189.
- [30] A. Buffi, A. Motroni, P. Nepa, B. Tellini, and R. Cioni, "A SAR-based measurement method for passive-tag positioning with a flying UHF-RFID reader," *IEEE Trans. Instrum. Meas.*, vol. 68, no. 3, pp. 845–853, 2019.

- [31] G. Greco, C. Lucianaz, S. Bertoldo, and M. Allegretti, "Localization of RFID tags for environmental monitoring using UAV," in *IEEE 1st International Forum on Research and Technologies for Society and Industry Leveraging a better tomorrow (RTSI)*, 2015, pp. 480–483.
- [32] G. Casati, M. Longhi, D. Latini, F. Carbone, S. Amendola, F. Del Frate, G. Schiavon, and G. Marrocco, "The interrogation footprint of RFID-UAV: Electromagnetic modelling and experimentations," *IEEE Journal of Radio Frequency Identification*, vol. 1, no. 2, pp. 155–162, 2017.
- [33] M. Longhi, G. Casati, D. Latini, F. Carbone, F. Del Frate, and G. Marrocco, "Rfidrone: Preliminary experiments and electromagnetic models," in *URSI International Symposium on Electromagnetic Theory (EMTS)*, 2016, pp. 450–453.
- [34] G. Casella, B. Bigliardi, and E. Bottani, "The evolution of RFID technology in the logistics field: a review," *Procedia Computer Science*, vol. 200, pp. 1582–1592, 2022.
- [35] M. Li, S. Gu, G. Chen, and Z. Zhu, "A RFID-based intelligent warehouse management system design and implementation," in *2011 IEEE 8th International Conference on e-Business Engineering*, 2011, pp. 178–184.
- [36] T. Kelepouris, K. Pramataris, and G. Doukidis, "RFID-enabled traceability in the food supply chain," *Industrial Management and Data Systems*, vol. 107, pp. 183–200, 03 2007.
- [37] W. Yao, C.-H. Chu, and Z. Li, "The use of RFID in healthcare: Benefits and barriers," in *2010 IEEE International Conference on RFID-Technology and Applications*, 2010, pp. 128–134.
- [38] A. Polycarpou, A. Dimitriou, A. Bletsas, P. Polycarpou, L. Papaloizou, G. Gregoriou, and J. Sahalos, "On the design, installation, and evaluation of a radio-frequency identification system for healthcare applications," *IEEE Antennas Propagat. Mag.*, vol. 54, no. 4, pp. 255–271, Aug. 2012.
- [39] V. U. Oliveira, "Applying RFID technology to improve hospital logistics," in *2022 IEEE 12th International Conference on RFID Technology and Applications (RFID-TA)*, 2022, pp. 191–193.
- [40] G. Vougioukas, N. Ntantidakis, E. Karatarakis, G. Apostolakis, and A. Bletsas, "Batteryless backscatter sensor networks—part ii: Lessons from scalable deployment," *IEEE Communications Letters*, vol. 27, no. 3, pp. 768–772, 2023.

- [41] R. Rayhana, G. Xiao, and Z. Liu, “RFID sensing technologies for smart agriculture,” *IEEE Instrumentation & Measurement Magazine*, vol. 24, no. 3, pp. 50–60, 2021.
- [42] M. Quigley, K. Conley, B. Gerkey, J. Faust, T. Foote, J. Leibs, R. Wheeler, and A. Ng, “ROS: an open-source robot operating system,” in *Proc. of the IEEE Intl. Conf. on Robotics and Automation (ICRA) Workshop on Open Source Robotics*, Kobe, Japan, May 2009.
- [43] T. Liu, Y. Liu, L. Yang, Y. Guo, and C. Wang, “BackPos: High accuracy backscatter positioning system,” *IEEE Trans. on Mobile Computing*, vol. 15, no. 3, pp. 586–598, Mar. 2016.
- [44] W. Hess, D. Kohler, H. Rapp, and D. Andor, “Real-time loop closure in 2D LIDAR SLAM,” in *Proc. IEEE Int. Conf. on Robotics and Automation (ICRA)*, Stockholm, Sweden, May 2016, pp. 1271–1278.
- [45] F. Dellaert, D. Fox, W. Burgard, and S. Thrun, “Monte carlo localization for mobile robots,” in *Proceedings 1999 IEEE International Conference on Robotics and Automation (Cat. No.99CH36288C)*, vol. 2, 1999, pp. 1322–1328 vol.2.
- [46] Brian P. Gerkey, “AMCL ROS package.” [Online]. Available: <http://wiki.ros.org/amcl>
- [47] S. Peppas, “Indoor RF localization with algebraic methods,” Diploma thesis available at: <https://dias.library.tuc.gr/view/90594>, School of ECE, Technical University of Crete, Chania, Greece, Oct. 2021, Supervisor A. Bletsas.
- [48] M. Leigsnering, F. Ahmad, M. G. Amin, and A. M. Zoubir, “Compressive sensing based specular multipath exploitation for through-the-wall radar imaging,” in *IEEE International Conference on Acoustics, Speech and Signal Processing (ICASSP)*, Oct. 2013, pp. 6004–6008.
- [49] S. J. Wright, R. D. Nowak, and M. A. T. Figueiredo, “Sparse reconstruction by separable approximation,” *IEEE Transactions on Signal Processing*, vol. 57, no. 7, pp. 2479–2493, Jul. 2009.
- [50] M. Leigsnering, “Sparsity-based multipath exploitation for through-the-wall radar imaging,” Ph.D. dissertation, Technische Universität Darmstadt, 2016.
- [51] C. Li, E. Tanghe, D. Plets, P. Suanet, N. Podevijn, J. Hoebeke, E. D. Poorter, L. Martens, and W. Joseph, “Phase-based variant maximum likelihood positioning

for passive UHF-RFID tags,” in *Proc. IEEE European Conf. on Antennas and Propagation (EuCAP)*, Mar. 2020.

- [52] K. Skyvalakis, “Low-cost software-defined radios (SDR) & techniques for robotic RFID systems,” Master’s thesis, Technical University of Crete, Jul. 2021, supervisor A. Bletsas.
- [53] J. Richter-Gebert, *Perspectives on Projective Geometry: A Guided Tour Through Real and Complex Geometry*, 1st ed. Springer Publishing Company, Incorporated, 2011.
- [54] N. Kargas, F. Mavromatis, and A. Bletsas, “Fully-coherent reader with commodity SDR for Gen2 FM0 and computational RFID,” *IEEE Wireless Commun. Lett.*, vol. 4, no. 6, pp. 617–620, Dec. 2015.
- [55] P. N. Alevizos, K. Tountas, and A. Bletsas, “Multistatic scatter radio sensor networks for extended coverage,” *IEEE Trans. Wireless Commun.*, vol. 17, no. 7, pp. 4522–4535, Jul. 2018.